A simulation-based approach to the fluid-structure interaction inside fatigue cracks in hydraulic components

Zur Erlangung des akademischen Grades eines

Doktors der Ingenieurwissenschaften (Dr.-Ing.)

von der KIT-Fakultät für Maschinenbau
des Karlsruher Instituts für Technologie (KIT)

angenommene

Dissertation

von

M.Sc. Lukas Michiels

Tag der mündlichen Prüfung:	23. Mai 2024
Erster Gutachter:	Prof. Dr.-Ing. Marcus Geimer
Zweiter Gutachter:	Prof. Dr.-Ing. Katharina Schmitz

Abstract

Fatigue plays an important role in the dimensioning of hydraulic components. Cyclic loads lead to crack growth, limiting the components' service life, and new developments require extensive testing to ensure the desired service life. The principle of linear damage accumulation assumes that the damage is independent of the progression over time. Only the number and amplitude of the load cycles are relevant. However, experiments on hydraulic components indicated that the temporal gradient of the applied load pressure influences fatigue crack growth.

Previous studies have raised two competing mechanisms. On the one hand, the hydraulic pressure causes an additional load on the crack faces as the oil penetrates the crack. On the other hand, a highly viscous fluid cannot flow out of the crack during rapid load changes, which reduces the effective damage amplitude. Previous empirical studies did not differentiate between these mechanisms or quantify their impact.

This work investigates the oil flow within a crack and its influence on the damage amplitude. Due to the small crack sizes, measuring the fluid flow within fatigue cracks is difficult. Instead, the flow in the crack is modeled with an averaged thin-film flow and coupled with a mechanical model of the crack opening to a dynamic simulation of the fluid-structure interaction. Strain measurements during cyclic pressure pulsations permit reconstruction of the oil flow and validation of the simulation.

The simulation method is able to simulate the oil flow in the crack and the crack opening displacement during rapid load changes, providing a better understanding of the fluid-structure interaction in fatigue cracks and its impact on fatigue crack growth. Adapted simulations can reduce the number of necessary tests and thus make development processes faster and more cost-effective.

***Keywords*:** Fatigue, Fluid-Structure Interaction, Fluid-Induced Crack Closure, Computational Fluid Dynamics

Kurzfassung

Ermüdungsbelastungen spielen eine wichtige Rolle bei der Dimensionierung hydraulischer Bauelemente. Zyklische Belastungen führen zu Risswachstum, welches die Lebensdauer der Bauelemente limitiert. Bei Neuentwicklungen sind aufwendige Versuche notwendig, um die gewünschte Lebensdauer sicherzustellen.
Nach dem Prinzip der linearen Schadensakkumulation wird davon ausgegangen, dass die Schädigung unabhängig von dem zeitlichen Verlauf der Beanspruchung auftritt. Versuche mit hydraulischen Bauteilen haben jedoch gezeigt, dass der zeitliche Verlauf der Belastung einen Einfluss auf das Ermüdungsverhalten hat. In bisherigen Versuchen wurden zwei konkurrierende Mechanismen als Ursache ermittelt.
Aufgrund des Öldruckes werden die Rissflanken durch das eindringende Öl zusätzlich belastet. Das hochviskose Öl fließt bei Lastwechseln jedoch nur mit Verzögerung aus dem Riss, wodurch bei schnellen zyklischen Lastenwechseln die effektive Schädigungsamplitude verringert wird. Bisherige Untersuchungen konnten den Einfluss der beiden Mechanismen nicht abschließend quantifizieren und voneinander abgrenzen.
Diese Arbeit untersucht den Ölfluss innerhalb von Rissen und dessen Einfluss auf die Schädigungsamplitude. Die Strömung im Riss wird mit einer Dünnfilmströmung modelliert und mit einem Fließstreifenmodell der Rissöffnung gekoppelt. Während zyklischer Druckbelastung wird der Ölfluss im Riss über die Bauteildehnung ermittelt und die Simulationsmodelle validiert.
Die Ergebnisse verbessern das Verständnis der Fluid-Struktur-Interaktion und deren Einfluss auf das Ermüdungsverhalten in Rissen. Angepasste Simulationsmethoden können die Anzahl der notwendigen Versuche verringern, um Entwicklungsprozesse schneller und kosteneffizienter zu gestalten.

***Schlagworte*:** Bauteilermüdung, Fluid-Struktur Interaktion, Fluid-Induziertes Rissschließen, Strömungssimulation

Danksagung

Die vorliegende Arbeit wurde während meiner Tätigkeit als wissenschaftlicher Mitarbeiter und Promotionsstudent am Institutsteil für mobile Arbeitsmaschinen (Mobima) des Karlsruher Instituts für Technologie (KIT) entstanden.

Ich möchte meinem Doktorvater Prof. Dr.-Ing. Marcus Geimer herzlich für seine wissenschaftliche Betreuung und die Übernahme des Hauptreferats danken. Der Freiraum und die Unterstützung, die Sie und das Institut mir für diese Arbeit gewährten, war entscheidend für den Erfolg der Arbeit. Neben meiner fachlichen Entwicklung konnte ich auch persönlich viel dazulernen. Prof. Dr.-Ing. Katharina Schmitz, Leiterin des Instituts für fluidtechnische Antriebe und Systeme der RWTH Aachen University, danke ich für Ihr Interesse an meiner Arbeit und die Übernahme des Korreferats. Ebenso bedanke ich mich herzlich bei Prof. Dr.-Ing. Christoph Stiller, Leiter des Instituts für Mess- und Regelungstechnik am KIT, für die Leitung der Prüfung.

Ein großes Dankeschön geht auch an meine Institutskollegen für Ihre fachliche und persönliche Unterstützung. Besonders möchte ich meinem Bürokollegen Benjamin Kazenwadel im Büro 019 und meinem Büronachbarn Sebastian Beiser für die gemeinsame Zeit und die wertvolle Unterstützung danken. Den studentischen Hilfskräften und Abschlussarbeitern, die mich während meiner Promotionszeit unterstützt haben, möchte ich für Ihre unschätzbare Unterstützung danken. Ohne sie wäre vieles nicht möglich gewesen, und ich habe viel von ihnen gelernt.

Ein besonderer Dank gebührt meinen Eltern und meiner Familie für ihre uneingeschränkte Unterstützung und den bedingungslosen Rückhalt während meiner gesamten Ausbildung und Promotionszeit. Vielen Dank, dass Ihr immer meinen Lebensweg unterstützt und mein Studium und meine Promotion ermöglicht habt. An dieser Stelle gilt mein ganz besonderer Dank meiner Partnerin Stephanie. Du standest mir während meiner Promotion immer liebevoll und geduldig zur Seite, und auch wenn ich am Verzweifeln war, hast Du mich neu motiviert.

Zu guter Letzt möchte ich allen in der Wissenschaft danken, die unter schiwerigen Umständen die Forschung und Technik vorantreiben und auch in schwierigen Zeiten durch viel Energie und Aufopferung neue Lösungswege für scheinbar unüberwindbare Probleme finden:

If nothing goes right, go left.
- Unknown

Karlsruhe, im Mai 2024 *M.Sc. Lukas Michiels*

Contents

Abbreviations and Symbols

Mathematical Notations

Scalar	Lower- and Uppercase Letters: a, A
Vector	Letters with Arrow Overline: $\vec{a}, \vec{B}$
Matrix	Bold Letters: $\mathbf{a}, \mathbf{B}$
$D(\cdot)$	Differential Operator
$\mathbb{E}(\cdot)$	Expected Value
$O(\cdot)$	Big-O Notation
$\Delta(\cdot)$	Discrete Difference
$d(\cdot)$	Derivative
$\partial(\cdot)$	Partial Derivative
$\dot{(\cdot)}$	Temporal Derivative
$\bar{(\cdot)}$	Arithmetic Mean
$(\cdot)^*$	Normalized Variable
$\hat{(\cdot)}$	Specific Value
$\tilde{(\cdot)}$	Approximated Value
$\lfloor(\cdot)\rfloor$	Rounded Down Value

Acronyms

ADC	Analog-Digital-Converter
CFD	Computational Fluid Dynamics
COD	Crack Opening Displacement
FEM	Finite-Element Method
FVM	Finite-Volume Method
YSM	Yield Strip Model

FSI	Fluid-Structure Interaction
PGA	Programmable Gain Amplifier
PZS	Plastic Zone Size
SIF	Stress Intensity Factor
SPI	Serial Peripheral Interface

Latin Symbols

b	Crack Width	mm
da/dN	Crack Advancement per Cycle	$\mu m/1$
dp	Temporal Pressure Gradient	$kbar/s$
$f(\cdot)$	Function Definition	-
f_b	Body Forces	N/kg
f_p	Pulse Frequency	Hz
h	Crack Opening Displacement	μm
i	Index	-
j	Index	-
k	Temporal Index	-
k_{sg}	Strain Gauges Measurement Sensitivity	-
l	Length	mm
l_0	Crack Length	mm
m	Mass	kg
n	Spatial Index	-
n_P	Paris' Law Material Constant	-
n_{FM}	NASGRO Material Constant	-
$\vec{n}$	Surface Normal	-
p	Fluid Pressure	bar
p_{FM}	NASGRO Material Constant	-
q	Volume Flow per Unit Length	m^2/s
q_{FM}	NASGRO Material Constant	-
r	Crack Tip Radius	mm
s	Streamline	m
t	Temporal Coordinate	s
$u_{x/y/z}$	Velocity	m/s

$v_{x/y/z}$	Displacement	m
w	Weight Function	-
x	Spatial Coordinate	mm
y	Spatial Coordinate	mm
z	Spatial Coordinate	mm
A_0, A_1, A_2, A_3	NASGRO Material Coefficients	-
C	Polynomial Coeffcient	-
C_{FM}	NASGRO Material Constant	$m^{1+n/2}/MPa^n$
C_P	Paris' Law Material Constant	$m^{1+n/2}/MPa^n$
E	Young's Modulus	MPa
F	Force	N
H	Characteristic Height	μm
K	Bulk Modulus	MPa
K_I	Mode I Stress Intensity Factor	$MPa\sqrt{m}$
K_{II}	Mode II Stress Intensity Factor	$MPa\sqrt{m}$
$K_{I,th}$	Mode I Stress Intensity Threshold	$MPa\sqrt{m}$
K_{IC}	Critical Mode I Stress Intensity Factor	$MPa\sqrt{m}$
$K_{I,eff}$	Effective Mode I Stress Intensity Factor	$MPa\sqrt{m}$
L	Characteristic Length	mm
M	Number of Time Steps	-
N	Number of Spatial Nodes	-
Q	Volume Flow	m^3/s
R_a	Arithmetic Average Surface Roughness	μm
R_{bridge}	Bridge Resistor Value	Ω
R_h	Hydraulic Resistance	bar/m^3
Re	Reynolds Number	-
Re_ζ	Reduced Reynolds Number	-
R_{PT100}	PT100 Resistance	Ω
R_{SG}	Strain Gauge Resistance	Ω
R_{SR}	Stress Ratio	-
$R1, R2, R3, R4$	Resistor Values	Ω
S	Surface Area	m^2
S_R	NASGRO Material Constant	-

T	Temperatur	$°C$
U	Voltage	V
V	Volume	m^3
Y	Geometry Factor	-

Greek Symbols

α_{FM}	NASGRO Material Constant	-
α_{pl}	Fictive Crack Shift	μm
α_T	Thermal Expansion Coefficient	K^{-1}
$\beta_{1/2}$	Boundary Condition	-
γ	NASGRO Crack Opening Function	-
ζ	Aspect Ratio	-
ϵ	Strain	mm/m
η	Dynamic Viscosity	$Pa \cdot s$
θ	Flow Factor	-
ι	Index	-
κ	Stress State	-
λ	Under-Relaxation Factor	-
ν	Poisson's Coefficient	-
ξ	Center Coordinate of Node	mm
ρ	Density	kg/m^3
σ	Mechanic Stress	MPa
σ_Y	Yield Strength	MPa
σ_{SD}	Standard Deviation	-
τ	Filter Time Constant	s
υ	Control Volume	m^3
φ	Angle	rad
ω	Random Noise	-
ω_{PZ}	Plastic Zone Size	μm
Γ	Characteristic Time	s
$\Lambda_{1/2}$	Boundary Condition	-
Π	Order of Polynomial Approximation	-
Φ	Intensive Property	-

Ω	Characteristic Frequency	Hz
Ψ	Characteristic Velocity	m/s

Sub- and Superscripts

$(\cdot)_0$	Initial Value
$(\cdot)_i$	Index
$(\cdot)_j$	Index
$(\cdot)_k$	Temporal Index
$(\cdot)_n$	Spatial Index
$(\cdot)_{min}$	Minimal Value
$(\cdot)_{max}$	Maximal Value
$(\cdot)_{ext}$	External Value
$(\cdot)_p$	Predicted Value
$(\cdot)_m$	Measured Value
$(\cdot)_{ref}$	Reference Value
$(\cdot)_{ex}$	Excitation Value
$(\cdot)_{pl}$	Plastic Value
$(\cdot)_{p2p}$	Peak to Peak Value
$(\cdot)_{th}$	Threshold Value
$(\cdot)_{dr}$	Drop Rate
$(\cdot)_{bu}$	Build-Up Rate
$(\cdot)_{lp}$	Low-Pass Filter
$(\cdot)^l$	Left Approximation
$(\cdot)^r$	Right Approximation

1 Introduction

Hydraulic actuators are essential in mobile machinery, providing high power density, reliability, and robustness to harsh environmental conditions. In recent decades, increasing fuel costs and the aim to reduce CO_2 emissions have driven the development of more energy-efficient hydraulic power systems. While electrification is promising for emission reduction, electric actuators do not achieve the hydraulics' power density and reliability. New hybrid concepts have emerged as an alternative to purely electric drivetrains, as hydraulic actuators remain essential for many applications. New developments must be efficient in terms of energy and material consumption, as resources and energy are expensive. Improved lightweight designs can reduce weight, material consumption, and costs.

However, reducing material consumption is only possible as long as the lifetime remains sufficient. Repeated transient loads limit the lifetime of components in hydraulic systems. Microscopic defects propagate due to repeated loads, leading to fatigue damage and component failure. Most components are designed to work in a high-cycle fatigue regime, where weight and material consumption are optimized under the constraint of a sufficient lifetime. New developments require extensive testing to ensure the desired lifetime and prevent premature failure. Experimental fatigue tests are expensive and time-consuming. Fatigue tests of hydraulic components are commonly done on pulsation test rigs with constant pulsation frequency. The established standards for pressure impulse tests, e.g., ISO 6802 and ISO 6803, define pulse frequencies between 0.5 and 1.3 Hz. Higher pulse frequency can accelerate the tests and decrease costs. Fatigue simulations, on the other hand, can estimate crack propagation in an early stage and help reduce experimental fatigue tests to a minimum.

Components are replaced before they reach their estimated lifetime to avoid system failure. Due to the high variation of fatigue crack propagation and crack initiation, the lifetimes are estimated with high safety margins. An alternative to predefined replacement cycles is condition monitoring. Condition

monitoring assesses the components' remaining lifetime and limits replacement to components before imminent failure. Hence, preventive replacements are avoided, reducing resource consumption and total costs of ownership. However, in both cases, an accurate prediction of the crack propagation rate is essential to ensure the lifetime and define adjusted service intervals without unnecessary safety margins. To achieve accurate predictions, knowledge of the underlying fatigue mechanisms is fundamental.

The cumulative damage theory and many crack propagation laws presume that the crack propagation rate in metals depends on the number of load cycles and their load amplitude, [1], [2]. At the same time, the temporal gradient of the load does not influence the crack growth. In contrast, the crack propagation rate of specimens in contact with a viscous fluid is supposed to depend on the temporal gradient of the load due to the interaction of the fluid with the mechanical structure, [3], [4]. Similar effects are to be expected in hydraulic components, which are subject to a wide range of pressure gradients.
The temporal pressure gradients at the control plate of axial piston pumps can reach up to 450,000 bar/s. Similar magnitudes occur at throttle and orifice geometries of valves. Depending on the geometry and design, temporal pressure gradients of 300,000 up to a maximum of 1,000,000 bar/s have been reported for these components. In contrast to these internal gradients, external loads can cause severe temporal pressure gradients in the entire hydraulic circuit, e.g., the impact of the bucket of a wheel loader generates pressure gradients of up to 20,000 bar/s. [5], [6]

The influence of the temporal gradient is supposed to be due to the interaction of the fluid with the structure. Due to its viscosity, the fluid flow is not independent of the temporal gradient. However, how the fluid influences the crack propagation has not been conclusively investigated. For this purpose, a more detailed investigation of the reciprocal relation between the fluid and the surrounding structure, the so-called fluid-structure interaction, is necessary. This work contributes to closing this research gap by providing a method to simulate the fluid-structure interaction in fatigue cracks. The simulation can predict the oil flow inside the crack and derive the effective stress amplitude for load pressures with arbitrary temporal gradients.
Investigations of the fluid-structure interaction in hydraulics are essential for improving fatigue predictions in hydraulic components. Neglecting the influences of fluid-structure interaction leads to incorrect predictions, requiring high safety margins and reducing condition monitoring's potential. Likewise,

fatigue tests cannot be carried out at higher frequencies as long as it is not possible to estimate their influence on the component's service life.

Because of the dimensions, measurements of the fluid flow inside propagating fatigue cracks are challenging and have, to the author's knowledge, not yet been performed. Fatigue cracks are small and have only a narrow cross-section compared to their length. Simulation of the fluid-structure interaction using the fluid and solid mechanics' governing equations is an alternative to direct measurements. In recent years, numerical simulations have become highly popular as computing performance increased. In addition to the fundamental understanding of the relevant mechanisms, a simulation can test many parameter variations with relatively little effort compared to experiments. However, simulation of the fluid-structure interaction inside fatigue cracks is challenging due to the different dimensions resulting in multi-scale models. In this work, reduced-order models are developed to address these difficulties, and an approach to simulate the fluid-structure interaction in fatigue cracks of pressurized components is presented. The developed simulation approach is demonstrated on a test specimen, and experiments were conducted to validate the developed models.

The following work is structured into seven chapters:

Chapter 2 focuses on a literature-based analysis of fluid-structure interaction. Initially, the basics of fatigue mechanics and the necessary tools are discussed. Following this, the fundamental fluid and solid mechanics governing equations are introduced, and the mathematical tools for the numeric simulations are derived. At last, studies related to the simulation of the fluid-structure interaction inside fatigue cracks are presented. On that basis, the research gap was identified, and the research hypothesis was defined, along with the research questions that are to be addressed within the scope of this work.

In Chapter 3, the test specimens used to validate the simulation models and to demonstrate the simulation approach are presented. The test specimens are based on the geometry of a hydraulic high-pressure connection. The geometry of the test specimens is designed to facilitate the investigation of the fluid-structure interaction. The simple geometry ensures a defined crack initiation, a short crack initiation phase, and stable crack growth with high repeatability. The desired crack growth is achieved within the designated time interval by preliminary estimations of the crack growth rate.

Chapter 4 consists of the description of the simulation approach and the derivation of the reduced-order models. The first part describes the setup of the structural finite-element analysis with a commercial solver. The finite-element analysis provides the basis for approximating the crack opening displacement with a yield strip model. In the second part, the reduced simulation models are derived and implemented. The section concludes with the two-way coupling of the structural and fluid models to simulate the fluid-structure interaction, followed by a convergence study of the coupled simulation.

The subsequent Chapter 5 focuses on the experiments. At first, the experimental setup is described, followed by the procedure and the optical evaluations. The second part describes the strain measurements and the post-processing. Supplementary filters were implemented for noise suppression, temperature compensation, and the detection of idle times. The flow through the cracked components was measured on a second test rig, and the flow model was parameterized to the surface roughness of the fatigue cracks. At the end of the section, the reduced-order models are validated.

In Chapter 6, the simulation results of the fluid flow inside the crack of the specimens are presented, and the influence of the fluid-structure interaction is discussed. At first, the pressure distribution inside fatigue cracks during dynamic pressure pulses is analyzed. Subsequently, the impact of fluid-structure interaction on fatigue and crack growth is identified, and the dominant mechanisms are discussed. In the last section of this chapter, the parameters influencing the fluid-structure interaction in the crack are determined, and their influence is quantified.

The summary, the scientific contribution, and continuing approaches conclude the work in Chapter 7.

Parts of this work have already been published in [124]–[128].

2 State of Research

In this chapter, the scientific fundamentals and the current state of the research are presented. The first part consists of the basis of material fatigue, the linear-elastic description of the fatigue stress, and the crack propagation laws. The second part describes the mathematical, structural-mechanical, and fluid-dynamic fundamentals. These form the foundation for the subsequent development of reduced simulation models. Finally, related studies are analyzed and assessed in the context of the problem statement. Based on this analysis, the research gap and hypothesis are derived at the end of the chapter.

2.1 Material Fatigue

In contrast to static material strength, fatigue occurs from repeated loads. The service life of components consists of two phases: crack initiation and crack growth. The fatigue crack growth initiates at small defects or cracks. Macroscopic cracks can either already exist due to the manufacturing process or form from micro-fissures in a later stage. In contrast to static failure due to a single overload, fatigue occurs at much lower stress thresholds, and stable crack growth can take place for tens of thousands of cycles before critical instability is attained.
Depending on the component service lifetime, three fatigue regimes are distinguished. In the case of low cycle fatigue, crack growth typically leads to failure after roughly 10^4 cycles. Low cycle fatigue requires the highest stress of the three regimes. For lower stress levels, high cycle fatigue occurs. High cycle fatigue requires about 10^4 and 10^7 load cycles before rupture, [7]. High cycle fatigue is the most relevant fatigue regime, as the component's life is sufficient for most applications, and components are lightweight and efficient. For decades, the general opinion presumed that no crack growth occurs if the stress does not exceed the fatigue limit. In recent years, fatigue

studies of rotating and vibrating devices proved that beyond that, very- and ultra-high cycle fatigue regimes exist, with lifetimes of approximately 10^9 and 10^{12} cycles, respectively, [8], [9].
The technical fracture mechanic describes the stress and displacement field at the crack tip and approximates the crack propagation. In the second part, the state of the research regarding premature crack closure, particularly fluid-induced crack closure, is covered. Crack closure reduces the effective stress amplitude and decreases the crack propagation rate.

2.1.1 Fracture Mechanics

In technical fracture mechanics, cracks are assumed to be omnipresent, [10], [11]. These can be microscopic defects in the range of micrometers or established macroscopic cracks with sizes of millimeters or more. The fracture-mechanical concepts investigate the local stress and displacement field in the vicinity of the crack to estimate the crack propagation.
A crack inside a loaded structure provokes a disturbance of the force flow. If the crack is perpendicular to the stress, the force flow is highly distorted around the crack front and at the crack tip. The distortion is small if the crack is orientated in line with the stress. As a result, cracks always propagate perpendicular to the applied stress. A microscopic defect in line with the stress does not grow, and no macroscopic crack develops. Hence, some loads influence crack growth in multiaxial load conditions, while others are harmless.

2.1.1.1 Crack Modes

From a geometric point of view, cracks are a separation of the material in a specific area. Cracks are classified into three principal modes. The orientation of the crack in relation to the orientation and type of the applied load characterizes the three crack modes. Figure 2.1 depicts the crack faces' displacement and the applied force's direction for each mode. The crack is located in the x-z plane, and the crack front is orientated in the z-direction, [12].

Mode I cracks are caused by stress perpendicular to the crack plane, opening the crack faces. The crack front propagates in the plane normal to the applied

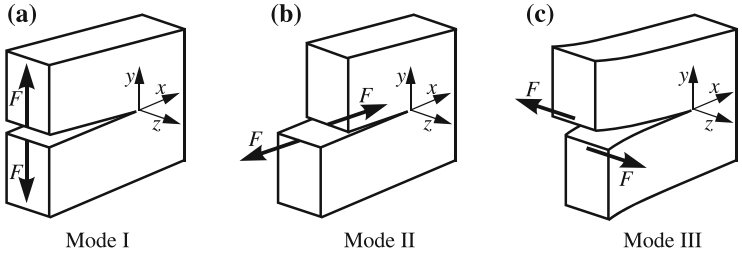

Figure 2.1: Crack opening modes, [13].

force. Mode II and Mode III cracks include all shear stress dominant cracks. Mode II occurs for shear stress perpendicular to the crack front, resulting in the crack faces sliding in the crack's direction. The crack front is orientated in the same plane as the force. In Mode III, cracks arise from shear stress parallel to the crack front. The crack front is located in the plane of the force. The crack faces slide perpendicular to the direction of the crack and the crack front in the direction of the shear stress. The superpositions of crack modes result in mixed mode cracks with the properties of the superposed modes.
In the following, only Mode I cracks are considered. The force perpendicular to the crack provokes the crack faces to separate, resulting in a crack opening displacement. In the case of Mode II and Mode III cracks, the crack faces slide and dislocate against each other. Hence, the crack faces are not separated, and no macroscopic crack opening occurs. Without the crack to open and close, oil flowing into the crack is less likely. However, oil is assumed to increase Mode II and Mode III crack growth by lubrication of the crack faces, [14], [15].

2.1.1.2 Stress and Displacement Field

The stress field in the vicinity of the crack tip characterizes the crack's propagation, with the highest local stress found at the crack tip. In some idealized configurations, analytic calculation of the stress distribution is possible. Based on these elasticity-theoretical solutions for plane and spatial problems, an approximative expression for the immediate vicinity of the crack tip can be derived. For small values of the crack tip radius r, the series expansion approximates the elastic stress field in homogeneous isotropic bodies. The

first term of a series expansion of a two-dimensional (x-y plane) stress field in polar coordinates (r, φ) around the crack tip as shown in [12], is

$$\sigma_{i,j} = \frac{1}{\sqrt{2\pi \cdot r}} \left[K_I \cdot f_{i,j}^{I}(\varphi) + K_{II} \cdot f_{i,j}^{II}(\varphi) \right]. \tag{2.1}$$

This linear elasticity description creates a stress singularity at the crack tip ($r = 0$). As a result, classical strength analysis methods can not be applied to cracks. The approximation introduces the stress intensity factors K_I and K_{II} for Mode I and Mode II, respectively, and the dimensionless functions, $f_{i,j}^{I}(\varphi)$ and $f_{i,j}^{II}(\varphi)$, which depend on the angle φ. This work is limited to pure Mode I cracks, where

$$\begin{aligned} K_I &\neq 0, \\ K_{II} &= 0, \\ \sigma_{xx} &= \sigma_x, \\ \sigma_{yy} &= \sigma_y. \end{aligned} \tag{2.2}$$

For the stress distribution along the x-axis ($\varphi = 0$), then applies:

$$\begin{aligned} \sigma_x &= \frac{K_I}{\sqrt{2\pi \cdot r}}, \\ \sigma_y &= \frac{K_I}{\sqrt{2\pi \cdot r}}, \\ \sigma_{xy} &= 0. \end{aligned} \tag{2.3}$$

The displacement of the crack faces is important when simulating the fluid-structure interaction. In the case of pure Mode I cracks, where the crack face motion is symmetrical to the crack plane in a perpendicular direction, the displacement of the crack faces is denoted as crack opening displacement (COD). The value of the crack opening displacement is two times the motion of the one crack face corresponding to the complete opening produced by the motion of the crack faces. Similar to the stress field in the proximity of the crack tip, the displacement field close to the crack tip can be approximated. The displacement along the crack axis in the x-direction is denoted as $v_x(r, \varphi)$ and the crack opening normal to the plane, which corresponds to the COD

for $\varphi = \pi$, is denoted as $v_y(r, \varphi)$. The approximation of the displacement field for Mode I cracks is given in [12] in polar coordinates as

$$\begin{aligned} v_x(r,\varphi) &= \frac{K_I \cdot (1+\nu)}{E} \cdot \sqrt{\frac{r}{2\pi}} \cdot cos\frac{\varphi}{2} \cdot \left(\kappa - 1 + 2sin^2\frac{\varphi}{2}\right), \\ v_y(r,\varphi) &= \frac{K_I \cdot (1+\nu)}{E} \cdot \sqrt{\frac{r}{2\pi}} \cdot sin\frac{\varphi}{2} \cdot \left(\kappa + 1 + 2cos^2\frac{\varphi}{2}\right). \end{aligned} \tag{2.4}$$

with stress intensity factor K_I, Young's modulus E, Poission's ratio ν, and crack tip radius r. The displacement fields depend on whether it is a plane stress state $\kappa = (3-\nu)/(1+\nu)$ or a plane strain state with $\kappa = (3-4\nu)$.

Plane Stress and Strain. For simplification, the stress field is solved as a two-dimensional problem. The two-dimensional problem is supposed to have either plane stress or plane strain. If the third direction (z) is significantly smaller than the other dimensions, the third direction is assumed to be infinitely small, and the part is reduced to a thin plate. Due to the infinite small third direction, the load in this direction is constant and equal to the surface stress. Hence, the stress is zero if no external surface force is applied, and the stress is denoted as plane stress, as only the planar components are non-zero,

$$\sigma_z = 0, \ \epsilon_z \neq 0 \tag{2.5}$$

whereas the strain ϵ_z can differs from zero.

In the case of a significantly larger dimension, an infinite uniform extent in the third direction is assumed. The strain is constrained by the material extending infinitely. Every strain in the third direction leads to an invalid infinitive displacement. Hence, the strain in the third direction has to be zero,

$$\sigma_z \neq 0, \ \epsilon_z = 0 \tag{2.6}$$

denotated as plane strain.

2.1.1.3 Stress Intensity Factors

The stress intensity factor (SIF) represents the intensity of the stress field at the crack tip, [12]. Due to the stress singularity at the crack tip, it is impossible to evaluate the stress at the crack tip based on linear elasticity. Instead, the SIF is used to assess the fatigue damage and to calculate the crack propagation

rate. The SIF depends on the applied load, the component's geometry, the crack length, and the crack's orientation to the load but is independent of the material properties. The Mode I stress intensity factor is defined following equation ((2.3)) as

$$K_I = \sigma \cdot \sqrt{\pi l_0} \cdot Y_I \tag{2.7}$$

with characterizing crack length l_0. Y_I is the geometry factor accounting for the geometry of the crack and the component. The geometry factor is $Y = 1$ for an internal crack in an infinitely extended plate under tensile loading (Griffith crack). Geometry factors for some particular geometries are defined in [16]–[18]. In general, geometry factors have to be approximated or simulated by numeric methods. The stress σ is defined as the fictional loading of the intact part without defect.

Besides the mentioned analytic solutions, stress intensity factors can be determined by numerical or experimental methods, [19]–[23]. Approximation of the SIF is possible by extrapolation of the stress or displacement fields around the crack. Regarding the finite-element method solution, one of the main problems is the inaccuracy of the linear-elastic solution close to the crack tip due to the non-infinitesimal size of the crack-tip element. A linear interpolation of the stress intensity factor over several elements in the proximity of the crack tip prevents the discretization error. Rearranging equation (2.3) and equation (2.4) (at $\varphi = \pi$) for $r \longrightarrow 0$ leads to

$$K_I = \lim_{r \to 0} \sqrt{2\pi r} \cdot \sigma_{y,FEM} \tag{2.8}$$

for the stress field method and

$$K_I = \lim_{r \to 0} \frac{E}{(\kappa + 1)(1 + \nu)} \sqrt{\frac{2\pi}{r}} v_{y,FEM} \tag{2.9}$$

for the displacement field method.

The displacement field method to determine the SIF might produce more accurate results than the stress field method, [12]. In contrast to stress or energy-related approaches, determining the SIF from the displacement fields is possible if an approximation of the crack opening displacement, e.g., by weight function, is utilized.

2.1.1.4 Plastic Zone

The linear-elastic solutions of the stress field lead to a stress singularity at the crack tip. However, the yield strength of materials limits the occurring stress, and instead of the singularity, the material undergoes plastic deformation, [24]. The area around the crack tip, where the material is plastically deformed, is denoted as the plastic zone. Many studies conclude that the size of the plastic zone (PZS) is an essential parameter regarding the initiation and propagation of fatigue cracks, [24]–[27]. The plastic deformation at the crack tip increases the displacement of the crack faces, influencing the effective cross-section for the oil flow and is, hence, also relevant for the fluid-structure interaction. Irwin presented a model to estimate the size of the plastic zone under the assumption of an infinite plate, [28]. Figure 2.2 depicts the approach of Irwin's model, limiting the stress to the yield strength of the material and introducing a fictitious crack tip by balancing the stress distribution to the remote force field. In the case of a Mode I loading in a plane strain state, the size of the plastic zone is given as

$$\omega_{PZ} = \frac{(1-2\nu)^2}{\pi}\left(\frac{K_I}{\sigma_Y}\right). \tag{2.10}$$

Recent studies indicate that Irwin's model underestimates the total size of the plastic zone when the remote stress approaches the yield strength, [27]. More accurate estimates of the plastic zone size can be achieved in FEM simulations with non-linear material hardening laws, [24], [29].

2.1.1.5 Crack Propagation Laws

In the previous sections, the stress and displacement fields around the crack tip have been described. Subsequently, methods and approaches have been presented to assess the stress intensity and calculate the size of the plastic zone. Under cyclic loading, the crack tip undergoes a repeated stress amplitude, and the crack grows with each load cycle. The crack propagation rate is defined as the average increase in the crack's length per cycle da/dN. The crack propagation rate depends, among others, on the stress amplitude, defined as the difference

$$\Delta K_I = K_{I,max} - K_{I,min} \tag{2.11}$$

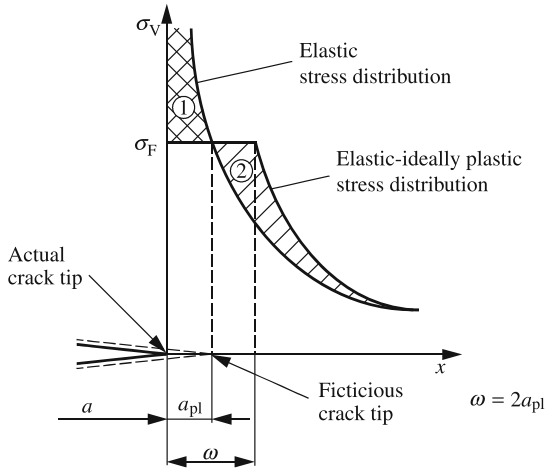

Figure 2.2: Linear elastic and ideal plastic stress distribution at the crack tip of a crack in an infinite plate with the elastic stress distribution (1) and the ideal plastic stress distribution (2), [13].

between the minimal and maximal stress intensity factor of each load cycle. Besides the stress amplitude, the stress ratio of the load R_{SR},

$$R_{SR} = \frac{K_{I,min}}{K_{I,max}} \tag{2.12}$$

influences crack propagation. In the past, several crack propagation laws have been proposed to estimate the crack propagation rate. Among them are the Paris' law ([30]) and the NASGRO equation ([31]). The crack propagation rate with respect to the stress intensity in Figure 2.3 is divided into three regions. No crack propagation is observed below a certain threshold $K_{I,th}$. Stable crack growth occurs above this threshold as long as the stress intensity remains below a critical intensity K_{IC} at which unstable crack growth follows.

Paris-Erdogan Law. Paris and Erdogan presented a crack propagation law (Paris' law) for the region of stable crack growth as a function of the amplitude of the stress intensity factor, [30]. The Paris' law estimates the crack propagation rate by

$$\frac{da}{dN} = C_P \Delta K^{n_P}, \ \Delta K_{I,th} < \Delta K_I < \Delta K_{IC}. \tag{2.13}$$

The exponent $n \in \mathbb{R}$ is a material constant while the coefficient C depends on the material and the stress ratio, [32]. The Paris' law does not account for the stress intensity threshold or the critical stress limit (Figure 2.3a), [33].

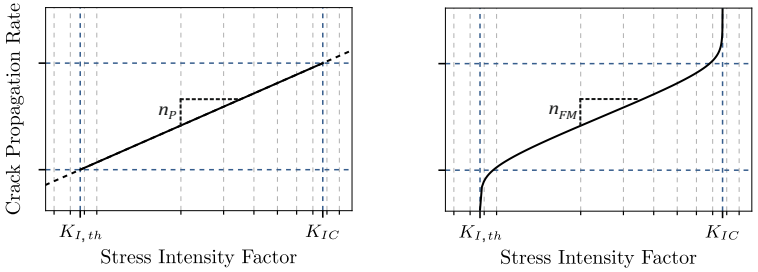

(a) Paris' Law. **(b)** NASGRO Equation.

Figure 2.3: Paris' Law and NASGRO Equation for the estimation of the crack propagation rate da/dN with the crack growth coefficient n_P and n_{FM}.

NASGRO Equation. Another approach developed by Forman et Mettu, [31], takes into account the entire crack propagation curve (Figure 2.3b). The NASGRO equation depends on the material constants C_{FM}, n_{FM}, $\Delta K_{I,th}$, K_{IC}, p_{FM}, and q_{FM} and is defined as

$$\frac{da}{dN} = C_{FM} \cdot \left[\left(\frac{1-\gamma}{1-R_{SR}} \right) \cdot \Delta K_I \right]^{n_{FM}} \cdot \frac{\left(1 - \frac{\Delta K_{I,th}}{\Delta K_I}\right)^{p_{FM}}}{\left(1 - \frac{K_{I,max}}{K_{IC}}\right)^{q_{FM}}}. \tag{2.14}$$

The crack opening function $\gamma(R_{SR})$ depends on the stress ratio R_{SR} and is calculated as

$$\gamma = \max\left(R_{SR}, A_0 + A_1 R_{SR} + A_2 R_{SR}^2 + A_3 R_{SR}^3\right) \tag{2.15}$$

with coefficients

$$\begin{aligned} A_0 &= \left(0.825 - 0.34\alpha_{FM} + 0.05\alpha_{FM}^2\right) \cdot \cos\left(\frac{\pi}{2} S_R\right)^{1/\alpha_{FM}}, \\ A_1 &= \left(0.415 - 0.071\alpha_{FM}\right) \cdot S_R, \\ A_2 &= 1 - A_0 - A_1 - A_3, \\ A_3 &= 2A_0 + A_1 - 1, \end{aligned} \tag{2.16}$$

which depend on the material constants α_{FM} and S_R. In contrast to the Paris' law, the NASGRO-Equation takes into account the stress intensity threshold, the critical intensity, and the stress ratio. Hence, no specific constants for different stress ratios are required. The influence of crack closure is modeled in the opening function $\gamma(R_{SR})$, [34].

2.1.1.6 Crack Initation

The service life of components can be divided into the crack initiation phase and the crack propagation phase. During the crack initiation phase, no macroscopic crack exists, and the crack initiation is happening on a microstructural scale, [35], [36]. The crack initiation phase can significantly contribute to the total service life. The time required for the crack initiation largely depends on the surface preparation, material properties, and local stress concentrations, [37]. An artificial defect in the area of the highest local stress, e.g., introduced in the milling process of notches, can reduce the crack initiation time to a minimum.

2.1.2 Crack Closure

Elber, [38], [39], has investigated the closing of fatigue cracks for a cyclic tensile load of constant amplitude in air. The investigation has shown that the crack faces come into contact even before reaching the minimal load. The contact of the crack faces prevents the crack from returning to its initial state. The residual deformation due to this premature crack closure provokes a stress field at the crack tip, even in the unloaded state. When increasing the load again, the crack faces remain in contact until a specific tensile stress is reached. In his experiments, the crack faces remained in contact for most of the tensile stress cycle.
The stress amplitude is one of the main parameters that influences the fatigue crack propagation rate. Increasing the minimal stress reduces the effective stress amplitude and increases the stress ratio. Figure 2.4 shows the effect of crack closure on the nominal and the effective stress amplitude. While the maximal stress is not altered by crack closure, the effective stress amplitude and, hence, the crack propagation rate decreases, [40]. Especially at near-threshold levels, crack closure can significantly alter the crack propagation, [41].

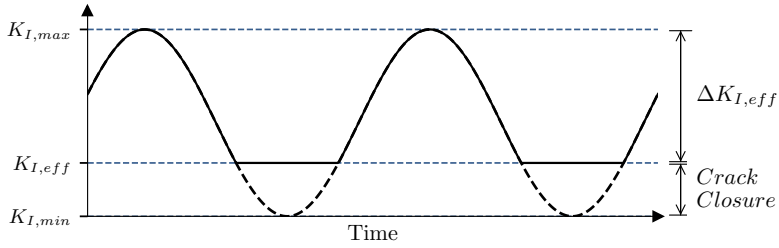

Figure 2.4: Reduced effective damage amplitude $\Delta K_{I,\text{eff}}$ due to crack closure.

In the past, various reasons for crack closure have been investigated, among them material plasticity, oxidation, surface roughness, phase transformation, viscous fluids, and artificially enforced crack closure, [41]–[44]. Figure 2.5 depicts the mechanism behind roughness-induced, oxidation-induced, and fluid-induced crack closure. Each prevents the crack faces from returning to their initial state.

Strain measurements in the vicinity of the crack is a widely used method to provide evidence of crack closure, [45]–[47]. In [45], Ray et al. measured the crack opening displacement with the strain gauges installed at the crack mouth. Once the crack faces are separated, the crack opening displacement should increase linearly with a higher gradient. The measured strain showed a clear transition between the initial gradient, where the crack faces remained in contact, and the subsequent gradient, where the crack faces were separated. Ray et al. assumed that the start of the linear gradient corresponded to the crack opening stress ($K_{I,\text{eff}}$). In further experiments, Xu et al. showed that both the conventional measurement of the crack opening displacement at the crack mouth and indirect strain measurements near the crack tip permitted tracing of crack closure, [46].
When the crack mouth is located inside hydraulic components, measuring the crack opening displacement at the crack mouth is challenging. However, indirect strain measurements near the crack tip are applicable to validate fluid-induced crack closure.

Roughness-induced crack closure occurs when the crack faces shift against each other. Shifting of the crack faces can be caused, for example, by shear stress (Mode II / III) or by plastic deformation of the material (Mode I - III).

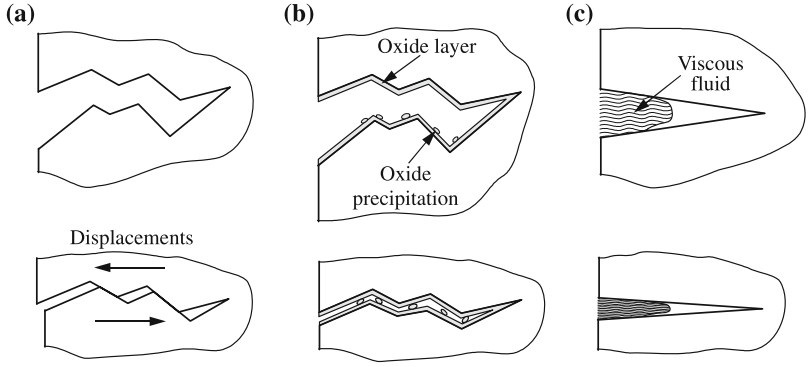

Figure 2.5: Schematics of crack closure mechanisms (a: roughness-induced, b: oxid-induced, c: fluid-induced), [13].

Hence, the surface geometry no longer interlocks if the crack flanks are not smooth. [41]
In addition to premature crack closure, the early contact of the surface reduces the cross-section for the oil flow. Roughness-induced crack closure can thus reduce the volume flow inside the crack. The incompatible crack faces can seal the crack off entirely and prevent the oil from flowing out.

While many studies have investigated plasticity-induced and roughness-induced crack closure, crack closure provoked by viscous fluids has received far less attention. In contrast to roughness-induced crack closure, which occurs quasi-instantaneously, fluid-induced crack closure depends on the fluid flow.

2.2 Computational Mechanics

The following section presents the fundamentals relevant to the numerical simulation of fluid-structure interaction. The necessary fundamentals can be divided into structural mechanics and fluid dynamics. The first part will introduce the finite-element method and the yield stripe model as computational methods for structural mechanics. The fluid dynamic governing equations are derived in the second part, and the finite-difference and finite-volume

methods as approximative solutions for computational fluid dynamics are presented.

2.2.1 Structural Mechanics

Nowadays, the state of the art provides many techniques for the numerical calculation of material deformations, [48]. Many of these are already implemented in commercial software, such as Ansys Mechanical, [121], and have been numerically optimized. The finite element method (FEM) is the basis of most modern three-dimensional structural simulations. The yield strip model offers a simple model for numerical simulation of the crack flank displacement. The yield strip model avoids the stress singularity of a linear elastic model at the crack tip by virtually extending the physical crack.

The principal governing equation of structural mechanics is the equilibrium of forces. For a one-dimensional rod, the equilibrium of forces is simplified to

$$\frac{d}{dx}\sigma_x - f_b = 0, \tag{2.17}$$

with the body force f_b. In the general three-dimensional case, the derivative is expressed by the aid of the differential operator $\mathbf{D}_\sigma$ as

$$\mathbf{D}_\sigma \vec{\sigma} - \vec{f_b} = 0 \tag{2.18}$$

with the force vector $\vec{f_b}$.

The one-dimensional Hook's law defines the principle of linear elasticity as

$$\sigma_x = E\epsilon_x \tag{2.19}$$

with Young's modulus E, the stress σ_x, and the strain ϵ_x in x-direction. In multi-dimensional formulations, the Young's modulus is replaced by the stiffness matrix K as

$$\vec{\sigma} = \mathbf{K}\vec{\epsilon} \tag{2.20}$$

In the same way, the kinematic boundary condition

$$\epsilon_x = \frac{dv_x}{dx} \tag{2.21}$$

can be written in general three-dimensional form using the differential operator $\mathbf{D}_v$ as

$$\vec{\epsilon} = \mathbf{D}_v \vec{v}. \tag{2.22}$$

2.2.1.1 Finite-Element Method

With the Galerkin method, the equilibrium of forces can be expressed in integral form over a control volume v as

$$\int_v \left(\mathbf{D}_v \partial\vec{v}\right)^T \mathbf{D}_\sigma \vec{\sigma} \left(\mathbf{D}_v \vec{v}\right) dv = \int_v \vec{f}_b dv. \tag{2.23}$$

The finite-element method is an approximative method to calculate a numeric solution. The FEM divides the solution space into a discrete number of elements. Each element has defined basis functions that interpolate the field variables, and the equilibrium condition is solved locally for each element. Integration of the integral form over the control volumes leads eventually to the quasi-static finite-element formulation defined as a set of non-linear equations

$$\mathbf{K}_e \vec{v} - \vec{F} = 0 \tag{2.24}$$

with the unknown displacement $\vec{v}$, the generalized force $\vec{F}$, and the element stiffness matrix $\mathbf{K}_e$, [49].

The system of non-linear equations is then solved iteratively, e.g., by the Newton-Raphson method, [49]. Depending on the problem formulation, various element types and basis functions have been developed, [50]. Due to their simple integrability and differentiability, first- or second-order polynomials are suitable and commonly used basis functions. Higher order basis functions can increase the solution accuracy but worsen the numerical stability and performance, [51].

2.2.1.2 Yield Strip Model

Irwin's model, [28], lays the physical foundation for the yield strip model (YSM). Linear-elastic calculation of the crack stress leads to a stress singularity at the crack tip. According to Irwin, a plastic deformation occurs at the crack tip (plastic zone). Dougdale first described the YSM analytically, [52]. To avoid the stress singularity at the crack tip, the yield strip model fictively extends the crack by the length of the plastic zone. Figure 2.6 visualize an elastic crack opening shifted by the size of the plastic zone and the following plastic crack opening displacement. The fictive crack can be described as a superposition of two elastic loads, the elastic solution plus the plastic approximation, [53]. The

plastic deformation is implemented as uniform stress on the last non-fictive segment of the crack, provoking the equivalent deformation.

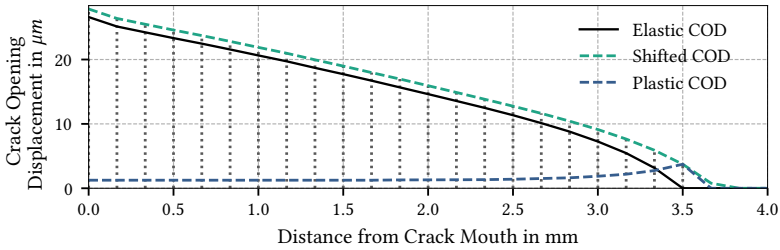

Figure 2.6: Seperation of elastic and plastic crack opening displacement following Irwin's model with dotted yield stripes.

Complex crack growth processes can be simulated numerically by division of the crack into yield strips. Investigations of crack growth with yield strip models are available from several related areas, e.g., for large-scale yielding, [54], plasticity-induced crack closure, [55], [56], analysis of the influence of surface flaws, [57], or calculation of the fatigue threshold, [58].

2.2.2 Fluid Dynamics

The governing equations of fluid dynamics describe the fluid's physics and are the basis for the numeric fluid models. Geometric assumptions and negligence of physical properties lead to simplified formulations. The following subsection presents first the fluid's governing equations and derives the Navier-Stokes equations. Subsequently, the thin-film approximation and the averaged Reynolds equation are derived from the Navier-Stokes equations.

2.2.2.1 Flow equations

The governing equations of fluid mechanics can be derived from the conservation laws. Generally, the conservation laws for three extensive properties are formulated: mass, momentum, and energy. In this case, the conservation laws are formulated within a spatial control volume in integral form.

The conservation laws for a control volume $V = V(t)$ and the intensive property Φ is given by the Reynolds transport theorem as, [59],

$$\frac{d}{dt}\int_V \Phi dV = \frac{d}{dt}\int_v \Phi dv + \oint_S \Phi(\vec{u}\cdot\vec{n})dS. \tag{2.25}$$

The left side of the integral represents the total amount of the property Φ in the volume V. The right side represents the instantaneous change of the property Φ within the spatial fixed control volume v plus the net flow of Φ across its surfaces S with surface normal $\vec{n}$. The intensive property Φ is $\Phi = \rho$ for the conservation of mass and $\Phi = \rho\vec{v}$ for the conservation of momentum.

Conservation of Mass. The integral form of the conservation of mass follows directly from equation (2.25) by substituting $\Phi = \rho$ and setting the left side equal to zero, as mass is neither created nor destroyed,

$$0 = \frac{d}{dt}\int_v \rho dv + \oint_s \rho(\vec{u}\cdot\vec{n})dS. \tag{2.26}$$

By applying the Gauss' divergence theorem, equation (2.26) is simplified and brought to the differential form, [59], being,

$$\frac{\partial\rho}{\partial t} + \frac{\partial(\rho u_x)}{\partial x} + \frac{\partial(\rho u_y)}{\partial y} + \frac{\partial(\rho u_z)}{\partial z} = 0. \tag{2.27}$$

Conservation of Momentum. The Navier-Stokes equations are derived from the conservation of momentum. In contrast to the mass, the momentum changes as a result of the acting forces. The governing equation is given by Newton's second law as

$$\frac{d(m\vec{u})}{dt} = \frac{d}{dt}\int_V \rho\vec{u}dV = \sum F. \tag{2.28}$$

Substituting $\Phi = \rho\vec{u}$ in equation (2.25) leads to

$$\sum F = \frac{d}{dt}\int_v \rho\vec{u}dv + \oint_S \rho\vec{u}(\vec{u}\cdot\vec{n})dS. \tag{2.29}$$

The forces acting on the control volume of a fluid are either body forces (gravity, inertial forces, etc.) or surface forces (pressure, shear stress, etc.). The body forces are represented by $\rho\vec{f_b}$. For viscous fluids, the surface forces

consist of the normal pressure forces and the shear stress caused by the internal friction of the fluid. The Navier-Stokes equation for compressible, Newtonian fluids are given in [60]. For incompressible Newtonian fluids ($\rho = const$), the Navier-Stokes equation simplifies to, [61],

$$\rho \cdot \left(\frac{\partial \vec{u}}{\partial t} + (\vec{u} \cdot \nabla)\vec{u} \right) = -\nabla p + \eta \cdot \nabla^2 \vec{u} + \rho \vec{f_b} \tag{2.30}$$

with the dynamic viscosity η, ∇p the gradient of p, $(\vec{u} \cdot \nabla)$ the Euclidean scalar product of the velocity vector with the gradient, and $\nabla^2 \vec{u}$ the Laplace-operator as

$$\nabla^2 \vec{u} = \frac{\partial^2 \vec{u}}{\partial x^2} + \frac{\partial^2 \vec{u}}{\partial y^2} + \frac{\partial^2 \vec{u}}{\partial z^2}. \tag{2.31}$$

Conservation of Energy. The third conservation law often connected with computational fluid dynamics is energy conservation. For example, this additional equation is required when considering turbulent flows or heat diffusion. In the scope of this work, the investigated flows were assumed to be isothermal and laminar, and energy conservation was not exploited.

2.2.2.2 Reynolds Equation

The Reynolds equation, developed in 1886 by Osborne Reynolds, [62], is based on the assumption that the height of the fluid film (y-direction) is several orders of magnitude smaller than its extent in $x-$ and $z-$ direction.

The thin film simplifications follow from normalizing the variables in the Navier-Stokes equation. Given the normalized coordinates x^*, y^*, z^* defined as,

$$(x^*, y^*, z^*) = \frac{1}{L_{xz}} \left(x, \frac{1}{\zeta} y, z \right), \tag{2.32}$$

with the aspect ratio ζ and the characteristic length L_{xz}. The aspect ratio must be $\zeta < 0.1$ for the thin-film simplifications to be accurate. For langer aspect ratios, Szeri reported deviations of the thin-film pressure of more than 16%, [63].
The fluid flow is characterized by the velocity along the film, which is denoted

by Ψ. Given the characteristic length L_y and the expected velocity Ψ, the Reynolds number Re and the reduced Reynolds number Re_ζ are defined by

$$\begin{aligned} Re &= \frac{\rho L_y \Psi}{\eta} \\ Re_\zeta &= \zeta Re, \end{aligned} \tag{2.33}$$

respectively.

The thin-film approximation is derived from the Navier-Stokes equations by substituting ζ, Re_ζ and all other variables by their normalized counterpart $(\cdot)^*$ in the Navier-Stokes equations and setting $\zeta^2 \to 0$. The complete derivation is given in [63], resulting in

$$\begin{aligned} Re_\zeta \rho^* \left(\frac{\partial u_x^*}{\partial t^*} + u_x^* \frac{\partial u_x^*}{\partial x^*} + u_y^* \frac{\partial u_x^*}{\partial y^*} + u_z^* \frac{\partial u_x^*}{\partial z^*} \right) &= -\frac{\partial p^*}{\partial x^*} + \frac{\partial}{\partial y^*} \left(\eta^* \frac{\partial u_x^*}{\partial y^*} \right), \\ 0 &= -\frac{\partial p^*}{\partial y^*} \\ Re_\zeta \rho^* \left(\frac{\partial u_z^*}{\partial t^*} + u_x^* \frac{\partial u_z^*}{\partial x^*} + u_y^* \frac{\partial u_z^*}{\partial y^*} + u_z^* \frac{\partial u_z^*}{\partial z^*} \right) &= -\frac{\partial p^*}{\partial z^*} + \frac{\partial}{\partial y^*} \left(\eta^* \frac{\partial u_z^*}{\partial y^*} \right). \end{aligned} \tag{2.34}$$

In addition to the thin-film approximation, four more assumptions were made by Reynolds in [62]:

1. The compressibility is negligible.
2. The viscosity is constant.
3. The lubricant inertia is negligible.
4. The lubricant flow is laminar.

Assumptions (1) and (2) lead to ρ and η being constant. Both assumptions are independent of the thin-film geometry and are questionable in many applications. In lubrication and hydraulics, fluid compressibility is often not negligible. The Boussinesq approximation offers an alternative to completely neglecting the compressibility, [64]. In this case, the fluid compressibility is neglected in the Navier-Stokes equation but taken into account for the body forces and the conservation of mass. The assumption of a constant viscosity is generally valid for isothermal flows at low pressure, [65], [66].
The third assumption, neglecting the fluid inertia, is equal to assuming

$Re_\zeta << 1$. By applying the third assumption, the left parts of equation (2.34) are equal to zero, and the equations simplify (in primitive variables) to:

$$\begin{aligned} \frac{\partial p}{\partial x} &= \eta \frac{\partial^2 u_x}{\partial y^2}, \\ \frac{\partial p}{\partial z} &= \eta \frac{\partial^2 u_z}{\partial y^2}. \end{aligned} \tag{2.35}$$

Integration of the simplified equations with respect to y with the following boundary conditions,

$$\begin{aligned} u_x(y=0) &= \beta_1, \quad u_x(y=h) = \beta_2 \\ u_z(y=0) &= 0, \quad u_z(y=h) = 0 \end{aligned} \tag{2.36}$$

gives the velocity distribution of the Poiseuille-Flow with moving walls

$$\begin{aligned} u_x(y) &= \frac{1}{2\eta}\frac{\partial p}{\partial x}(y^2 - yh) + \left(1 - \frac{y}{h}\right)\beta_1 + \frac{y}{h}\beta_2, \\ u_z(y) &= \frac{1}{2\eta}\frac{\partial p}{\partial z}(y^2 - yh). \end{aligned} \tag{2.37}$$

At last, the conservation of mass is exploited and equation (2.27) integrated across the film (with respect to y for $y \in [0, h]$). Substituting u_x and u_z results in the most common form of the *Reynolds equation* for lubricating pressure films

$$\frac{\partial}{\partial x}\left(\frac{h^3}{\eta}\frac{\partial p}{\partial x}\right) + \frac{\partial}{\partial z}\left(\frac{h^3}{\eta}\frac{\partial p}{\partial z}\right) = 6(\beta_1 - \beta_2)\frac{\partial h}{\partial x} + 6h\frac{\partial(\beta_1 + \beta_2)}{\partial x} + 12(\Lambda_2 - \Lambda_1). \tag{2.38}$$

Λ_1 and Λ_2 are the motion of the rigid bodies in contact with the lubricant in the direction of the film thickness, whereas β_1 and β_2 are the motion of the bodies in the direction of the flow.

2.2.2.3 Averaged Reynolds Equation

The Reynolds equation is only valid for smooth surfaces, implying that the surface roughness is negligible compared to the film thickness. Neither mixed friction regimes nor fatigue cracks have smooth surfaces. The surface geometry is investigated for fatigue cracks in Section 5.1.3.2.

Patir and Cheng, [67], developed an average Reynolds equation for the mixed lubrication regime by averaging the Reynolds equation over a flow section. At first, they defined the local film thickness $h_T(x,z)$ as

$$h_T(x,z) = h(x,z) + \omega_x(x) + \omega_z(z), \tag{2.39}$$

where $h(x,z)$ is the nominal film thickness. ω_x and ω_z are random roughness amplitudes being Gaussian distributed with zero mean. Integration of equation (2.38) leads to the volume flows per unit length as

$$\begin{aligned} q_x(x,z) &= -\frac{h_T(x,z)^3}{12\eta}\frac{\partial p}{\partial x} + \frac{\beta_1+\beta_2}{h_T(x,z)}, \\ q_z(x,z) &= -\frac{h_T(x,z)^3}{12\eta}\frac{\partial p}{\partial z}. \end{aligned} \tag{2.40}$$

Hence, q_x and q_z are random functions with respect to $h_T(x,z)$. If q_x and q_z are random variables, the expected values $\mathbb{E}(q_x)$ and $\mathbb{E}(q_x)$ correspond to the average of q_x and q_z over the lengths Δx and Δz. The line integrals along x and z are defined as

$$\begin{aligned} \mathbb{E}(q_x) &\approx \frac{1}{\Delta z}\int_z^{z+\Delta z} q_x dz, \\ \mathbb{E}(q_z) &\approx \frac{1}{\Delta x}\int_x^{x+\Delta x} q_z dx. \end{aligned} \tag{2.41}$$

Δx and Δz must be sufficiently large that the regarded section includes many asperities.

At last, [67], defined the pressure flow factors θ_x, θ_y, and the shear flow factor θ_s in such a way that the expected flows are equal to

$$\begin{aligned} \mathbb{E}(q_x) &= -\theta_x\frac{h(x,z)^3}{12\eta}\frac{\partial p}{\partial x} + \frac{\beta_1+\beta_2}{h(x,z)} + \frac{\beta_1-\beta_2}{2}\theta_s, \\ \mathbb{E}(q_z) &= -\theta_z\frac{h(x,z)^3}{12\eta}\frac{\partial p}{\partial z}. \end{aligned} \tag{2.42}$$

Equation (2.42) corresponds to the Reynolds equation evaluated with the nominal film thickness, multiplied by the pressure flow factors. The shear flow factor accounts for the fluid flow generated by the additional shear stress of asperities perpendicular to the direction of motion.

If the motion between the two bodies is equal to zero, e.g., for pure Mode I fatigue cracks, $\beta_1 = \beta_2 = 0$, the shear stress factor equals zero. The pressure flow factors depend on the nominal film thickness h and the surface roughness. If the surface roughness is not isotropic, individual flow factors for each flow direction are required, [68].
An overview of general numerical and analytical approaches to determine the flow factors for rough surface pairs is given in [69]. Teale and Lebeck have in [70] further investigated the roughness distribution and its influence on the flow factors as well as the impact of isotropic and non-isotropic surfaces. Harp and Salant extended the average flow model in [71] with a cavitation model due to the motion of the surfaces. In [72], optical topographical measurements have been performed to determine the corresponding flow factors.

2.2.2.4 Finite-Difference Method

The finite-difference method (FDM) is a discretization method to approximate the solution of partial differential equations. In contrast to the finite-element and finite-volume methods, the finite-difference method requires an orthogonal grid. In the scope of this work, however, the finite difference method will solely be applied to one-dimensional problems. Figure 2.7 depicts an example of a 1D grid for the finite-difference method. This work uses the indices n and k for spatial and temporal grids and i or j otherwise.

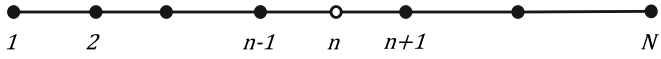

Figure 2.7: Example of an unregular 1D cartesian grid for the FDM.

The approach of the finite-difference method is based on a Taylor series expansion of the intensive property Φ around the grid points, [59]. The Taylor series around the grid point x_i is given as,

$$\Phi(x) = \Phi(x_i) + (x - x_i)\left(\frac{\partial \Phi}{\partial x}\right)_i + \frac{(x - x_i)^2}{2!}\left(\frac{\partial^2 \Phi}{\partial x^2}\right)_i + O\left(\frac{\partial^3 \Phi}{\partial x^3}\right), \tag{2.43}$$

with the omitted higher order terms $O\left(\frac{\partial^3 \Phi}{\partial x^3}\right)$. The FDM assumes that terms of order two or higher are negligible if the grid is sufficiently dense. In consequence, the first derivative is obtained by rearranging equation (2.43)

and substitution of $x = x_{i-1}$ for the backward difference or $x = x_{i+1}$ for the forward difference as

$$\begin{aligned}\left(\frac{\partial\Phi}{\partial x}\right)_i &\approx \frac{\Phi_{i+1} - \Phi}{x_{i+1} - x_i} - O(\Delta x),\\ \left(\frac{\partial\Phi}{\partial x}\right)_i &\approx \frac{\Phi - \Phi_{i-1}}{x_i - x_{i-1}} - O(\Delta x).\end{aligned} \tag{2.44}$$

A third difference is possible, when using both x_{i+1} and x_{i-1}, denoted as central-difference

$$\left(\frac{\partial\Phi}{\partial x}\right)_i \approx \frac{\Phi_{i+1} - \Phi_{i-1}}{x_{i+1} - x_{i-1}} - O(\Delta x)^2. \tag{2.45}$$

The notation $O(\Delta x)$ shows the order of the truncation error due to the neglection of the higher-order terms. The central difference scheme can be more accurate than the forward- or backward-difference scheme as it has a second-order truncation error, [60]. The truncation error decreases with decreasing step size Δx, and all three differences are exact for $\Delta x \to 0$.

2.2.2.5 Finite-Volume Method

The Finite-Volume Method (FVM) divides the solution domain into a finite number of control volumes and then creates nodes at their center. In contrast to the FEM method, the control volumes are defined by their boundaries and not by the location of the node. The conservation equations for a variable Φ are expressed in integral form. The volume integral of the divergence is transformed to a surface integral by application of the divergence theorem [59].

$$\int_S (\rho\Phi)\vec{u} \cdot \vec{n} dS = \int_S \nabla\Phi \cdot \vec{n} dS + \int_V \Phi dV \tag{2.46}$$

The volume integral is approximated by the assumption of a constant value for the variable Φ over the control volume. This results in the integral being replaced by the product of the value of the variable at the i-th node and the size of the control volume ΔV.

$$\int_V \Phi dV \approx \Phi_i \Delta V \tag{2.47}$$

The surface integral is the sum of the surface integrals of all faces of the control volume. The integral of each face can be approximated by the midpoint rule [59]. According to this rule, the surface integral of the variable Φ over the surface S is replaced by the value of the variable Φ_i at the center of the i-th face multiplied by the corresponding face area S_i. Summed over all faces, this leads to

$$\int_S \Phi dS = \sum_i \Phi_i S_i \tag{2.48}$$

In the finite-volume method mesh, the value of the variables is known at the nodes in the center of the control volume, and the volume integrals can be calculated without interpolation. The values at the center points of the surfaces, however, are unknown, and the surface integrals cannot be calculated. Numerous possibilities to interpolate the surface values are available [73]. Among them is the upwind interpolation scheme (UDS), taking the next nodal value in the direction of the flow. The UDS is a first-order interpolation scheme, resulting in an interpolation error with high numerical diffusion but no oscillation. Another possibility is the central differencing scheme (CDS), a second-order interpolation scheme. The CDS interpolates the surface center point linearly by the neighboring nodes. The various interpolation schemes distinguish themself by the approximation error, the numerical diffusion, and the oscillation behavior.

2.3 Related Work

In the following, research related to the fluid-structure interaction in fatigue cracks in hydraulic components is analyzed. The literature review is separated into a section for simulation approaches for fluid-structure interaction (FSI) and a section regarding studies related to the fracture mechanic influence of FSI. Besides the hydraulic components, lubricated contacts and submerged specimens have fatigue cracks where FSI occurs. Lastly, studies focusing on fluid flow through narrow cracks are examined. Modeling the fluid flow through narrow cracks is an important prerequisite for the simulation of the FSI.

2.3.1 Fluid-Structure Interaction Simulation

Various numerical approaches have been developed to simulate the fluid and solid domains' interaction. Many approaches limit the fluid-structure interaction (FSI) to one-way coupled problems, [59]. The aerodynamics of a rigid body is an example of a one-way coupled problem. The body remains rigid while the fluid provokes a surface force, [74]. Alternatively, the fluid force and the motion (deformation) of the structure are taken into account, e.g., in the case of a sinking ship. Two-way coupled FSI requires simulation of a solid and a fluid domain, [75].

Two-way coupled approaches can be divided into monolithic and partitioned approaches. In the monolithic case, a mathematical framework is used for both domains. This approach is generally suitable for specific problems, as an adapted mathematical formulation is necessary to integrate both domains in a single mathematical framework, [75]. In the partitioned case, the fluid and solid domains are modeled separately. However, this case requires an interface between the two domains. If the interface moves, e.g., due to a displacement of crack faces, adapting the mesh (re-meshing) and tracking the interface is challenging.

One possibility to reduce or avoid re-meshing in the case of a moving interface is the arbitrary lagrangian-eulerian (ALE) approach, [76], [77]. This approach combines a Lagrangian reference system with an Eulerian reference system. For example, the fluid domain is simulated in a Lagrangian mesh, while the interface and the solid domain are defined in an Eulerian reference system. Difficulties arise with large deformations, which can lead to mesh degeneration, [77]. Examples of methods with an ALE approach include the immersed boundary (IB) method, [78], or the extended immersed boundary method (EIBM), [79].

An alternative to the ALE approach is the fixed grid approach. This approach does not adapt the mesh and instead describes the interface explicitly, e.g., by a Lagrangian interface marker, or implicitly, e.g., by level sets, [80]. A simulation method with a fixed grid approach is the extended finite element method (XFEM). The XFEM method has proven suitable for many research areas requiring simulations with moving interfaces. For example, moving FSI interfaces or simulation of crack propagation, [81]. As an extension to the original FEM methods, the concept of the XFEM adds a term to the element formulation to include the crack interface. Hence, it allows the simulation

of crack propagation without re-meshing or a priori adjusted meshes but increases the model complexity, [82].

XFEM simulations were used in [83], [84] to simulate the crack propagation due to the fluid-structure interaction in the hydraulic fracturing processes. In this process, a hydraulic pressure forcibly fractures a porous material. In contrast to material fatigue, crack propagation in hydraulic fracturing is caused by a forced fracture once the pressure exceeds the material strength. The hydraulic pressure was applied through a moving interface that described the crack front. By coupling the XFEM simulation with a modellation of the fluid front retarding the hydraulic pressure, Wang was able to reproduce the lag in the hydraulic fracturing processes caused by the fluid's viscosity, [84].

2.3.2 Submerged Specimens

Fluid-Induced Crack Closure. A fluid-structure interaction inside Mode I cracks can provoke fluid-induced crack closure. In a dynamic setup, the flow resistance of the fluid prevents a fast evacuation of the crack and provokes crack closure. In a static load case, closing the crack mouth can prevent fluid from flowing out of the crack. In literature, the mechanism of fluid-induced crack closure is also denoted as oil trapping.

Davis and Ellison studied the hydrodynamic pressure on the crack faces in submerged specimens, [4]. Their experiments showed that the crack propagation rate in the submerged specimens was decreased compared to the reference group in air. They concluded that the fluid provoked premature crack closure, reducing the effective stress amplitude.

Similar conclusions were made by Polk et al. after investigating fatigue propagation rates of rotated beams in lubricated environments, showing lower crack propagation rates for specimens submerged in oil, [85]. However, their results remained inconclusive as the specimens in contact with distilled water had higher crack propagation rates than those without fluid contact. It remains unclear to what extent other factors influence the results. Lubrication of the crack faces or crack tip corrosion due to the applied water could have influenced the results.

Tzou et al. studied crack propagation in experiments with submerged specimens, [86], [87]. However, their results also remained inconclusive regarding

the influence of the fluid-structure interaction. They differentiated between low-stress and high-stress intensities, whether the load was in the range of the fatigue threshold and the critical stress intensity. For low-stress intensities, they reported increased propagation rates in submerged specimens. However, the difference between submerged specimens and the control group decreased with increasing viscosity. At high-stress intensities, the specimen submerged in the fluid had lower crack propagation rates than the control group. Their experiments could determine whether secondary effects like lubrication of the crack faces or mixed loadings significantly influenced the crack propagation rate at low-stress intensities. They proposed two competitive mechanisms to explain the different effects: suppression of corrosion fatigue and fluid-induced crack closure. The influence of the fluid-induced crack closure depended on the ability of the oil to penetrate the crack. They assumed that the fluid-induced crack closure is dominant at high-stress intensities, whereas the suppression of the corrosion fatigue process is more important at low-stress intensities.

Hydrostatic Pressure. David and Errision studied the influence of hydrostatic pressure on the fatigue crack propagation rate for submerged specimens. They concluded in their experiments that while hydrodynamic pressure leads to crack closure and reduced damage amplitudes, hydrostatic pressure provokes additional stress on the crack faces and, therefore, increases the stress amplitude. [3] The same conclusion was made in additional experiments by Plumbridge et al., [88].

2.3.3 Lubricated Contacts

In lubricated contacts, pressurized fluids are supposed to be essential for crack growth and the so-called rolling contact fatigue. Rolling contact fatigue occurs in rolling bearings, gear transmission, and railway wheels. Rolling contact fatigue occurs in two stages, [89]. In the first stage, shear-stress Mode II crack propagation is dominant, and the lubricant assists crack growth by reducing the friction between the crack faces. In the second stage, the fluid pressure on the crack faces leads to Mode I crack propagation. Figure 2.8 displays the four mechanisms attributed to fluid-assisted crack propagation in rolling contacts. Three out of the four mechanisms provoke a fluid pressure and Mode I crack growths. The motion of the contact pair can force fluid into the crack. The fluid inside the crack can be entrapped as the contact

force closes the crack mouth, and the motion of the crack faces can provoke a squeeze film pressure, [90].

Most studies focused on the influence of the fluid on fatigue crack propagation in driven-over rail systems, [90]–[94]. In [93], Bower remarked that fatigue cracks in railway tracks only propagate with a fluid present. Additionally, the cracks only propagate in the direction of the motion of the surface contact and if a traction force is applied. The traction force was assumed to open the crack for the fluid to enter before the surface contact forced the crack mouth to close. The surface contact acting on the rail pressurizes the trapped fluid, and the fluid pressure provokes a normal force on the crack faces, increasing the Mode I crack propagation rate, [91]. In [90], Fletcher et al. proved in full-scale track tests that fluid penetrated fatigue cracks in rolling surface contacts. The tests with marked water have shown that the fluid behavior is consistent with the assumed crack growth mechanism, increasing Mode I and Mode II crack growth.

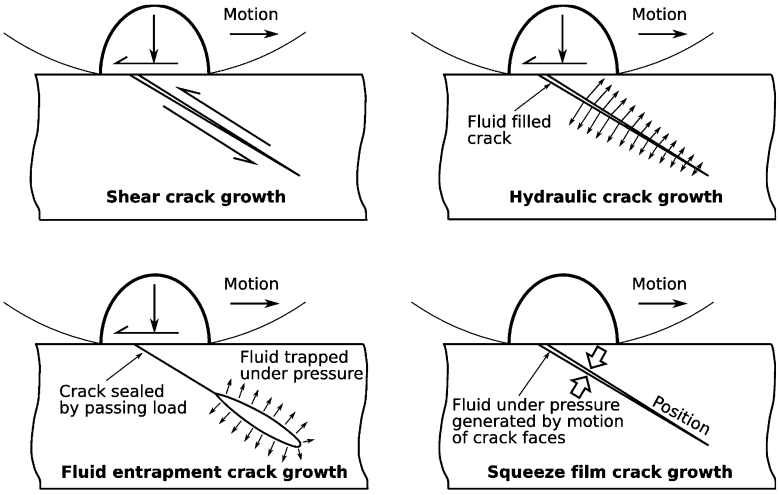

Figure 2.8: Opening of the crack due to the driving force on the left and trapped fluid provoking fluid-induced crack closure, [95].

The studies regarding rolling contact fatigue demonstrate that fluid-structure interaction does influence crack propagation, and fluid penetration of fatigue cracks occurs. The mixed loading of railways with dominant shear stress

differs from the internal pressure load of hydraulic components. Even though investigations of mixed Mode I and Mode II loadings in [96] have pointed out that the underlying stresses act independently, the mechanisms in rolling contact fatigue leading to fluid-structure interaction and Mode I crack growth are not identical to those present in hydraulic components. In contrast to hydrodynamic fluid-induced crack closure, the contact force closing the crack mouth traps the oil and provokes the hydrostatic pressure. It does not depend on the fluid's viscosity.

In conclusion, the contact force is the primary driver of mode I crack growth in the case of lubricated contact. Contrary to this, the fluid-structure interaction in hydraulic components is assumed to influence crack growth without additional external forces.

2.3.4 Fluid Flow Through Fatigue Cracks

As early as the 1990s, the first attempts to measure the leakage through fatigue cracks were made. The power industry aimed to detect leakage through cracks before the pipes and pressure vessels shattered.

In [97], Narabayashi et al. described experiments with bent pipes. The crack opening was varied by bending the pipe, and the water and steam volume flow was measured. The experiments indicated that the influence of surface roughness depended on the crack opening's size. The authors proposed a distinction between wide gaps and narrow gaps. The surface roughness had a minor influence in wide gaps, as the crack opening is significantly larger than the surface roughness. In narrow gaps, though, the surface roughness is in the magnitude of the crack opening, and its influence is more significant. Further measurements were carried out by Clarke et al. [98]. The results aligned with a laminar flow model between two plates for larger cracks. In the case of smaller crack openings, they assumed a crack flow aligned with the surface, following the «turns and bends» of the surface.

In [99], Bagshaw et al. carried out CFD simulations of idealized crack geometries in addition to experiments. The results indicated different flow regimes depending on the ratio of the crack opening and the surface roughness. The gas followed the surface curves for small crack openings. With larger openings, eddies form in the surface valleys, and the flow no longer follows the curvature of the rough surface. In [100], Chivers introduced friction factors as

a function of the Reynolds number of the flow and the surface roughness. In further investigations, Hong et al. demonstrated that leakage flow prediction is possible when considering the surface properties, [101].

For the correct description of the fluid-structure interaction in fatigue cracks of hydraulic components, the correct representation of the oil flow in the cracks is of particular importance. The previous studies indicate that the surface roughness must be considered when estimating the crack flow. However, a direct transfer of the measured volume flows to hydraulics is impossible as the studies focused on larger crack openings or gaseous fluids.

2.4 Research Approach

The state of research reveals two research gaps. On one side, the influence of a fluid-structure interaction inside the fatigue cracks of hydraulic components is yet to be confirmed. The existing studies regarding the fluid-structure interaction in high-cycle fatigue focused on lubricated contacts, railway contacts, or submerged specimens. In lubrication and railway contacts, an external compression force acts on the crack in contrast to the internal surface force provoked by the fluid pressure in hydraulic components. The submerged specimens were loaded with an external tensional force, and the fluid did not cause the principal load.

Furthermore, simulation-based approaches to complex fluid-structure interaction problems, e.g., with moving boundaries or inside fatigue cracks, exist in related fields. However, a simulation approach adapted to fatigue cracks in hydraulic components is still missing. Previous studies mainly focused on the simulation of crack propagation due to forced rupture by static hydraulic pressure. The influence of the temporal load pattern on the fluid-structure interaction in fatigue cracks has not yet been demonstrated. Neither has its impact on the stress amplitude for the transient loads typically encountered in hydraulics been quantified.

The presented work addresses these research gaps by providing a method for the simulation of fluid-structure interaction in narrow fatigue cracks. Existing research indicates that an oil flow into fatigue cracks is likely and that the interaction between the pressurized fluid and the crack faces influences the effective stress amplitude. The developed simulation approach aims

to provide a simple and performant tool for analyzing the fluid-structure interaction inside fatigue cracks of hydraulic components with transient loads. Subsequently, the underlying mechanisms and the parameters influencing the fatigue stress under transient hydraulic loads are discussed.

To summarize the research gaps, the following hypothesis is formulated:

«*The interaction between a pressurized fluid and crack face influences the effective stress amplitude of fatigue cracks in hydraulic components.*»

Five research questions were posed to answer the research hypothesis:

- *How does oil penetrate fatigue cracks in hydraulic components?*
- *How can the model complexity for FSI Simulations inside fatigue cracks be reduced?*
- *How does the interaction of the oil with the mechanic structure influence the stress amplitude of fatigue cracks?*
- *Which load and design parameters influence the effective stress amplitude of fatigue cracks under cyclic loads?*
- *Does the fluid-structure interaction inside fatigue cracks provoke a time delay between the pressure load and the mechanical deformation?*

These questions will be answered in the following work. The research approach builds on existing research from similar domains presented in Section 2.3 and combines the fundamental simulation techniques described in Section 2.2 to an adapted FSI simulation for fatigue cracks. The small dimensions of fatigue cracks prevent direct measurements of the fluid-structure interaction, but numerical simulations do not have these limitations. A two-way coupled simulation with a mechanic and fluid model is developed in the presented work to analyze the fluid-structure interaction inside fatigue cracks. The specific geometric and fluid-dynamic properties of the crack geometry and crack flow are exploited to develop the simulation models, and an indirect approach is employed to validate these. The simulated structural response to the fluid-structure interaction is compared to experimental results. The corresponding models are implemented and validated using a test specimen to demonstrate the simulation approach on an exemplary application. The studied influence of the fluid-structure interaction is generally valid for fatigue cracks of hydraulic systems, and the simulation approach can be transferred to other hydraulic components.

3 Investigated Geometry

This chapter describes the simulated planar geometry and the corresponding test specimens. The simulation approach is demonstrated for the test specimens with a geometry designed for the investigation of the fluid-structure interaction. There are many characteristic geometries in hydraulic systems, and deriving a representative geometry appears impractical. For this reason, the investigated geometry and the design of the test bodies were focused on the investigation of the fluid-structure interaction. Nevertheless, the demonstrated simulation approach is applicable to other geometries with Mode I fatigue cracks.
The chapter is divided into three parts. First, the requirements for the geometry are defined in accordance with the problem statement. Then, a two-dimensional geometry was derived and adapted to the requirements. The high-pressure connection typically found in hydraulic pumps and motors served as a model for the geometry. Subsequently, the three-dimensional test specimens were designed, and the expected service life was estimated.

3.1 Geometric Requirements

The geometry must fulfill several requirements to be suitable for the envisaged study. These are requirements required to provoke the investigated fatigue cracks. Additional requirements exist to enable a targeted analysis of the fluid-structure interaction, prevent undesired side effects, and keep the investigations within a manageable scope. When no macroscopic defects exist, crack initiation can take up to two-thirds of the lifetime, [12].

Fatigue cracks originate from local defects in the material. Surface flaws can be located at a surface, e.g., flaws caused by the manufacturing process or inside the material at grain boundaries or contaminants. For the fluid-structure interaction, however, only cracks exposed to the oil are relevant,

and the investigated cracks must originate from the internal surface of the geometry. Additionally, only Mode I cracks were considered as shear stress dominant cracks of Modes II and III do not have an opening cross-section, and a significant fluid flow into these cracks is unlikely.

Hence, the following main requirements have to be fulfilled by the geometry:

- Internal pressure chamber provoking a mechanical deformation of the geometry.
- Designated crack initiation point in contact with the pressurized fluid.
- Dominant Mode I crack propagation.

Furthermore, the following additional requirements were imposed:

- Dominant direction of the crack advancement to prevent varying crack paths.
- Fast initiation time and low structural resistance to reduce lifetime and experimental costs.
- Stable crack growth regime and no structural rupture to measure the influence of the fluid-induced crack closure and the fluid flow through the crack.
- Manufacturing of the part is possible with conventional manufacturing techniques.
- Transferability between a planar two-dimensional simulation and three-dimensional test specimens.

3.2 Planar Geometry

In [119], a planar geometry inspired by the pressure chamber of a hydraulic pump has been proposed. The proposed geometry shown in Figure 3.1 was characterized by a rectangular, rounded pressure chamber where the crack originates from the surface.

The resulting geometry is similar to hydraulic screw connections where cracks have been reported from industry, [120]. Rounded rectangular, circular, or

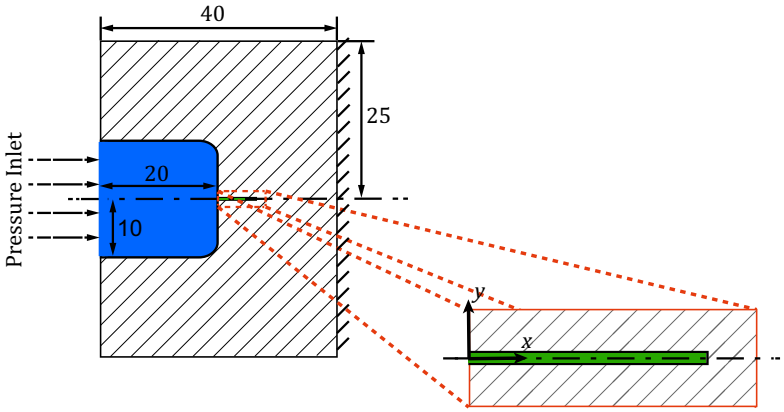

Figure 3.1: Geometry proposed by [119] with the fluid domains in blue (pressure chamber - dark blue, crack - green), the fixed support on the right and the pressure inlet on the left, [125]

.

elliptic shapes are commonly encountered in hydraulic components such as pressure chambers, valve housing, or connectors. An internal fluid pressure provokes a normal force, yielding suitable conditions for Mode I crack initiation and advancement. In conclusion, the proposed geometry is a suitable example for hydraulic components' internal Mode I fatigue cracks and was used successfully in [119] for FSI Simulations.

However, it does not fulfill all defined requirements. The pressure chamber is small compared to the wall thickness, resulting in insufficient stress levels for stable crack growth in the typical range of hydraulic test rigs of up to 400 *bar*. Additionally, the crack origin is not at the location of the highest local stress and is prone to a high variation.
The planar geometry displayed in Figure 3.2 has been developed by adapting this geometry to fulfill the defined requirements. The pressure chamber was prolonged, and a flange was integrated at the pressure inlet. The long pressure chamber limited the connector's undesired influence. For better manufacturing, the pressure chamber was constructed with two different diameters. A notch has been introduced to create a surface defect for crack initiation and reduce crack initiation time to a minimum. The supposed direction of the crack growth is displaced in green.
The fluid-structure interaction shall be analyzed in established cracks during

stable crack growth. The holes placed in the proximity of the notch modify the structural resistance to optimize the stress levels to attain stable crack growth at the desired pressure levels.

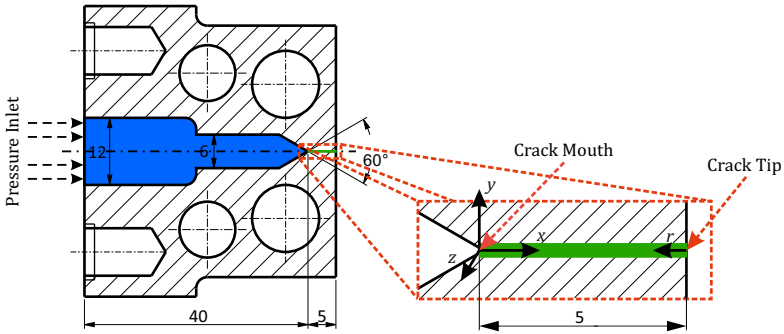

Figure 3.2: Derived planar geometry for the simulation of the FSI with the fluid domains in blue (dark blue: pressure chamber, light blue: supposed crack growth - green) and the pressure inlet with a flange at the left.

For the scope of this work, a specific coordinate system for positions inside the crack is defined. The origin of the coordinate system is fixed to the crack mouth, with the x-axis orientated in the direction of the crack propagation. The y-axis is perpendicular to the crack faces in the direction of the crack opening. The x- and y-axes span the plane of the two-dimensional crack geometry. The z-axis is oriented perpendicular to the x-y plane in the direction of the crack's width. The crack opening displacement (COD) denotes the displacement of the crack faces in the y-direction. The crack length denotes the length of the crack in the x-direction. Positions along the crack's length are given based on their distance from the crack mouth in x-coordinates. Positions along the x-axis in relation to the crack tip are defined by the crack tip radius r.

3.3 Test Specimens

Subsequently, the test specimen was constructed based on the planar geometry. The two-dimensional simulation assumes a plane-strain state. In theory, a plane-strain condition requires an infinite extent in one direction. In practice, an approximative plane-strain condition is reached when one

direction is one order of magnitude larger than the other directions. The expected crack opening displacement is in the range of micrometers. The design limits cracks' length to 5 *mm*, and the crack length is smaller during the crack propagation phase. Hence, plane-strain conditions at the center of the crack can be assumed if the component's depth is in the range of approx. 50 *mm*. The final notch was limited to 42 *mm* due to test and manufacturing constraints. Figure 3.3 depicts the constructed geometry.

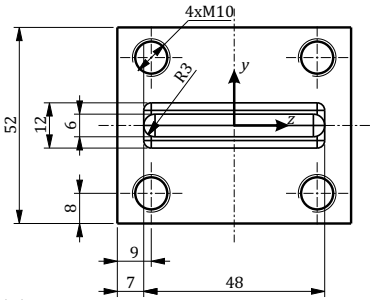

(a) Drawing of the tow view (pressure inlet) with dimensions in *mm*.

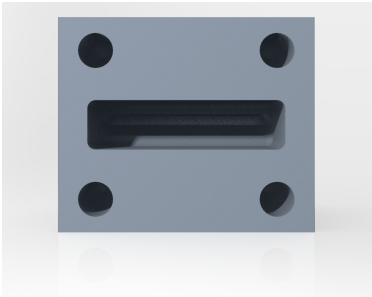

(b) Rendering of the specimen seen from the pressure inlet.

Figure 3.3: Test specimen design.

Preliminary crack growth calculations have been performed to choose an adapted material. The stress intensity factor in the notch was simulated, and the crack propagation rate was estimated. The choice of material has a significant influence on the crack propagation rate. Three different materials were compared: S235 structural steel, GJL 300 gray cast iron, and 26CrNiMo4 tempered steel. The approximated service life is given in Table 3.1.

Of the considered materials, only S235 steel has a service life between a hundred thousand and a million cycles. The stress intensity at the notch is above the critical value for GJL 300 gray cast iron. In 26CrNiMo4 tempered steel, stable crack growth should occur. However, the low number of cycles of about thirty thousand is at the lower limit of the high-cycle fatigue regime and can be critical regarding stable crack growth. Additionally, the low hardness of S235 compared to 26CrNiMo4 facilitates the manufacturing of the test benches. As a result, the test specimen has been manufactured from S235 steel.

In total, one test batch of 24 pieces was manufactured. All specimens were made from the same batch of material to minimize the variance due to different

Table 3.1: Approximative calculation of component service life (N) for S235, GJL 300 and 26CrNiMo4. Material parameters for Paris' Law from [12] with a stress ratio of $R_{SR} = 0.1$.

		S235	GJL 300	26CrNiMo4
ΔK_I	$MPa\sqrt{m}$	17	17	17
$\Delta K_{I,th}$	$MPa\sqrt{m}$	10.2	8.1	6.5
ΔK_{IC}	$MPa\sqrt{m}$	99	15.3	97.2
C_P	$m^{1+n/2}/MPa^n$	$1.2{\cdot}10^{-12}$	$3.50{\cdot}10^{-12}$	$2.51{\cdot}10^{-12}$
n_P	-	3.38	3.67	3.92
da/dN	$\mu m/1$	$1.80{\cdot}10^{-2}$	$1.15{\cdot}10^{-1}$	$1.67{\cdot}10^{-1}$
$CycleCount$	$1000x$	**277**	**43.5**	**29.9**
t at 3 Hz	h	25.7	4.04	2.77
Stable Crack Growth		Yes	No	Unclear

material treatments. The base materials were rectangular extruded profiles of S235 steel. The milling process consisted of two steps. The shape, interface, and inner pressure chamber were milled in the first manufacturing step. In the second step, the notch was manufactured with a sharp edge (6 *mm* diameter, 60° angle, 0.5 radius) to predefine the crack initiation.

4 FSI-Simulation

The fluid-structure interaction is supposed to provoke premature crack closure and limit the overall stress amplitude in cyclic loadings of hydraulic components. The simulation approach uses governing equations of the fluid and structural mechanics to approximate the fluid flow, the crack deformation, and the provoked fluid-structure interaction inside fatigue cracks.
In this section, the physical models are derived. In the first step, the finite-element analysis (FAE) of the test specimens with the commercial software Ansys Mechanical[1] is described. The finite-element analysis simulates the displacement of the crack, which is then approximated with the mechanic strip model. Additionally, the FAE simulations are used to estimate the crack length based on the measured deformation during the experiments.
The two-way coupling for the fluid-structure interaction simulation significantly increases the computing time as repeated iterations are required to reach a solution. The computational effort is even higher as the problem requires a small time advancement and high under-relaxation to assure numeric stability. In the case of the fluid-structure interaction inside fatigue cracks, this is inevitable because of the different spatial scales of the cracks' length and height. Reduced models are derived in the second part of the section to reduce the computational effort. The model complexities were reduced with the thin-film approximation of the fluid flow and the approximation of the displacement of the crack faces with weight functions.

[1] Ansys Mechanical is a commercial finite element solver by Ansys, Inc., [121]

4.1 Structural Simulation

The structural simulation of the test specimen has been implemented as a three-dimensional model with one symmetry plane. The model is solved based on the finite-element method described in Section 2.2.1.1. The development of the model has been separated into four parts. At first, the mesh of the solid domain is described, followed by the model parameter and the definition of the boundary conditions. Afterward, the evaluation of the finite-element analysis is described. The section concludes with a description of the SMART (Separating Morphing and Adaptive Remeshing Technology) tool of Ansys for preliminary simulations of the crack growth in the test specimens.
The mesh and the boundary conditions of the FEM model of the test specimen are visualized in Figure 4.1.

4.1.1 Mesh

Figure 4.1a depicts the FEM mesh. The mesh of the solid domain consisted of unstructured tetrahedral elements. The base element size of the elements was 1.8 *mm*. At the strain gauges' positions and inner surfaces, the mesh was refined by a factor of two. The crack plane was refined by a structured surface mesh with a characteristic element size of 120 μm. The tetrahedral elements used a quadratic basis function. The mesh consisted of 1.423 million elements with 2.098 million nodes.

4.1.2 Model Parametrization

The model parametrization is divided into the description of the boundary conditions, the material models, and the simulation parameters.

4.1.2.1 Boundary Conditions

Figure 4.1b visualizes the three types of applied boundary conditions. The specimen's model had support, surface force, and symmetry boundaries.

Supports. The model has two supports. The screwed joints are one support, and the surface contact with the adapter plate at the pressure inlet is the

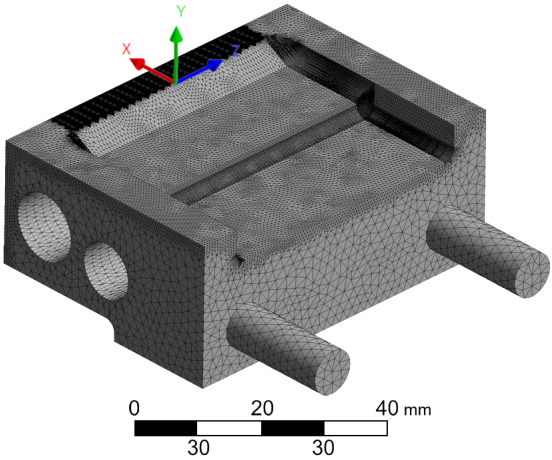

(a) Mesh of the solid domain for the finite-element method model with refinement around the crack, the inner surface, and the strain gauges' positions.

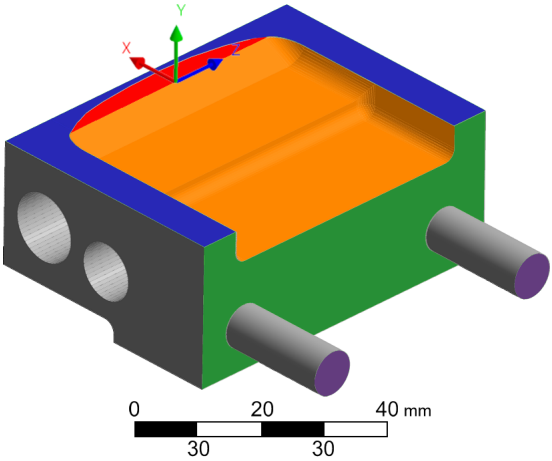

(b) Visualization of the solid domain with colorized areas of the boundary conditions. Blue: Y-Symmetry, Orange: Fluid Pressure, Red: Crack, Green: Frictionless Support in X-Direction, Purple: Fixed Support.

Figure 4.1: Simulation model used for the structural analysis with the finite-element method.

second one. Screwed joints are challenging to reproduce in a FEM model. Neither is the screwed connection a fixed support nor a cylindric sliding bearing. Modeling the threads as fixed supports has been proven to be too conservative compared to measurements, [128]. The best representation of the joints was achieved by including the screws as elastic parts fixed to the specimen with the screw heads modeled as fixed support. The contact with the fixation plate was defined as frictionless support normal to the contact plane. Due to its comparable high wall thickness, the fixation plate's deformation was negligible. Compared to the structural resistance of the specimen, the adhesive friction forces between the plate and the fixation plate were assumed to be negligible, especially as an elastic seal ring separated the surfaces.

Forces. The pressurized fluid inside the test specimens provoked a force on the internal surfaces. The surface force has been divided into an external pressure force, which took effect outside the crack in the pressure chamber, and an internal pressure force caused by the fluid inside the crack. The external fluid pressure has been applied uniformly on the surface of the pressure chamber. The external fluid pressure was identical to the applied load pressure.
For the simulation with a known internal pressure inside the crack, the pressure was applied uniformly along the y- and z-axis while varying along the x-axis. The internal pressure was applied as a surface force in intervals corresponding to the node positions of the mesh.

Symmetry. The last boundary condition is the symmetry condition. The test specimen is symmetric to the xz- and xy-plane. The crack plane is identical to the xz-plane, and the xz-symmetry condition was exploited to implement the advancement of the crack. Since the computation time of the non-coupled FEM simulation was not critical, exploitation of the XY symmetry was omitted to avoid an additional interface at the crack's centerline.

Crack advancement. The crack advancement was implemented by removing the symmetry conditions from the nodes corresponding to the crack. In the undamaged simulation, the symmetry condition was applied to all nodes, and as the crack advanced, the symmetry condition was removed from the nodes that were part of the crack. In Figure 4.1b, the symmetry condition (blue) is displayed for a crack with a characteristic crack length of 4.5 mm. The crack advancement is characterized by the crack's characteristic length being the crack's length at the specimen's center. Once the crack reaches the outer surface of the specimen, the characteristic length is prolonged for a virtual

crack (cf. Figure 4.3). The approximation of the crack front is based on the crack growth simulation with the SMART tool and the optical analysis of the cracked test specimens.

4.1.2.2 Material Models

The FAE used an isotropic linear elastic material with isotropic hardening. In the case of small deformations, an isotropic linear elastics model can be used for metals. Large deformations that exceed the yield strength of the material require a non-linear plastic material model to simulate the plastic deformations. Plastic materials can be modeled with an ideal plasticity or by various non-linear hardening laws, e.g., the isotropic hardening law.

Linear Elastic Material. The linear elastic material model is based on Hook's law. The principal stresses are linearly proportional to the strain, [102],

$$\epsilon_1 = \frac{\sigma}{E},\ \epsilon_2 = -\nu\frac{\sigma}{E} \tag{4.1}$$

with E being the materials Young's modulus. The linear elastic material stretched in one direction compressed in perpendicular directions. The ratio between the stretching in one direction and the compression in the other direction is given as the Poisson coefficient ν. The generalized three-dimensional Hook's law is given in [102]. Due to the linearity, all acting forces can be treated separately, and the provoked strain can be aggregated. This property is exploited by the mechanic strip model in the subsequent Section 4.2.2.

Isotropic Hardening. One possibility to represent plastic deformation and hardening is the isotropic hardening model. Figure 4.2 depicts the linear elastic strain followed by an ideal plasticity or an isotropic hardening. In contrast to ideal plasticity, the hardening model assumes that the material strength increases during the plastic deformation. The isotropic hardening approximates the material hardening above the yield strength by a linear function with a constant tangential module. The material model is denoted as bilinear as a linear isotropic hardening follows the linear elastic yield. In contrast to kinematic hardening, isotropic hardening does not account for the hysteresis due to the Bauschinger effect. However, the hysteresis should be negligible, as no compressive force is applied in alternation with the tensile pressure load.

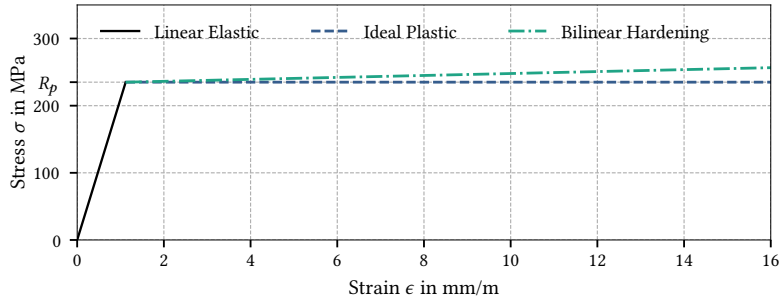

Figure 4.2: Strain / stress diagram with ideal plastic or bilinear hardening. Yield strength: $\sigma_Y = 235\ MPa$, tangent modulus: $1,450\ MPa$

Material Properties. The simulation used an isotropic linear elastic material model for all elastic simulations and a bilinear isotropic hardening model for the plastic simulations. The material constants, displayed in Table 4.1, corresponded to structural-grade carbon steel S235 that are provided in the 1998er ASME BPV Code, Section 8, Div 2, Table 5-110.1, [103]. The deformation of the material has been assumed as isothermal, and the thermal properties of the material have been neglected.

Table 4.1: Material constants for S235, [103]

Constant	Value	Unit
Density (ρ)	7,850	kg/m^3
Young's Modulus (E)	210	GPa
Poisson's Ratio (ν)	0.3	-
Yield Strength (σ_Y)	235	MPa
Tangent Modulus	1,450	MPa

4.1.2.3 Simulation Parameters

The solver of Ansys Mechanical features a variety of parameters to change the solution properties and improve the convergence of the solution. The analysis was performed as a transient structural analysis in both the static and the

dynamic simulations. The simulation was performed without time integration to neglect the body inertia. Without time integration, each timestep is solved individually. The simulations have been performed with a constant time advancement with a value of $\Delta t = 2 \cdot 10^{-4}\ s$. Rayleigh-Damping was included with a beta damping coefficient to improve the convergence of the model. The force and displacement residuals verified the convergence of the model. Table 4.2 gives an overview of the solver parameters.

Table 4.2: FEM solver parameters

Parameter	Value	Description
Time Advancement	$2 \cdot 10^{-4}\ s$	-
Simulation Type	Transient Structural	-
Time Integration	Off	Include Transient Effects
Solver Type	PCG Solver	Sparse or Iterative PCG
Weak Springs	Off	Additional Weak Springs
Large Deflections	Off	-
Newton-Raphson Option	Full	Stiffness Matrix Update
Convergence Criterions	Force & Displacement	-
Convergence Value	Program Controlled	-
Energy Dissipation Ratio	$1.0 \cdot 10^{-4}$	Rate of the Damping
Beta Coefficient	0.287	Stiffness Damping
Unit System	μmks	μm, kg, mN, s

4.1.3 Evaluation

The simulation results were processed with the Ansys Parametric Design Language (APDL), a structured scripting language providing low-level access to the simulation results. The implemented scripts calculated two high-level results: the measured strain at the strain gauges' positions and the displacement of the crack faces.

Strain Gauges. The strain gauges were simulated as linear elements fixed to the surface nodes on the designated positions. The strain measured by the gauges was equal to the average strain of the surface elements in the area of the gauges' grid.

Crack Opening Displacement. The crack nodes' displacement was evaluated at the center line of the crack. The displacement of the elements along the line was equal to one-half of the total COD.

4.1.4 SMART Simulation

Preliminary simulations of the crack advancement were conducted with the SMART (Separating Morphing and Adaptive Remeshing Technology) function of Ansys Mechanical, [121]. The SMART function provides an engineering tool for numerically simulating the crack advancement in a conform finite-element mesh. The crack advancement is calculated stepwise either by the Paris' Law or, in the case of a forced rupture, by a maximal stress condition. The simulation results offered a preliminary approximation of the propagating crack front in the test specimen. In these simulations, the Paris Law' with the material constants given in Table 3.1 was implemented. Figure 4.3 depicts the derived crack fronts at different characteristic crack lengths. The simulation used simplified boundary conditions without fluid-structure interaction inside the cracked regions. Hence, the static pressure on the crack faces and fluid-induced crack closure were neglected. A constant surface force in the pressure chamber substituted the fluid pressure.

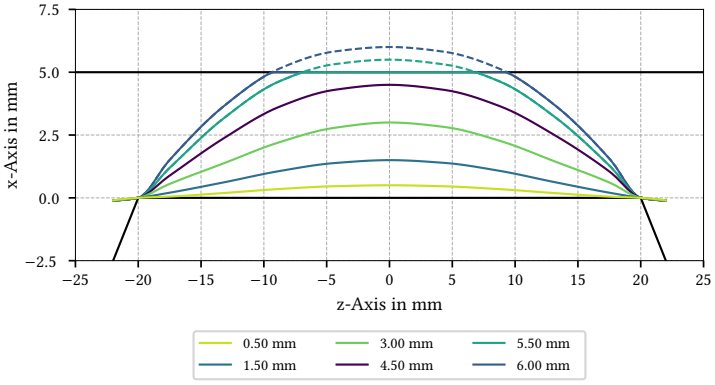

Figure 4.3: Approximated propagation of the crack front in the test specimen (legend: Characteristic crack length in *mm*).

4.2 Reduced-Order Models

The finite-element method and finite-volume method provide a high degree of flexibility. Nevertheless, this flexibility comes with high computational costs. Simulation of the fluid-structure interaction inside fatigue cracks is challenging due to the different scales and low damping. The height of the cross-sections inside fatigue cracks ranges between five and sixty micrometers, whereas the length and width can be up to three orders of magnitudes larger. Reducing the load pressure and the mechanic structure's elastic relaxation takes milliseconds, while the oil flow inside the fatigue cracks takes seconds. The oil's low compressibility combined with a minimal cross-section provides only marginal damping compared to the high structural resistance. In addition, the crack geometry is subject to severe change throughout a pressure pulse. As the crack closes, the COD decreases to zero, and dynamic re-meshing is necessary.
Small element sizes and time steps, in combination with a strong under-relaxation and dynamic re-meshing, are possibilities to overcome these limitations. However, they come with significant computational costs. The fluid-structure interaction requires many iterations to converge. In combination with high under-relaxation and small timesteps, the number of iterations quickly becomes unfeasible. However, exploiting the specific physical and geometric properties of fatigue cracks and the fluid flow makes it possible to reduce the models' complexity. The length-to-height ratio allows for a thin-film modelation of the flow instead of a three-dimensional finite-volume analysis. Weight functions correlating the internal load to the structural deformation can approximate the COD. In the following sections, the reduced-order models are derived.

The presented simulation approach has four steps, displayed in Figure 4.4. The input consists of the studied geometry, the material, and the applied load pressure. In the pre-processing step, the weight functions for the crack deformation are derived, e.g., by a finite-element analysis, and the flow regime must be parameterized. The weight functions, the flow factors, and the load pressure are inputs to the coupled FSI simulation. The FSI simulation calculates the pressure field, the fluid flow, and the crack face displacement. In the post-processing, the part's complete mechanical deformation is simulated by the three-dimensional FAE to evaluate the virtual strain gauges.

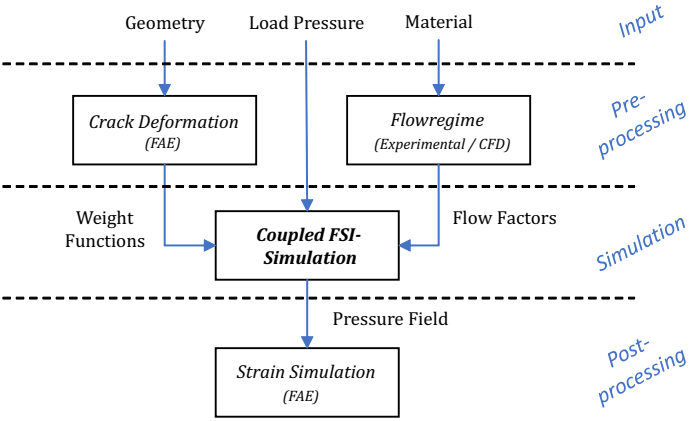

Figure 4.4: Overview of the workflow of the simulation approach.

4.2.1 Laminar Flow Model

The laminar flow model simulates the oil flow inside fatigue cracks under the assumption of a thin film with a laminar Poiseuille flow profile. Reducing the flow model to a two-dimensional laminar Poiseuille flow reduces the model complexity significantly compared to the complexity of a three-dimensional finite-volume analysis.
The flow area inside the crack can be characterized by the crack's length l_0, the crack's width b, and the crack's height h (crack opening displacement). As the crack's width in the z-direction was considerably larger (about one order of magnitude) than its length, the z-direction has been neglected by the assumption of a planar two-dimensional flow. Typically, crack opening displacements are in the range of micrometers ($h < 50\ \mu m$), in contrast to the studied crack's lengths of $l_0 \in (1, 5)\ mm$ and the crack width of $b \approx 40\ mm$.

The following assumption has been made for the reduced fluid model:

- The fluid flow is isothermal.
- The viscosity is constant.

- The pressure is constant over the crack's height (thin-film approximation).
- The body forces are negligible (e.g., gravity, magnetic fields).
- The no-slip boundary conditions hold.
- The fluid compressibility does not influence the flow profile.

The fluid's gravity and inertia have been neglected. Neglecting the fluid inertia results in the assumption of a fully developed flow, which is not the case as the pressure pulsations are highly transient and non-stationary. However, the inertial forces remained negligible compared to the viscous forces, which will be discussed further in Section 4.2.1.1. The fluid compressibility is partially neglected following the Boussinesq approximation [64]. The Boussinesq approximation assumes that the difference in the fluid's inertia due to the compressibility is negligible, but the compressibility is sufficiently strong to alter the fluid mass. Hence, fluid compressibility is considered in the conservation of mass but neglected in the Navier-stokes equations in the derivation of the flow profile. In the following, the analytic solution of the Poiseuille flow profile over the crack's height is combined with a finite-difference simulation of the flow in the direction of the crack.

4.2.1.1 Crack geometry

In the laminar flow model, the crack of the length l_0 is divided into N strips with index n, as shown in Figure 4.5. The stripes are uniformly distributed with length Δx being,

$$\Delta x = \frac{l_0}{N}. \tag{4.2}$$

The flow variables are defined for the center of each stripe: the volume of the stripe V_n, the pressure p_n, the density ρ_n, and the flow velocity u_n in the x-direction. The volume flow per unit length from the strip $n-1$ to the strip n is denoted as q_n.

The thin-film theory is applicable only when the height of the fluid cross-section is small compared to the other dimensions. The order of magnitude of the different lengths can be estimated by normalizing the variables of the governing equation and replacing the dimensional parameters by characterizing boundaries. In the following paragraph, an extract of the complete derivation

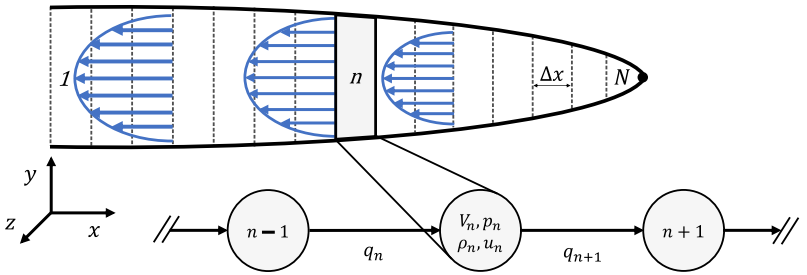

Figure 4.5: Representation of the crack geometry with fluid stripes and laminar flow profile.

of the normalized flow variables from [63] is given for the dimensions of the crack. At first, the coordinates are replaced by nondimensional coordinates x^*, y^*, z^* defined as

$$(x^*, y^*, z^*) = \frac{1}{L_{xz}} \left(x, \frac{1}{\zeta} y, z \right). \tag{4.3}$$

The typical length L_{xz} and the aspect ratio ζ are defined such that $(x^*, y^*, z^*) \in [0, 1]$. The normalized velocities follow from the equation of continuity as

$$(u_x^*, u_y^*, u_z^*) = \frac{1}{\Psi} \left(u_x, \frac{1}{\zeta} u_y, z_x \right) \tag{4.4}$$

with the characterizing velocity along the crack Ψ.

The pressure error Δp_e of the thin-film approximation was estimated in [63] as a function of the aspect ratio ζ. The aspect ratio ζ depends on the dimensions of the film's cross-section. For ratios of $\zeta \leq 0.05$, the pressure error was $\Delta p_e \leq 1\%$, for larger ratios of $0.05 < \zeta \leq 0.1$ the pressure error increased quite rapidly up to $\Delta p_e \leq 16\%$.

Several assumptions about the film dimensions were made to estimate ζ and whether the thin-film approximation is applicable. An established crack has a minimal length of $L_{xz} \geq 1.0\ mm$, whereas the maximal cross-section was $L_y \leq 50\ \mu m$. In consequence, the aspect ratio is

$$\zeta \leq \frac{50\ \mu m}{1.0\ mm} = 0.05 \tag{4.5}$$

and the approximative pressure error of the thin film theory is $\Delta p_e \leq 1\%$. However, the error significantly increases for cracks smaller than 1 mm. For $L_{xz} \leq 0.5\ mm$ the aspect ratio follows as

$$\zeta \geq \frac{50\ \mu m}{0.5\ mm} = 0.1 \tag{4.6}$$

and $\Delta p_e \gtrsim 16\%$. Nevertheless, these boundaries are highly conservative for short cracks, as shorter cracks also have a smaller cross-section.

The ratio of the maximal crack opening displacement $\max(h_0)$ and the minimal crack length $\min(l_0)$ gives the maximum of the average crack slope. The maximal local slope is estimated by twice the average slope, which is

$$\frac{\partial h}{\partial x} < 2 \cdot \frac{\max(h_0)}{\min(l_0)} \approx 2 \cdot \frac{0.05}{1} = 0.1. \tag{4.7}$$

Hence, the slope remains under the threshold of $1 : 10$, which is in the tolerance of the thin-film theory, [63],

Additionally, a reduced Reynolds number and a reduced frequency are defined to assess the influence of fluid inertia. Given the density ρ and the dynamic viscosity η of the fluid and the characteristic length L_y of the cross-section (which is equal to the crack opening displacement $h(x,t)$), the Reynolds number Re and the reduced Reynolds number Re_ζ are, [63],

$$Re = \frac{\rho \Psi L_y}{\eta}, \quad Re_\zeta = \zeta Re. \tag{4.8}$$

The non dimensional time t^* is defined as $t^* = \Omega t$ with the characteristic frequency Ω being approximately $\Omega \approx \Psi / L_{xz}$, [63]. By substitution into the Navier-Stokes equation and neglection of higher order terms, the reduced frequency Ω^* follows as, [63],

$$\Omega^* = \Omega \cdot L_y^2 \frac{\rho}{\eta}. \tag{4.9}$$

The influence of the inertia effects remains small for values of $\Omega^* \leq 1$ and $Re_\zeta \leq 1$

The minimal duration of the pressure drop is $t \geq \frac{400\ bar}{400\ kbar/s} = 1\ ms$ and the average velocity $\bar{u}_x$ for a crack with maximal length $l_0 \leq 5\ mm$ is given as

$$\bar{u}_x \leq \frac{5\ mm}{1\ ms} = 5 m/s. \tag{4.10}$$

The characteristic velocity Ψ was assumed to be twice the average value as $\Psi \leq 2\bar{u}_x = 10\ m/s$. The reduced Reynolds number and the reduced frequency follow as

$$\begin{aligned} Re_\zeta &\leq 0.05 \frac{844\ kg/m^3 \cdot 50\ \mu m \cdot 10 m/s}{0.0388\ Pas} = 0.544 \leq 1 \\ \Omega^* &\leq 10,000 \cdot (50\ \mu m)^2 \frac{844\ kg/m^3}{0.0388\ Pas} = 0.544 \leq 1 \end{aligned} \tag{4.11}$$

The reduced Reynolds number and the reduced frequency remained smaller than one, concluding that the fluid inertia has only a minor influence, [104].

4.2.1.2 Averaged Volume Flow

In consequence of the thin-film approximation and the neglection of the inertia, the Navier-Stokes equations are simplified following the derivation of the Reynolds equation, as shown in Section 2.2.2.1, to

$$\frac{\partial p}{\partial x} = \eta \frac{\partial^2 u_x}{\partial y^2} \tag{4.12}$$

and

$$\frac{\partial p}{\partial z} = \eta \frac{\partial^2 u_z}{\partial y^2}. \tag{4.13}$$

Equation (4.13) equals zero because of the assumption of a plane flow in x and y. Integrating (4.12) twice with respect to y and the boundary conditions

$$\begin{aligned} u_x(y = 0) &= 0 \\ u_x(y = h) &= 0 \end{aligned} \tag{4.14}$$

results in

$$u_x(y) = \frac{1}{2\eta}(y^2 - yh)\frac{\partial p}{\partial x}, \tag{4.15}$$

which is known as the flow profile of a plane Poiseuille flow between two long parallel plates. The volume flow per unit length q follows from the volume flow Q as

$$q = \frac{Q}{b} = \int_0^h u_x(y) dy = \bar{u}_x \cdot h \tag{4.16}$$

with the average velocity $\bar{u}_x$ and the crack width b. Integrating equation (4.15) over $y \in [0, h]$ leads the volume flow per unit length along the x-direction

$$q = -\frac{h^3}{12\eta}\frac{\partial p}{\partial x}. \tag{4.17}$$

The original Reynolds equation does not take into account the surface roughness. If the surface roughness is in the range of the film thickness, it reduces the volume flown, [105]. Due to turns and bends during the crack propagation, the crack surfaces are not necessarily smooth. Therefore, following the averaged flow model described in Section 2.2.2.3, a flow factor $\theta \in [0, 1]$ has been included in the flow model to account for the surfaces' shape. The corrected volume flow per unit length is

$$\boxed{\tilde{q} = -\theta\frac{h^3}{12\eta}\frac{\partial p}{\partial x}.} \tag{4.18}$$

The surface roughness of fatigue cracks is analyzed in Section 5.1.3, and the flow factors are parametrized by volume flow measurements in Section 5.3.

4.2.1.3 Mass Conservation

A second equation is given by the conservation of mass (see Section 2.2.2.1),

$$\frac{\partial \rho}{\partial t} + \frac{\partial(\rho u_x)}{\partial x} + \frac{\partial(\rho u_y)}{\partial y} + \frac{\partial(\rho u_z)}{\partial z} = 0. \tag{4.19}$$

Given the mentioned assumptions, as $u_y = 0$ and $u_z = 0$, the conservation law simplifes for a one-dimensional flow to

$$\frac{\partial \rho}{\partial t} + \frac{\partial(\rho u_x)}{\partial x} = 0. \tag{4.20}$$

In contrast to most formulations of the conservation law, where the control volumes are assumed to be constant, in our case, the crack's height varies in space and time due to the crack's opening and closing. As a result, the integral of equation (4.20) with respect to y in the bounds $y \in [0, h(t)]$ is

$$\frac{\partial \rho}{\partial t}h + \frac{\partial h}{\partial t}\rho + \frac{\partial(\rho \bar{u}_x)}{\partial x}h + \frac{\partial h}{\partial x}(\rho u_x(h)) = 0, \tag{4.21}$$

with the Leibniz integral rule and substitution of

$$\int_0^h u_x(y)dy = \bar{u}_x \cdot h \tag{4.22}$$

from equation (4.16). The no-slip condition at the surfaces defines $u_x(0) = u_x(h) = 0$. The pressure and the density are assumed to be constant over the crack's height.

Equation (4.21) can be rearranged and divided by h to get

$$\frac{\partial \rho}{\partial t} = -\frac{\partial(\rho \bar{u}_x)}{\partial x} - \frac{\partial h}{\partial t}\frac{\rho}{h}. \tag{4.23}$$

The compression of the oil is assumed to be isothermal with bulk modulus K and a reference density of ρ_0 at atmospheric pressure,

$$\rho(p) = \rho_0 \left(1 + \frac{p}{K}\right). \tag{4.24}$$

The partial derivative of equation (4.24) with respect to t is

$$\frac{\partial \rho(p)}{\partial t} = \frac{\rho_0}{K}\frac{\partial p}{\partial t}. \tag{4.25}$$

Inserting equation (4.23) into (4.25) and rearranging leads to

$$\frac{\partial p}{\partial t} = -\left(\frac{\partial(\rho \bar{u}_x)}{\partial x} + \frac{\partial h}{\partial t}\frac{\rho}{h}\right)\frac{K}{\rho_0}, \tag{4.26}$$

which defines the evolution of the pressure over time.

Substitution of the average velocity $\bar{u}_x$ in equation (4.26) by q/h (equation (4.16)), and replacing the volume flow per unit length q with the corrected volume flow per unit length $\tilde{q}$ leads to

$$\boxed{\frac{\partial p}{\partial t} = -\left(\frac{\partial(\rho \tilde{q})}{\partial x} + \rho\frac{\partial h}{\partial t}\right)\frac{K}{\rho_0 h}.} \tag{4.27}$$

4.2.1.4 Discretization

Equation (4.18) and equation (4.27) define the flow variables of the laminar model as differential equations of space (∂x) and time (∂t). In the next step, $\frac{\partial(.)}{\partial x}$ and $\frac{\partial(.)}{\partial t}$ are replaced by discrect differences. The flow stripes are indexed by n in contrast to the timesteps indexed by k. The spatial and temporal indices of the spatial step size $\Delta x_{k,n}$ and temporal Δt_k step size are omitted for the sake of clarity. The spatial step size can vary over time and space, e.g., when modifying the mesh after a timestep or when refining the mesh in certain areas of interest. The temporal step size can vary only over time. Hence, the finite differences are

$$\begin{aligned}
\frac{\partial p}{\partial t} &= \frac{p_{k+1} - p_k}{\Delta t}, \\
\frac{\partial p}{\partial x} &= \frac{p_{n+1} - p_n}{\Delta x}, \\
\frac{\partial(\rho\tilde{q})}{\partial x} &= \frac{(\rho\tilde{q})_{n+1} - (\rho\tilde{q})_n}{\Delta x}, \\
\frac{\partial h}{\partial t} &= \frac{h_k - h_{k-1}}{\Delta t}.
\end{aligned} \tag{4.28}$$

The derivates of the pressure p and the mass flow $(\rho\tilde{q})$ are discretized by forward difference schemes. In contrast to those, the derivate of the crack's height h is replaced by a backward difference scheme. The mechanic strip model to calculate h is discussed in the next section. However, as the structural inertia is neglected, h_k only depends on p_k and not on h_{k-1}. Hence, using the backward difference, the two-way coupled model of the fluid-structure interaction can be formulated as a forward Euler simulation. Inserting the finite differences, equation (4.28) into the fluid equations (4.27) and (4.18) gives

$$\boxed{\tilde{q}_{k,n} = -\theta \frac{h_{k,n}^3}{12\eta} \frac{p_{k,n+1} - p_{k,n}}{\Delta x}} \tag{4.29}$$

and

$$\frac{p_{k+1,n} - p_{k,n}}{\Delta t} = \left(-\frac{(\rho\tilde{q})_{k,n+1} - (\rho\tilde{q})_{k,n}}{\Delta x} - \rho_0 \frac{h_{k,n} - h_{k-1,n}}{\Delta t} \right) \frac{K}{\rho_0 h_{k,n}} \tag{4.30}$$

with the unkown p_{k+1}. Rearranging equation (4.30) results in the final forward Euler formulation of the laminar flow model

$$\boxed{p_{k+1,n} = \left(-\frac{(\rho\tilde{q})_{k,n+1} - (\rho\tilde{q})_{k,n}}{\Delta x} - \rho_0 \frac{h_{k,n} - h_{k-1,n}}{\Delta t} \right) \frac{K}{\rho_0 h_{k,n}} \Delta t + p_{k,n}.} \quad (4.31)$$

4.2.1.5 Boundary Conditions

Three boundary conditions have to be met in the model:

- The pressure at the crack opening ($n = 0$) is equal to the system load pressure.
$$p_{k+1,0} = p_0(t_k)$$
- The mass flow at the crack tip ($n = N$) is zero.
$$\tilde{q}_{k,N} = 0$$
- Initially ($t = 0$), the pressure inside the crack of the simulation equals zero.
$$p_{0,n} = 0$$

Given these boundary conditions, $p_{k+1,n}$ can be solved for all $k \in (0, \infty)$ given the yet unknown variable $h_{k,n}(p_{k,n})$.

4.2.2 Mechanic Strip Model

The displacement of the crack faces interacts with the fluid flow inside the crack. The fluid pressure inside the pressure chamber and the crack caused the structural deformation of the crack and the crack opening displacement. Under the assumption of a linear elastic material, the total deformation is expressed as the superposition of the deformation caused by a subpart of the total force. The pressure force is divided into $N+1$ subparts. One subpart is for the external displacement of the pressure chamber, and N subparts for each section (stripe) of the crack. Figure 4.6 visualizes the N crack stripes, with an individual pressure force for each of the N stripes. The external forces, in this case the load pressure inside the pressure chamber, are modeled as far-field

force F_{ex}. The pressure inside the crack is modeled as a piecewise uniform distributed surface force acting on the stripes. The stripes corresponded to the spatial nodes of the laminar flow model.

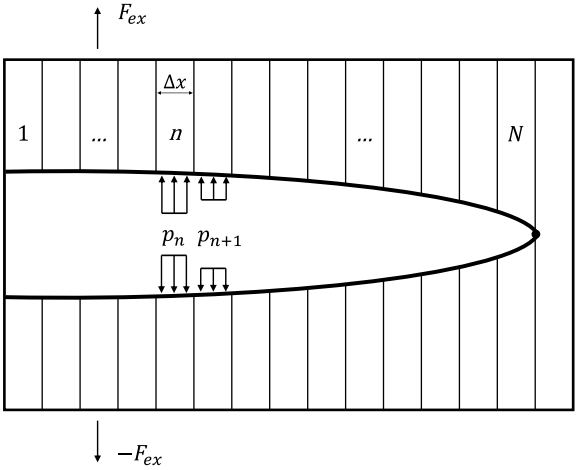

Figure 4.6: Yield strips with elementwise constant pressure force and external far-field force.

The center of the strip with index n is located at $x = \xi_n$ with the size Δx_n. The fluid pressure at the strip n is accounted for by a uniformly distributed pressure load p_n. For clarity, the time index t is omitted in the following section.

4.2.2.1 Weight Functions

The total crack opening displacement of the stripes is given by the superposition of the far field forces F_{ex} and the internal forces $p_n = p(x = \xi_n)$ as

$$h(x) = \frac{1}{E}\left[F_{ex}w^{ex}(x) + \sum_{n=1}^{N}(p_n w^n(x, \xi_n)\Delta x)\right] \tag{4.32}$$

with the corresponding weight functions w^{ex} and $w^n(x)$. The weight functions[2] approximate the unknown displacement field of the corresponding

[2] In literature, weight functions are also denoted as influence functions.

loads, [106]. A similar approach is found in various implementations of the yield strip model, [107]. In the case where the only external force is a fluid pressure p_0 applied to a constant surface area A_0, equation (4.32) can be simplified by replacing $F_{ex} = p_0 \cdot A_0$ and $w^{ex} = \frac{\Delta x}{A_0} w^0$ and including both in the summation.

$$h(x) = \frac{1}{E} \left[\sum_{n=0}^{N} (p_n w^n(x, \xi_n) \Delta x) \right] \tag{4.33}$$

The spatial distribution of the deformation caused by the external pressure is represented by the weight function $w^{ex}(x)$. The external pressure is a far-field force, and $\xi_0 = 1$ is required in the matrix formulation for compatibility with the internal pressure force but has no physical significance. The weight functions describe the spatial distribution of the crack opening displacement caused by the pressure forces. They depend exclusively on the geometry and are independent of the applied loads. Analytic solutions of the weight functions can be found in the literature for some particular cases, e.g., in infinite elastic plates, [56], [108], [109].

The analytic solution of the weight function for a concentrated force P applied at ξ_n on a symmetric crack of length l_0 in an infinite elastic plate is given in [108] as

$$\tilde{w}(x) = \frac{2}{\pi} log \left| \frac{\sqrt{l_0^2 - \xi_n^2} + \sqrt{l_0^2 - x^2}}{\sqrt{l_0^2 - \xi_n^2} - \sqrt{l_0^2 - x^2}} \right|, \ |x| \leq l_0, \ \xi_n \leq l_0, \ |x| \neq \xi_n, \tag{4.34}$$

and

$$h(x) = \frac{P}{E} \tilde{w}(x), \ |x| \leq l_0. \tag{4.35}$$

Without restricting the geometry to these cases, approximations of the influence functions are required. Fett et al. proposed in [110] polynomial regressions as weight functions. In the following, polynomial regressions are implemented to approximate the spatial displacement field of the pressure forces. A polynomial regression of the weight function $w^n(x, \xi_n)$ with respect to $x - \xi_n$ is given as

$$w^n(x, \xi_n) = \sum_{i=0}^{\infty} C_{i,n} (x - \xi_n)^i \tag{4.36}$$

with coefficients $C_{i,n}$ which results in a polynomial regression model. The coefficients were determined based on a known displacement, e.g., through

a numeric simulation (finite-element analysis) or an analytic solution. A polynomial least-square regression can determine the, in a least-square sense, best-fitting coefficients. For the stripe $n = \iota$ the polynomial regression model of order $\Pi \leq N$ at the discrete positions x_n, $n \in [1, N]$ is

$$w^{\iota}\left(\begin{bmatrix} x_1 \\ x_2 \\ \vdots \\ x_N \end{bmatrix}, \xi_{\iota}\right) = \begin{bmatrix} 1 & (x_1 - \xi_{\iota}) & (x_1 - \xi_{\iota})^2 & \dots & (x_1 - \xi_{\iota})^{\Pi} \\ 1 & (x_2 - \xi_{\iota}) & (x_2 - \xi_{\iota})^2 & \dots & (x_2 - \xi_{\iota})^{\Pi} \\ \vdots & \vdots & \ddots & \vdots & \\ 1 & (x_N - \xi_{\iota}) & (x_N - \xi_{\iota})^2 & \dots & (x_N - \xi_{\iota})^{\Pi} \end{bmatrix} \begin{bmatrix} C_{0,\iota} \\ C_{1,\iota} \\ \vdots \\ C_{\Pi,\iota} \end{bmatrix} \tag{4.37}$$

and in matrix notation

$$\vec{w}^{\iota} = \mathbf{X}\vec{C}_{\iota}. \tag{4.38}$$

If $h^{\iota}(\vec{x})$ is the crack opening displacement for the case

$$p_n = 0, \ \forall \ n \in [1, N] \setminus \iota \tag{4.39}$$

then

$$\vec{w}^{\iota} = \frac{E}{p_{\iota}\Delta x} h^{\iota}(\vec{x}). \tag{4.40}$$

The coefficients of the polynomial regression were then estimated using the ordinary least square equation

$$\vec{C}_{\iota} = \left(\mathbf{X}^T\mathbf{X}\right)^{-1}\mathbf{X}^T\vec{w}^{\iota}. \tag{4.41}$$

When comparing the polynomial regressions with the analytic solution of equation (4.34) in Figure 4.7, it can be seen that a polynomial regression of an order of thirty-four or lower is not able to approximate the weight function close to the applied force. However, using even higher-order polynomials produces numerical errors and decreases overall stability.

For the fluid-structure interaction in hydraulic components, an accurate representation of the strain caused by the internal pressure forces inside the crack is crucial. Therefore, neither the analytic approximation for an infinite elastic plate, neglecting the geometry, nor the single polynomial regressions leading to significant errors are applicable. In order to improve the approximation, a piecewise-defined weight function for the left and the right parts of the crack has been implemented with different polynomial coefficients. The polynomial regression of the left side is $w^{n,l}$ with coefficients $C^{l}_{i,n}$ and

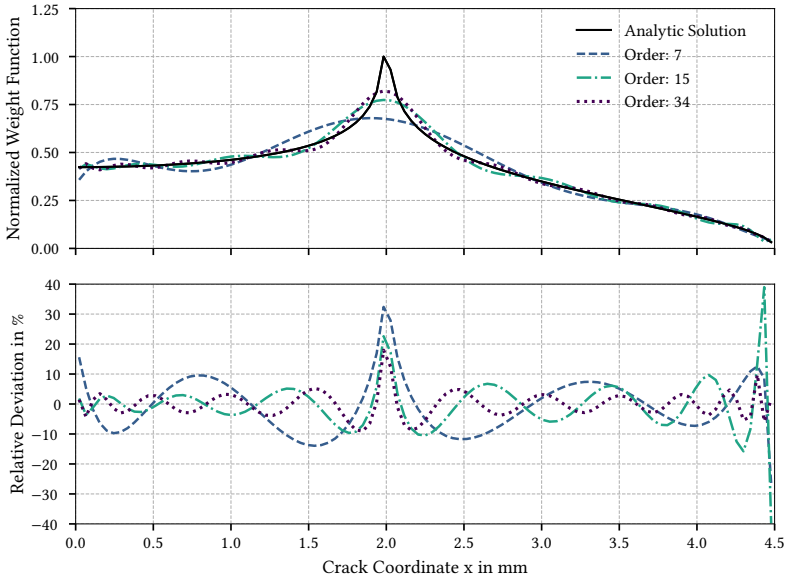

Figure 4.7: Analytic solution of the weight function for infinite elastic plates and polynomial regressions of various orders for a pressure strip at $\xi_l = 2.0\ mm$.

the regression of the right side is $w^{n,r}$ with the corresponding coefficients $C^r_{i,n}$. Combining both gives the weight function as

$$w^n(x,\xi_n) = \begin{cases} w^{n,l} = \sum_{i=0}^{\infty} C^l_{i,n}(x-\xi_n)^i, & x < \xi_n \\ w^{n,r} = \sum_{i=0}^{\infty} C^r_{i,n}(x-\xi_n)^i, & x \geq \xi_n \end{cases}. \tag{4.42}$$

The piecewise polynomial regression resulted in higher approximation accuracy even with lower-order polynomials, which additionally increased the numeric stability. The coefficients of the left and right polynomials have been determined separately by equation (4.41). The crack opening displacement for the corresponding partial pressure load of the crack faces has been determined by the finite-element method simulation described in Section 4.1. In the following implementation, polynomials of seventh order have been used except for the borders, where lower-order polynomials are needed. The number of nodes restricts the order of the polynomials. The order has to be equal to or smaller than the number of remaining nodes left of the base node

$n = \iota$. The same applies to the right polynomial. The number of nodes has to be equal to or higher than the order of the polynomial.

$$\begin{aligned} \Pi_l &\leq \iota \\ \Pi_r &\leq (N - \iota) \end{aligned} \tag{4.43}$$

In Figure 4.8, the piecewise polynomial approximation, the solution of the analytic weight function, and the simulated deformation are shown for the studied geometry with a crack length of $l_0 = 4.5\ mm$ at the section $\xi_\iota = 2.0\ mm$. After the determination of the coefficients of the weight function, the crack opening displacement is calculated with respect to $p(x)$ by equation (4.33). In the following, the crack opening displacement is evaluated at the same positions as the fluid pressure, setting $x_n = \xi_n$. In consequence, using equation (4.33) and combining all nodes into one matrix, the crack opening displacement is calculated in dependence of the pressure as

$$\begin{bmatrix} h(\xi_1) \\ h(\xi_2) \\ \vdots \\ h(\xi_N) \end{bmatrix} = \begin{bmatrix} w^0(\xi_1, \xi_0) & w^1(\xi_1, \xi_1) & \dots & w^N(\xi_1, \xi_N) \\ w^0(\xi_2, \xi_0) & w^1(\xi_2, \xi_1) & \dots & w^N(\xi_2, \xi_N) \\ \vdots & \vdots & \ddots & \vdots \\ w^0(\xi_N, \xi_0) & w^1(\xi_N, \xi_1) & \dots & w^N(\xi_N, \xi_N) \end{bmatrix} \begin{bmatrix} p_0 \\ p_1 \\ \vdots \\ p_N \end{bmatrix} \tag{4.44}$$

or in matrix notation as

$$h(\vec{x} = \vec{\xi}) = \mathbf{W}\vec{p} \tag{4.45}$$

with the weight matrix

$$\mathbf{W} = \begin{bmatrix} \vec{w}^0 & \vec{w}^1 & \dots & \vec{w}^N \end{bmatrix} = \begin{bmatrix} w^0(\xi_1, \xi_0) & \dots & w^N(\xi_1, \xi_N) \\ \vdots & \ddots & \vdots \\ w^0(\xi_N, \xi_0) & \dots & w^N(\xi_N, \xi_N) \end{bmatrix}. \tag{4.46}$$

and $\vec{\xi}$ defined as

$$\vec{\xi} = \{\xi_n\}, \forall\ n \in [0, N]. \tag{4.47}$$

In the weight matrix given in equation (4.46), the entries are either from the left polynomial of the weight function or from the right polynomial. In the simulation, the same node position for the pressure and the displacement has been used ($x_n = \xi_n$), and, hence, the conditions from equation (4.42) become $\xi_\iota < \xi_n$ for the left polynomial and $\xi_\iota \geq \xi_n$ for the right polynomial. In consequence, all entries of and above the main diagonal are of the left

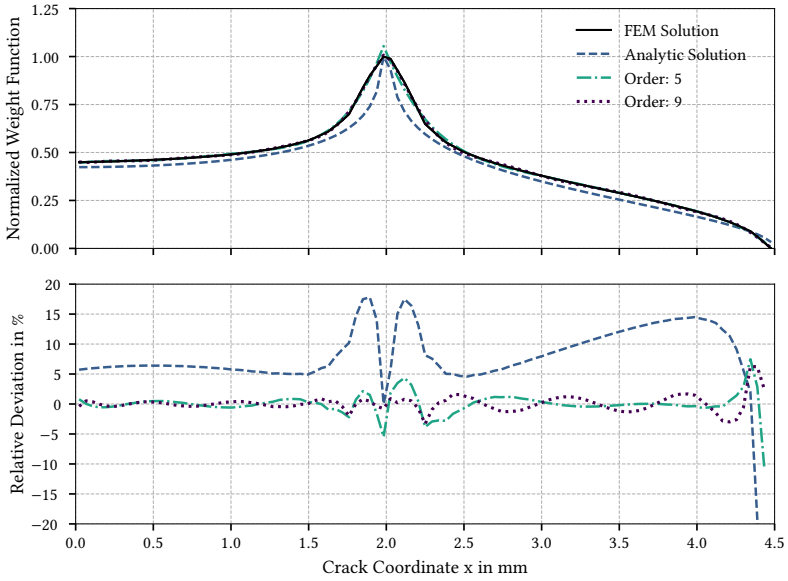

Figure 4.8: FEM Solution of the weight function and piecewise polynomial regressions of various order for a pressure strip at $\xi_\iota = 2.0\ mm$.

polynomial, while all elements below the main diagonal are of the right polynomial. The external pressure force has only one (right) approximation.

$$\mathbf{W} = \begin{bmatrix} w^{0,r}(\xi_1, \xi_0) & w^{1,l}(\xi_1, \xi_1) & \dots & w^{N,l}(\xi_1, \xi_N) \\ w^{0,r}(\xi_2, \xi_0) & w^{1,r}(\xi_2, \xi_1) & \dots & w^{N,l}(\xi_2, \xi_N) \\ w^{0,r}(\xi_3, \xi_0) & w^{1,r}(\xi_3, \xi_1) & \dots & w^{N,l}(\xi_3, \xi_N) \\ \vdots & \vdots & \ddots & \vdots \\ w^{0,r}(\xi_{N-1}, \xi_0) & w^{1,r}(\xi_{N-1}, \xi_1) & \dots & w^{N,l}(\xi_{N-1}, \xi_N) \\ w^{0,r}(\xi_N, \xi_0) & w^{1,r}(\xi_N, \xi_1) & \dots & w^{N,l}(\xi_N, \xi_N) \end{bmatrix} \tag{4.48}$$

The weight matrix $\mathbf{W}$ depends exclusively on the geometry and is independent of the applied load. The part's geometry is inherited by the polynomial coefficients and represented in the weight matrix with respect to the fluid and the structural mesh. Both meshes consist of N nodes at the center of the corresponding stripes. The node positions ξ_n were constant throughout the simulation as no re-meshing was implemented. Hence, the weight matrix

W is constant and was calculated prior to the simulation to increase the performance of the simulation.

The required weight functions have been approximated from the part's deformation simulated by the finite-element method model described in Section 4.1. The FAEs used to determine the weight functions have been purely elastic, neglecting plastic deformations at the crack tip. Weight functions for five crack lengths $l_0 \in \{0.5, 1.5, 2.5, 3.5, 4.5\}$ mm have been approximated.

4.2.2.2 Plastic material deformation

The linear superposition of the forces is only valid in the linear elastic case. The linear elastic stress field of the crack results in a stress singularity at the crack tip, as shown in Figure 2.2. In reality, however, there is plastic deformation of the material around the crack tip. Irwin's model described in Subsection 2.1.1.4 provides an estimate of the plastic zone.
In the implemented strip model, the size of the plastic zone is estimated using Irwin's model based on the calculated linear elastic displacement. Subsequently, the crack is prolonged by the size of the plastic zone, and the displacement of the virtual crack is calculated. The virtual crack is shifted compared to the linear elastic by the plastic zone size a' (see Figure 2.2). As the size of the plastic zone is small compared to the crack's length, the shape of the virtual crack is assumed to be identical to the shape of the original crack. The plastic deformation of the yield strip at the crack tip is defined by the crack opening displacement of the shifted crack at the original crack tip. The plastic deformation is then superposed with the linear elastic deformation.

The size of the plastic zone a_{pl} is given by Irwin's model for the plane-strain conditions as, [28],

$$a_{pl} = \frac{(1-2\nu)^2}{2\pi} \cdot \frac{K_I}{\sigma_Y}^2 \tag{4.49}$$

with the material's yield strength σ_Y, the linear elastic stress intensity factor K_I and the Poisson's ratio ν.

From the size of the plastic zone a_{pl} follows the plastic deformation at the crack tip as

$$\hat{h}_{pl} = h(l_0 - a_{pl}), \quad \text{if } h(l_0 - a_{pl}) > \hat{h}_{pl}. \tag{4.50}$$

The plastic deformation was treated like an additional force at the crack tip's strip. However, the once-generated plastic deformation was not reversed

during the simulation. The influence of the plastic deformation on the other stripes uses the same weight function

$$h_{pl}(\vec{x}) = \frac{\vec{w}^N}{max(\vec{w}^N)} \cdot \hat{h}_{pl}, \tag{4.51}$$

which was used for the fluid pressure. The approximation of the plastic zone and the plastic deformation has limitations. In Figure 4.9, the crack opening displacement simulated by a finite-element analysis with isotropic plastic hardening is compared to the approximation of the mechanic strip model. The three-dimensional specimen was charged inside the crack with the pressure simulated by the developed FSI simulation. Besides minor differences due to the discretization of both models, the deviation in the simulated total displacement between the two simulations was negligible. However, two main limitations of the approximation with Irwin's model were observed.

Irwin's model assumes that the stress field expands till infinity. In the case of a crack length of 4.5 *mm*, the distance between the parts' surface and the crack tip was small, and the surface restricts the expansion of the stress field. Hence, the local stress distribution differed from the theoretical model, and the approximation underestimates the plastic deformation.

The second limitation was observed at the time of the minimal crack opening displacement. The finite-element analysis showed a slight decrease in the deformation at the crack tip, while the plastic deformation of the mechanic strip model was constant. Irwin's model estimates the primary plastic zone. However, the closing crack faces provoke compressive stress at the crack tip, leading to inversed plastic deformation, the cyclic plastic zone, [24]. The implemented yield strip model did not incorporate backward plasticity. Despite this simplification, the reduced-order model deviates only slightly, as the proportion of backward plasticity was small compared to the total plastic deformation.

4.2.2.3 Effective Stress Amplitude

The stress intensity factors express the stress amplitude in linear elastic fracture mechanics. In the proposed approach, the stress intensity factors were approximated based on the movement of the crack faces, as neither the J-integral nor the crack tip stress can be calculated from the weight

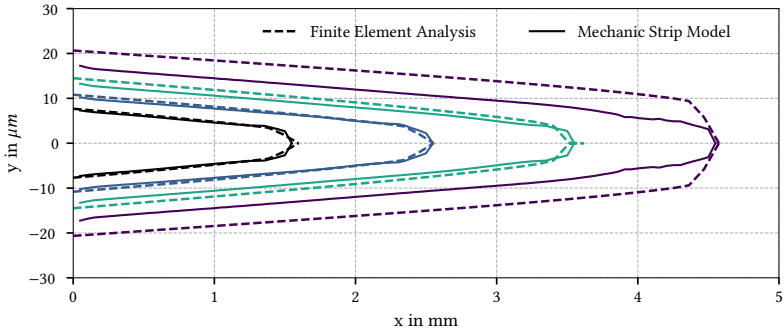

(a) Time of the maximal crack opening displacement.

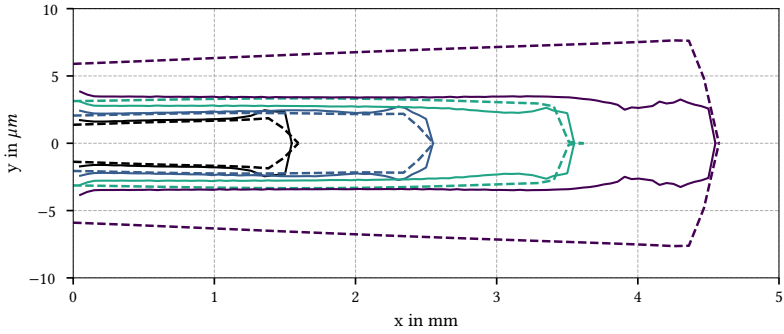

(b) Time of the minimal crack opening displacement.

Figure 4.9: Simulated crack opening displacement at different crack lengths (black: 1.5 *mm*, purple: 2.5 *mm*, blue: 3.5 *mm*, green: 4.5 *mm*) of the finite-element analysis with a bilinear plastic material (dashed) and the mechanic yield strip model (solid).

functions of the strip model. The difference between the minimal and maximal stress intensity throughout one cycle defines the effective stress amplitude, determining the crack propagation rate. The stress intensity factor is given at each timestep based on the simulated crack opening displacement $v_y(r)$ by

$$K_I = \lim_{r \to 0} \frac{E}{(\kappa + 1)(1 + \nu)} \cdot \sqrt{\frac{2\pi}{r}} \cdot v_y(r). \tag{4.52}$$

The crack tip radius is defined as $r = l_0 - x$ and plane strain conditions are assumed, $\kappa = \frac{(3-\nu)}{1+\nu}$. However, close to $r \approx 0$, the numeric solution is poor

due to the discretization error of the simulation, and a low accuracy would be achieved. Instead, the stress-intensity factor (SIF) was approximated over several elements in the range of $r \in [0.5, 1]$ to achieve a higher accuracy (cf. Figure 4.10).

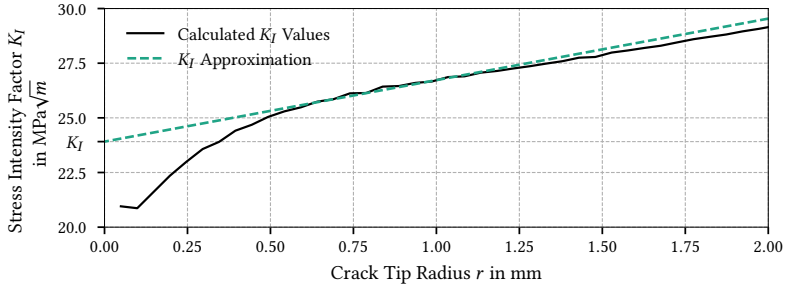

Figure 4.10: Theoretic calculated SIF and SIF approximation in the vicinity of the crack tip.

Given the crack opening displacement

$$h(x_i, t) = \frac{1}{2} h_i(t), \quad \forall\, 0 \leq x_i < l_0 \tag{4.53}$$

and $x(r) = l_0 - r$, the approximated stress intensity function $\tilde{K_I}(r)$ is

$$\tilde{K_I}(r) = \frac{E}{(4-\nu)} \cdot \sqrt{\frac{2\pi}{r}} \cdot h(l_0 - r). \tag{4.54}$$

The linear regression of the numeric stress intensity factors is $f(r) = m \cdot r + K_I$, with the intercept being the approximate stress intensity factor K_I. The least-squares solution defines the optimal linear regression as

$$\begin{bmatrix} K_I \\ m \end{bmatrix} = \left(\mathbf{R}^T \mathbf{R}\right)^{-1} \mathbf{R}^T \mathbf{K_I}, \tag{4.55}$$

with

$$\mathbf{R} = \begin{bmatrix} 1 \cdots 1 \\ r_1 \cdots r_i \end{bmatrix}^{-1} \tag{4.56}$$

and

$$\mathbf{K_I} = \begin{bmatrix} 1 \cdots 1 \\ r_1 \cdots r_i \end{bmatrix}^{-1} \begin{bmatrix} \tilde{K_I}(r_1) \\ \vdots \\ \tilde{K_I}(r_i) \end{bmatrix} \tag{4.57}$$

for $r_i \in [0.5, 1]$ mm. For each time step t_i, the stress intensity factor was approximated, and the effective stress amplitude was calculated as the difference between the lowest and highest stress intensities,

$$\Delta K_I = K_{I,max} - K_{I,min}. \tag{4.58}$$

Various crack propagation laws exist to estimate the resulting crack advancement per cycle da/dN based on the amplitude of the stress intensity factors. Among them are the Paris' Law and the NASGRO-Equation. For the estimates of the damage provoked by the varying stress amplitudes, the NASGRO-Equation was used as it takes into account different stress ratios. The NASGRO-Equation is given as

$$\frac{da}{dN} = C_{FM} \cdot \left[\left(\frac{1-\gamma}{1-R_{SR}}\right) \cdot \Delta K_I\right]^{n_{FM}} \cdot \frac{\left(1 - \frac{\Delta K_{I,th}}{\Delta K_I}\right)^{p_{FM}}}{\left(1 - \frac{K_{I,max}}{K_{IC}}\right)^{q_{FM}}} \tag{4.59}$$

with material constants C_{FM}, n_{FM}, $\Delta K_{1,th}$, K_{IC}, p_{FM}, and q_{FM}. The function $\gamma(R_{SR})$ depends on the stress ratio R_{SR} and is calculated as

$$\gamma = \max\left(R_{SR}, A_0 + A_1 R_{SR} + A_2 R_{SR}^2 + A_3 R_{SR}^3\right) \tag{4.60}$$

with coefficients

$$\begin{aligned}
A_0 &= \left(0.825 - 0.34\alpha_{FM} + 0.05\alpha_{FM}^2\right) \cdot \cos\left(\frac{\pi}{2} S_R\right)^{1/\alpha_{FM}}, \\
A_1 &= \left(0.415 - 0.071 \cdot \alpha_{FM}\right) \cdot S_R, \\
A_2 &= 1 - A_0 - A_1 - A_3, \\
A_3 &= 2A_0 + A_1 - 1,
\end{aligned}$$

which depend on the material constants α_{FM} and S_R.

4.2.2.4 Mass Inertia

The mechanic strip model neglects the mass inertia. An upper bound for the mass inertia experienced by the crack faces can be derived from Newton's second law. For the crack faces, Newton's second law can be formulated as

$$\frac{\partial \sigma(\vec{x}, \vec{y})}{\partial y} = \rho \frac{\partial^2 v_y(\vec{x}, \vec{y})}{\partial t^2}. \tag{4.61}$$

As the integral of equation (4.61) with respect to y is unknown, the effect of the inertia can be assessed by introducing the crack face motion as an upper bound

$$\frac{\partial^2 h(\vec{x})}{\partial t^2} > \frac{\partial^2 v_y(\vec{x},\vec{y})}{\partial t^2}. \tag{4.62}$$

Inserting equation (4.62) into equation (4.61) and integration with respect to $y \in [0, L_y]$ gives

$$\sigma(\vec{x}) < \rho L_y \frac{\partial^2 h(\vec{x})}{2\partial t^2} \tag{4.63}$$

with the characteristic length L_y. Introducing the normalized variables

$$\frac{\partial h^*}{\partial t} = \frac{1}{H}\frac{\partial h}{\partial t}, \quad t^* = \frac{t}{\Gamma}, \quad \rho^* = \frac{\rho}{\rho} = 1 \tag{4.64}$$

with the characteristic values H, Γ. The normalized inertial force is defined as

$$\sigma^*(\vec{x}) = \frac{2\Gamma^2}{\rho H L_y}\sigma(\vec{x}). \tag{4.65}$$

The ratio between the inertial and the pressure force is given as

$$\zeta = \frac{1}{p^*(\vec{x})} = \frac{\rho H L_y}{\Gamma^2 P} \tag{4.66}$$

with characteristic pressure P.
The characteristic time is $\Gamma = 1\ ms$. The crack opening displacement is twice the distance moved by each crack face. Assuming a crack opening displacement of $2H = 50\ \mu m$ and a characteristic wall thickness in y-direction of $L_y = 25\ mm$, the aspect ratio is

$$\zeta = \frac{1}{p^*(\vec{x})} = \frac{844\ kg/m^3 \cdot (25\ \mu m) \cdot (25\ mm)}{(1\ ms)^2 \cdot (400\ bar)} = 1.32 \cdot 10^{-5}. \tag{4.67}$$

The ratio ζ suggests that the inertial forces are up to a magnitude of 10^5 smaller than the pressure forces.

4.2.3 Two-Way Coupling

In a two-way coupled fluid-structure interaction simulation, the pressure force is transferred to the mechanical domain, and the mechanical displacement is

transferred to the fluid domain. The coupling can be formulated implicitly, solved by iterating to a steady state, or explicitly. In this case, we used forward and backward difference schemes for a forward Euler formulation of the simulation. Given the fluid pressure at the current timestep k, the crack opening displacement is given by equation (4.45). In a subsequent step, the pressure at the following timestep $k + 1$ is determined by equation (4.31). Figure 4.11 depicts the calculation steps of the developed simulation method. The green frame depicts the mechanical domain, and the blue frame depicts the fluid domain.

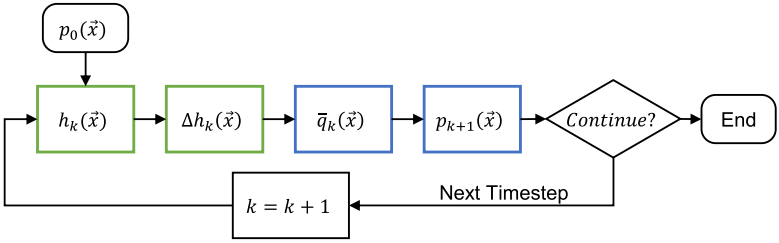

Figure 4.11: Calculation steps of the two-way coupled reduced simulation method (green frame: mechanic domain, blue frame: fluid domain, black frame: other execution steps).

4.2.3.1 Under-Relaxtation

The numeric stability of this fluid-structure interaction simulation is challenging as minor numerical errors in the crack opening displacement provoke significant pressure changes due to the small volume and oil's low compressibility. These significant pressure changes provoke a displacement of the crack faces, resulting in changing fluid pressure. Hence, the system is prone to high oscillations. Additionally, as the body inertia is neglected, it does not dampen these oscillations. An under-relaxation was applied to increase numeric stability in order to avoid these oscillations. An under-relaxation factor of λ was implemented into the coupled simulation. The crack opening displacement $h_k(\vec{x})$ (equation (4.31)), is replaced by an under-relaxed term $\hat{h_k}(\vec{x})$ as

$$\hat{h}_{k+1}(\vec{x}) = \hat{h}_k(\vec{x}) + \lambda \left[h_{k+1}(\vec{x}) - \hat{h}_k(\vec{x}) \right]. \tag{4.68}$$

The under-relaxation corresponds to a low-pass filter where the under-relaxation factor is

$$\lambda = \frac{\Delta t}{\tau_{lp}} \tag{4.69}$$

with time advancement Δt and time constant τ_{lp}. To assure the simulation accuracy, the filter's time constant τ_{lp} has to be significantly smaller than the frequency of the expected deformations.

4.2.3.2 Simulation Parameters

The forward Euler method requires a small-time advancement to attain the intended accuracy and be numerically stable. The Courant-Friedrichs-Lewy condition provides a necessary condition for the numeric stability of explicit time integration schemes, [60]. The condition states that the timestep must be smaller than the time that any object needs to travel from one to the next grid point. In other words, the numeric information transport domain has to include the physical transport domain.

The Courant-Friedrichs-Lewy condition is defined as:

$$\Psi \cdot \frac{\Delta t}{\Delta x} = CFL \leq 1 \tag{4.70}$$

In the simulations, the section size was $\Delta x = 50\ \mu m$, and the maximal fluid velocity was $\Psi = 10\ m/s$. Hence, the maximal timestep is given as

$$\Delta t \leq \frac{1}{10\ m/s} \cdot 50\ \mu m = 5 \cdot 10^{-6}\ s \tag{4.71}$$

However, due to the challenging numeric stability, an even smaller time advancement of up to $\Delta t = 2 \cdot 10^{-8}\ s$ has been used. Leading to a total step count of $1.6710 \cdot 10^7$ steps for a single 3 Hz pulse. The time constant of the low-pass filter was chosen as $\tau_{lp} = 2 \cdot 10^{-6}\ s$ resulting in an under-relaxation factor of $\lambda = 0.01$. A complete list of all parameters, separated into material properties, simulation parameters, and material constants of the NASGRO equation, are in the Appendix in Table A.1, Table A.2, and Table A.3, respectively.

4.2.4 Convergence Study

The section length was chosen based on a convergence study performed for crack lengths of $l_0 = 2.5\ mm$ and $l_0 = 4.5\ mm$. In both cases, the maximal mass flow and the total surface force of the oil were evaluated at the time of the highest pressure drop. The section length was varied in the interval $\Delta x \in [30, 600]\ \mu m$. Figure 4.12 depicts the results of the convergence study. The true value of the variables is unknown, and the simulation error can not be calculated directly. However, the discretization error decreases to zero for infinitesimal small section lengths. Consequently, the variables are supposed to converge the true value for small section lengths.

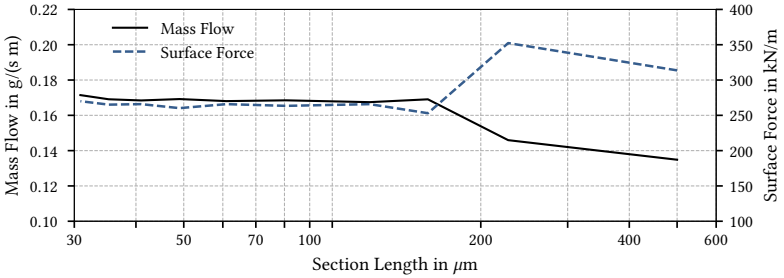

(a) Crack size of $l_0 = 2.5\ mm$.

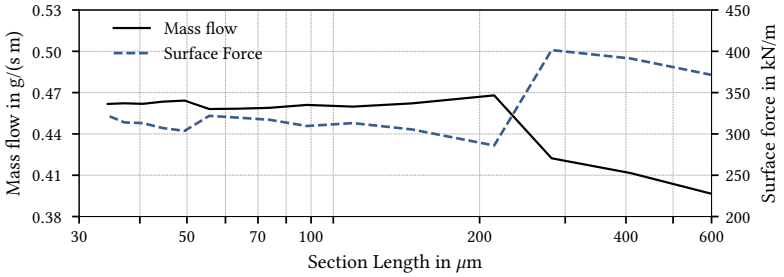

(b) Crack size of $l_0 = 4.5\ mm$

Figure 4.12: Maximal mass flow and total surface force at the time of the highest pressure drop.

The results indicate that a section length of $\Delta x < 100\ \mu m$ is sufficiently small to minimize the simulation error due to the discretization. On the other

hand, the numeric errors increased for further decreasing crack size, and the simulation was no longer numerically stable for section lengths below $\Delta x < 30\ \mu m$. Hence, a section length of $\Delta x = 50\ \mu m$ was chosen. The section length of $\Delta x = 50\ \mu m$ was used for all crack lengths as the results indicated that it is sufficiently small, even for short cracks.

5 Experiments

The following fatigue experiments validate the developed reduced-order models. The deformation of the specimens was measured during the fatigue experiments. The specimens's deformation made it possible to deduce the crack growth and the amount of oil in the crack. The flow rates through the crack were measured once the crack reached the surface and the specimens leaked.
At least two specimens of different runs were inspected at each validation step. More specimens were tested when the results of the two specimens did not align or when the validation step was prone to high variance. However, most figures depict the result of only one specimen to improve clarity. The results of the other specimens are visualized in additional figures in the Appendix.
The Section is divided into four parts. In the first part, the fatigue experiments on the pulsation test rig are described. The second and third parts present the strain measurements and the test setup for the mass flow measurements. The Section concludes with the validation of the simulation.

5.1 Fatigue Experiment

The test specimens were tested in four runs on a hydraulic pulsation test rig with pulse frequencies of 3 Hz and 6 Hz and drop rates of 10 $kbar/s$ and 80 $kbar/s$. The volume flow through the specimens was measured after the fatigue experiments, and the specimens underwent destructive component testing for an optic analysis of the crack front and the crack's surface.

5.1.1 Experimental Setup

Figure 5.1 shows the hydraulic schematics of the test rig where the auxiliary components are omitted. The pulse is generated by a rectangular pulse

generator driven by a motor with adjustable speed. Two adjustable throttle valves in the pump and the tank line of the pulse generator controlled the pressure build-up and drop rate. Pressure gauges measured the pressure at the output of the pulse generator and after the connector block. The shape of the pulse generator was constant, switching between the pump line and the tank line mechanically. Therefore, the maximal charge- and discharge time are limited to one-half of the pulse duration, respectively.

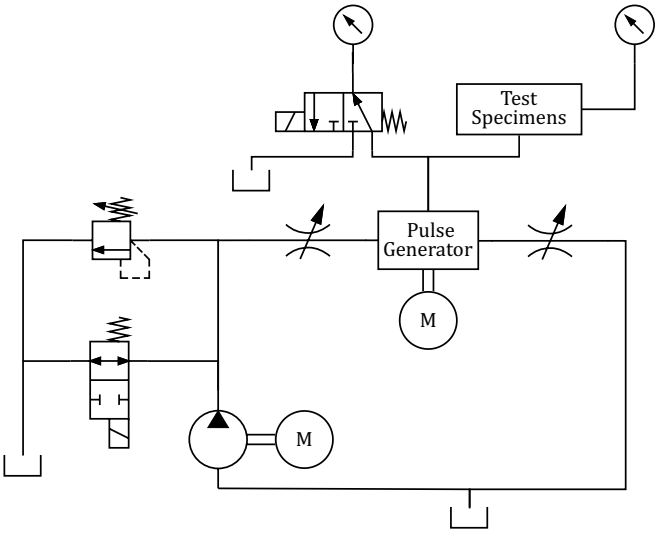

Figure 5.1: Hydraulic schematics of the pulsation test rig, [127].

The adjustable throttle valves controlled the flow resistance in the pump and tank-line of the pulse generator. However, the cross-section of the flow lines limited the minimal flow resistance and the maximal temporal pressure gradients.

The test specimens were connected to the hydraulic circuit by a G1/2" thread. A large cross-section of the connection is required to minimize the pressure losses in the inflow and outflow and achieve high temporal pressure gradients (drop rates). The stiffness of the test assembly determines the amount of oil flow and limits the temporal pressure gradients. All hydraulic connections have been made with steel fittings and steel pipes. The G1/2" thread could not be integrated into the test specimens due to the manufacturing process of

the notch, and an adapter plate was required. Each test specimen was fixed with four M10 screws to an adapter plate with a G1/2" thread. The complete assembly is displayed in Figure 5.2. Four specimens have been tested with the same configuration for statistical analysis of the experiments. The test assembly included a rotationally symmetric connector block that provided mounting points for up to four test specimens. Symmetry was required to guarantee equal pressure distribution and gradients for all four specimens.

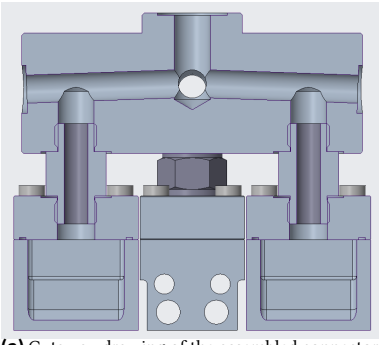

(a) Cutaway drawing of the assembled connector block with four test specimens.

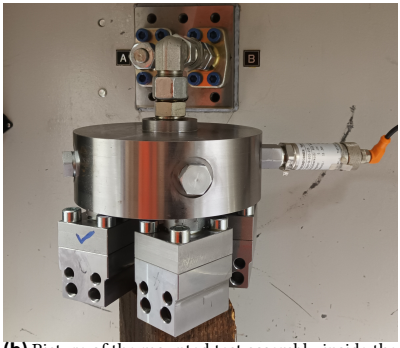

(b) Picture of the mounted test assembly inside the test chamber of the hydraulic test rig.

Figure 5.2: Flow divider and picture of the mounted test assembly.

The volume flow during one pulse depends on the bulk modulus K of the oil and the total oil volume V_0 as

$$Q = \frac{\Delta V}{\Delta t} = -\frac{V_0}{K} \cdot \frac{\Delta p}{\Delta t}. \tag{5.1}$$

The complete test assembly had a volume of 136 cm^3, which resulted in a maximal oil flow of about 130 l/min with a maximal temporal pressure gradient of 160 $kbar/s$.

5.1.2 Experimental Procedure

The experiments consisted of four runs with four specimens each, resulting in a total of 16 test specimens. Each run has been performed with different dynamic load parameters. At each run, two specimens were equipped with strain gauges, except for the first run, which had three specimens equipped

with strain gauges. The corresponding load parameters and part designations are given in Table 5.1.

Table 5.1: Variable load parameters.

Run	Part №	Frequency	Drop Rate	Parts w/ Strain Gauges
1	210-213	3 Hz	80 kbar/s	210, 211, 212
2	220-223	3 Hz	10 kbar/s	222, 223
3	230-233	6 Hz	80 kbar/s	232, 233
4	240-243	6 Hz	10 kbar/s	242, 243

The calculated load pressure pulses used in the simulations and the measured load pressure during the pulsation tests at a frequency of 3 Hz and 6 Hz are visualized in Figure 5.3. The applied load pressure is divided into two segments. The first segment consists of the pressure build-up, where the load pressure is increased from the low-pressure level p_{min} to the high-pressure level p_{max} and held for a certain amount of time. The pressure build-up and the time of the high-pressure level have taken one-half of the pulse time. This time span is denoted as the high-pressure phase during which the specimens are connected to the high-pressure line.

The second segment, which is denoted as the low-pressure phase, consists of the pressure drop (pressure release) and the duration during which the low-pressure level is held. The temporal pressure gradient is not constant throughout the pressure drop. Due to the mechanical properties of the pulse generator, a certain amount of time is required to open the pressure outlet completely. At first, the pressure outlet is partially opened, resulting in a reduced pressure gradient. The maximal pressure gradient is achieved once the pressure outlet is opened completely. Eventually, the pressure gradient decreases as the pressure difference between the test specimens and the tank falls. The average pressure drop rate $\bar{dp}_{dr}$ is defined as the average temporal pressure gradient, given by the ratio of the drop duration Δt_{dr} to the high-pressure level p_{max} as

$$\bar{dp}_{dr} = \frac{p_{max}}{\Delta t_{dr}}. \tag{5.2}$$

A 1% tolerance band determined the drop duration Δt_{dr}. The pressure drop began once the measured pressure was 4 bar below the theoretical high-pressure level and ended once it was first situated 4 bar above the low-pressure

level. At last, the load pressure is held at the low-pressure level until the end of the pulse.

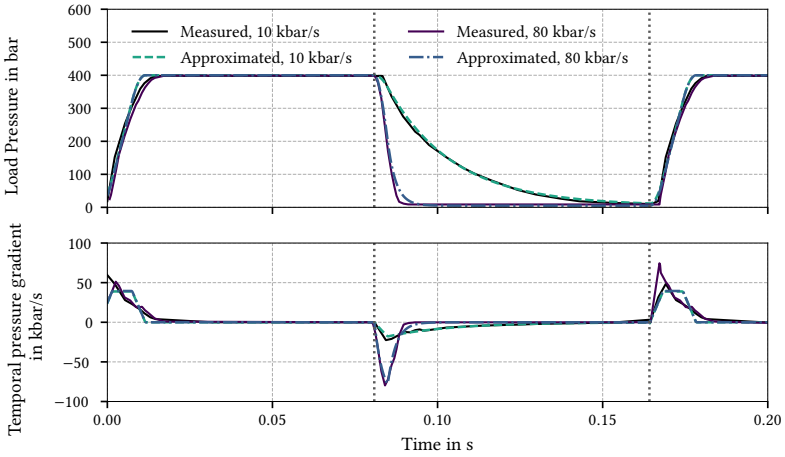

Figure 5.3: Measured load pressure and temporal pressure gradients of the test setup (solid line) and applied load pressure of the simulations (dashed) at a frequency of 6 Hz.

The measured load pressure was used as input pressure for the model validation. However, an approximation of the pressure build-up and the pressure drop was required for the subsequent parameter study.

The pressure build-up was approximated by a linear build-up rate dp_{bu} as

$$p(t) = dp_{bu} \cdot t + p_{min}. \tag{5.3}$$

The pressure drop with an average drop rate of $\bar{dp}_{dr}$ was approximated by a capacitive discharge as

$$p(t) = (p_{max} - p_{min})e^{-\tau_{dp}t} + p_{min} \tag{5.4}$$

with time-constant τ_{dp} defined as

$$\tau_{dp} = 2\frac{\bar{dp}_{dr}}{p_{max}}. \tag{5.5}$$

The pressure build-up (rate) $dp_{bu} = 40\ kbar/s$ and the high-pressure level of $p_{max} = 400\ bar$ have been equal for all runs. The tank pre-tension of 5 bar has defined the low-pressure level. An overview of all constant load parameters is given in Table 5.2.

Table 5.2: Constant load parameters

Parameter	Value	Unit
High Pressure (p_{max})	400	bar
Low Pressure (p_{min})	5	bar
Rise Time	10	ms
Rise Rate	40	$kbar/s$
Density (40 °C)	843.75	kg/m^3
kin. Viscosity (40 °C)	46	mm^2/s
dyn. Viscosity (40 °C)	$38.8{\cdot}10^{-3}$	$Pa \cdot s$
High- to Low-Pressure Time Ratio	50/50	-
Oil Type	HLP 46	-
Specimen Material	S235JR	-

Once the crack growth reached the outer surface of the test specimen, the specimen started leaking oil. The experiment continued until a float switch in the drainage of the pressure chamber detected the leakage and stopped the pulsation. Once the test rig stopped, the operator removed the leaking specimen manually, and the run continued with the remaining specimen.

5.1.3 Optical Analysis

The geometry of the crack is vital for the flow regimes inside the crack. Two general assumptions have been made regarding the crack geometry. One concerns the extent and advancement of the crack front, and the other concerns the crack surface profile of a straight crack. An optical analysis of the crack has been performed to verify both assumptions. The test specimens were cut in two directions to expose the crack. The **A-A** and **B-B** directions are visualized in Figure 5.4. The cut in the **A-A** direction was perpendicular to the crack and showed the crack profile in the x-y plane. Sequential cuts in the **B-B** direction (x-direction of the crack coordinate system) revealed the crack front in the x-z plane.

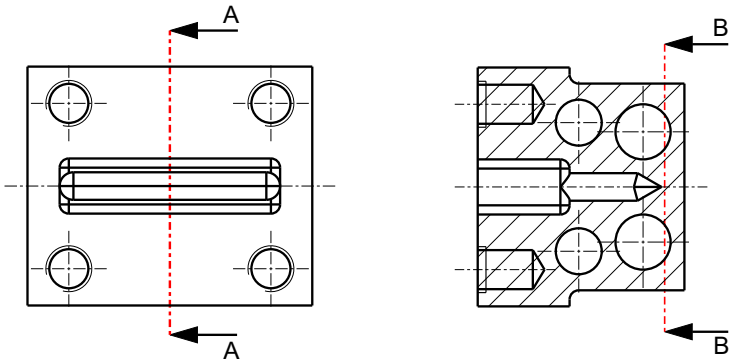

(a) Cut A-A. **(b)** Cut B-B.

Figure 5.4: Cutting planes of the microscopic (cut A-A) and the dye penetrant (cut B-B) inspection.

5.1.3.1 Crack Front

An assumption of the crack front has been made based on the preliminary simulations with the SMART tool (Section 4.1.4). The extent of the crack and the shape of the crack front have been revealed by removing the specimen surface along the crack's length from the direction of the crack tip (see Figure 5.4b). On the revealed surface, the extent of the crack has been measured optically by dye penetration (see Figure 5.5b). The measurements have been performed in steps of 1 *mm* of the surface.

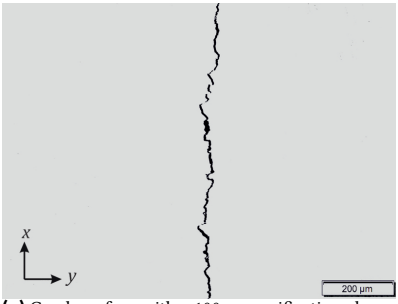

(a) Crack surface with a 100x magnification along cut A-A.

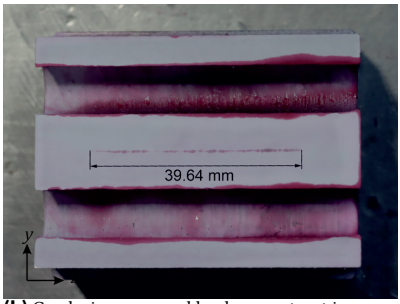

(b) Crack size measured by dye penetrant inspection along cut B-B.

Figure 5.5: Optical analysis of the crack front and the crack's surface profile.

The results for part 220, as well as the derivation of the measurements compared to the corresponding simulated crack front, are depicted in Figure 5.6. The results are similar to the second specimen, Part 231, which is visualized in the Appendix in Figure A.1. The measurements for the two specimens differ due to the final crack advancement at which the experiments have been stopped. The measured crack front aligns with the simulated crack front at the lower layers close to the crack opening. Closer to the surface of the test specimens, the observed deviations between the measurement and the approximation were higher. Possible explanations for this behavior are the influence of local non-linearities and the increasing plastic deformation once the crack reaches the surface. As the analysis requires the destruction of the specimen, this investigation has been made only on two specimens at the end of the fatigue experiments.

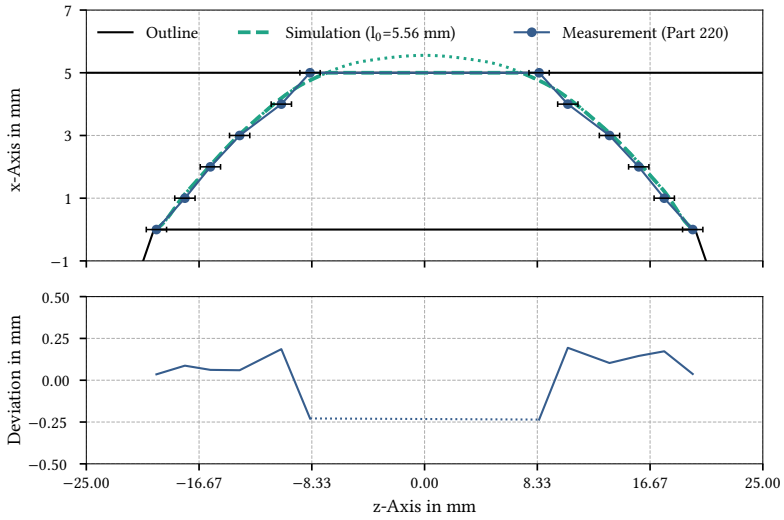

Figure 5.6: Crack front measurement and deviation of the crack front approximation for part 220.

The approximation of the crack front provides the shape of the crack depending on the characteristic crack length. The approximation can be used the other way around to determine the characteristic crack length for a measured

crack front. Hence, when the size of the crack front is known at a position x, the crack's length can be estimated.

At the end of the fatigue experiments, the crack widths on the outer surface ($x = 5\ mm$) have been measured by dye penetration. Table A.4 in the Appendix gives the measured crack widths and estimated characteristic crack lengths. A variation of the crack widths between specimens was observed as the leakage detection stopping the experiments does not accurately match the current crack size. The compliance simulations for the validation of the simulations models were adjusted to the measured crack extent of the compared specimen.

5.1.3.2 Crack Surface Profile

The fluid flow inside the crack depends on the crack surface profile. While the assumption of a straight crack holds on a large scale and for high crack opening displacement, the fluid flows need to follow the surface profile for smaller crack opening displacement. The specimens have been cut open at the cut **A-A** for optical analysis of the crack's surface profile and the direction of crack advancement. Figure 5.5a depicts the crack profile along the x-axis recorded by an optical microscope with a magnification of 100. The crack is unloaded and closed. However, its pathway is visible due to residual oil (in black). The material granulation around the crack path was made visible by the etching of the surface. Figure 5.7 depicts two high-magnified recordings of the surface roughness of the crack. In this area, the crack path turns perpendicular to the opening displacement, and the asperities narrow the cross-section of the fluid flow.

Figure 5.8 visualizes the surface profiles extracted from the optical recordings. Even though the general direction of the crack advancement was in a straight line along the x-direction, the magnified recordings proved that the crack's surface roughness reduces the cross-section of the oil flow. Multiple segments where the crack closes prematurely due to an incompatibility of the crack faces were observed. In these segments, the cross-section of the crack was reduced even in the opened state. Additionally, the crack was partially orientated in the y-direction in many parts. In these segments, the effective cross-section of the fluid flow is lower than the crack opening displacement.

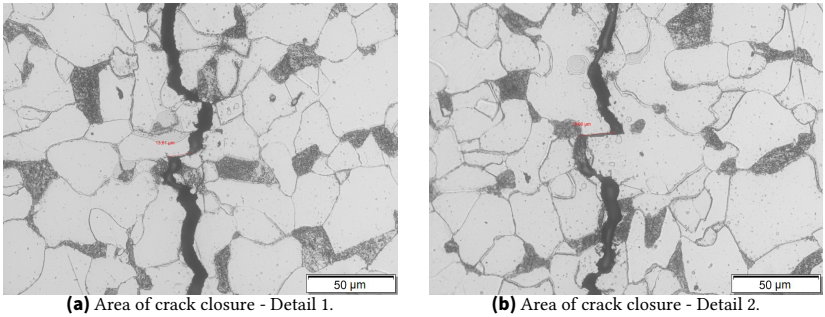

(a) Area of crack closure - Detail 1. **(b)** Area of crack closure - Detail 2.

Figure 5.7: Recording of areas of crack closure with a magnification of 500x.

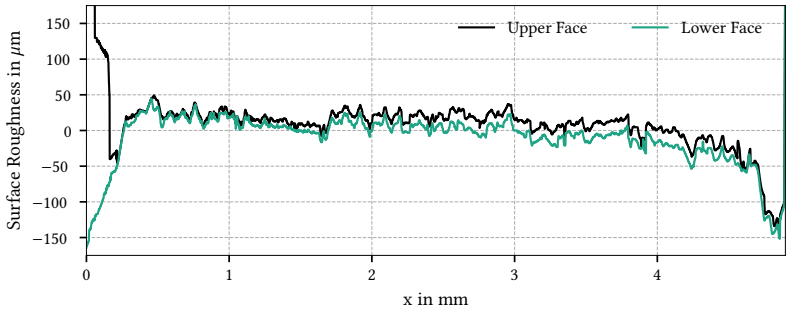

Figure 5.8: Measured surface profile of the grown fatigue crack with an aspect ratio of 1:5.

The theoretic cross-section of the fluid flow inside the crack can be derived by superposing the macroscopic crack face displacement with the local surface. Figure 5.9 depicts the theoretic cross-section of the crack at a load pressure of 270 *bar* and 400 *bar*. However, the constructed cross-section does not take into account local deformations due to the pressure on the asperities.

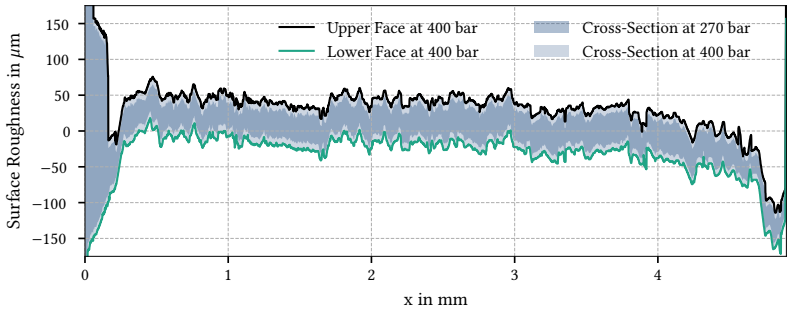

Figure 5.9: Theoretic cross-section of the crack at a load pressure of $p_0 = 270\ bar$ and $p_0 = 400\ bar$.

5.2 Strain Measurement

The objective of the strain measurements was to confirm the presence of oil and the oil flow inside the crack. If oil remains inside the crack and prevents the crack faces from returning to their initial position, the specimens remain deformed. Based on the finite-element analysis of the specimens, the positions of the strain gauges were chosen, and the required measurement accuracy was defined. This section describes the measurement setup and the implemented post-processing.

5.2.1 Strain Gauge Setup

Three possible strain gauge positions (channels) were examined, of which two were chosen for the measurement setup. Each channel consists of two symmetrically placed strain gauges undergoing an identical deformation. The channels were located in different spatial directions and were affected differently by the displacement of the crack faces. An analog-digital converter (ADC) circuit converted the bridge offset for post-processing.

5.2.1.1 Strain Gauge Placement

The strain gauges' resistance varies with the measurement grid's deformation, indicating the average strain at the location of the grid. Figure 5.10 visualized the three investigated locations (channels) for placement of the strain gauges.

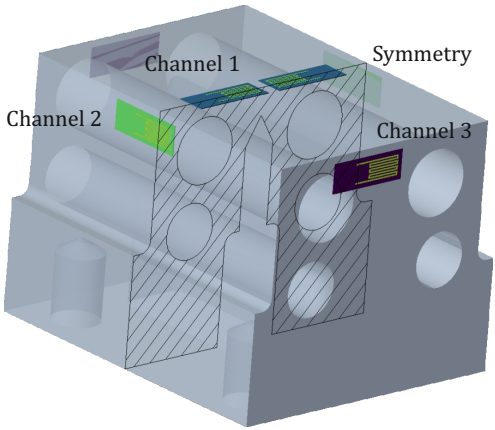

Figure 5.10: Strain gauges positions of channel 1 (teak), channel 2 (green), and channel 3 (purple) with one of the two symmetry planes (black).

The test specimen has six faces where strain gauges could have been placed. However, the surface of the pressure inlet was ruled out due to its distance from the crack and the fixation of the adapter plate. Two of the remaining five faces were identical to the other two because of the specimen's symmetry. Strain gauges have been simulated on the three potential surfaces. The strain gauges were orientated in the direction of the highest normal strain close to the notch. Handling and placing the strain gauges required a tolerance of 1 mm from each edge and each other.

Figure 5.11 shows the simulated strain of each channel for a constant fluid pressure inside the crack of 200 or 400 bar and no external load pressure at the three positions. At position one, the highest absolute strain could be measured. However, the strain measurements decreased with increasing crack sizes, and the strain changed from tensile to compression once the crack reached the specimen's surface at ($l_0 \rightarrow 5\ mm$). The measured strain

at position two is lower than at position one, but in contrast to position one, the strain at position two increased monotonously. The measured strain at position three is lower than at the other two locations.

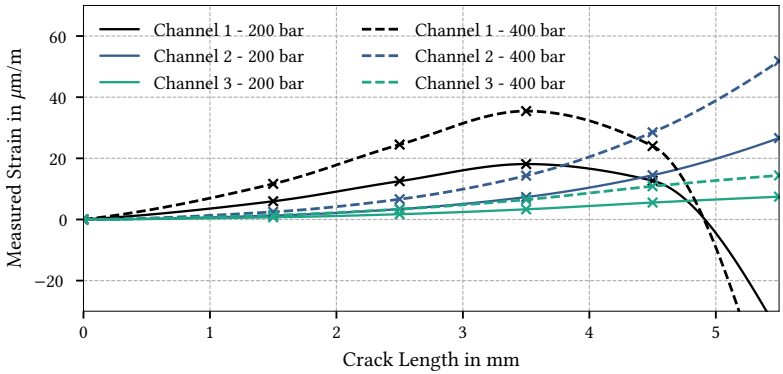

Figure 5.11: Expected strain measurements due to fluid pressure on the crack faces at the three proposed locations (solid line: 200 bar crack pressure, dashed line: 400 bar crack pressure)

Another important aspect is the homogeneity of the strain distribution at the proposed positions. The strain gauges measure the average local strain over the size of the measurement grid. A strongly inhomogeneous distribution is prone to measurement errors due to the assembly tolerance of the strain gauges. Figure 5.12 depicts the local strain distribution around the center of the proposed strain gauge positions in the longitudinal and lateral directions. The measurement grid of the utilized strain gauges has a longitudinal size of 6 *mm*. The strain at position one was highly inhomogeneous once the cracks were longer and was more likely to suffer from measurement errors due to the assembly tolerances. Despite the disadvantages of position one, the test specimens have been equipped with measurement gauges on positions one and two. Position one has been chosen due to the high absolute measurements. Position two has been chosen due to the monotonic increase and the high homogeneity.

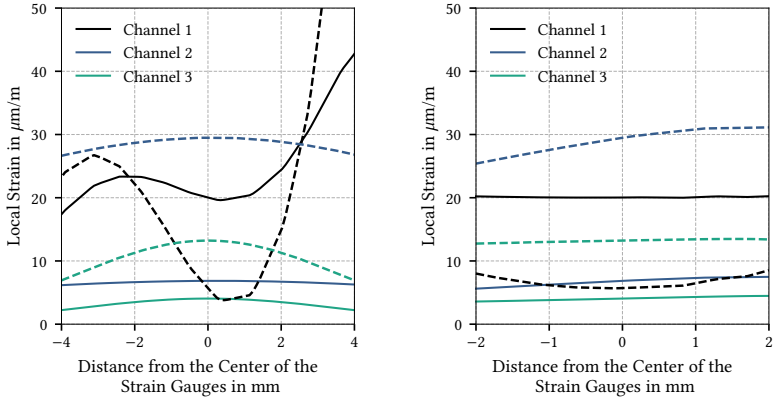

(a) Longitudinal distribution.

(b) Lateral distribution.

Figure 5.12: Local strain distribution in relation to the center of the strain gauges measurement grid center (oil pressure: 400 bar, crack size: 2.5 mm (solid), 4.5 mm (dashed)).

5.2.1.2 Analog Digital Conversion

The strain gauges were wired as Wheatstone bridges to measure their resistance. Each Wheatstone bridge consisted of two strain gauges and two resistors. The strain gauge's resistance varies when the strain gauge's measurement grid is deformed. As the strain gauges' resistance changes, the bridge becomes unbalanced, resulting in a voltage offset proportional to the resistance change. Hence, a variation of the strain gauge resistances provokes a bridge offset proportional to the strain. Theoretically, in the undeformed state, the resistance of the two resistors and the strain gauges are equal, and the bridge is balanced. In reality, however, the resistances are never perfectly identical, and the bridge circuit requires calibration to compensate for the initial offset.

Due to the symmetry of the test specimens, each channel had a second gauge placed symmetrically to the first. Figure 5.13 depicts the wiring scheme of one test specimen with four strain gauges providing two strain measurements (channels). Conventional half-bridges are wired with two strain gauges that undergo opposed strain. One strain gauge undergoes tensile strain, and the second strain gauge undergoes compressive strain of the same magnitude.

In this case, the half-bridge provides temperature compensation. Contrary to the conventional case, the two strain gauges on the test specimens are exposed to identical strain. Hence, the half-bridge provided no temperature compensation but amplified the strain measurement and reduced the required accuracy of the analog-digital conversion. The wiring of a conventional half-bridge is impossible as no opposed strain gauges can be placed due to the nature of the pressure force. Two constant resistors complemented the strain gauges to a Wheatstone bridge.

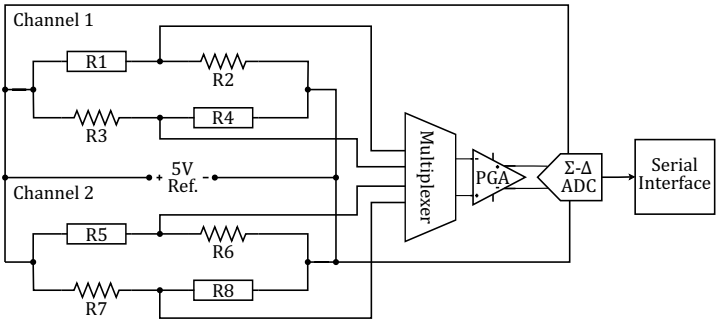

Figure 5.13: Wiring scheme of strain gauges (G) with resistors (R), 5V voltage source, programable gain amplifier (PGA), and an analog-digital converter (ADC), [128]

The deformation caused by the fluid inside the crack ranged between 7 $\mu m/m$ at the third channel and 40 $\mu m/m$ at the second channel. Hence, the analog-digital conversion required microvolt accuracy to determine the in and outflow of the oil. In addition, a high temporal resolution was required for testing drop rates of up to 80 $kbar/s$. The measurement circuit has been designed to achieve microvolt accuracy in combination with a temporal resolution of 1 kHz.

The two strain gauge channels on each specimen have been measured by a multiplexed single-channel analog-digital converter (ADC). First, the multiplexer selected the channel, followed by an integrated programable gain amplifier (PGA) before the ADC. A serial interface then transmitted the measured voltage via SPI to a data recorder. The circuit diagram and the PCB layout are visualized in the Appendix (Figure A.6 and Figure A.5). The used $AD7195$ microchip is an ADC with an integrated two-channel multiplexer and gain amplifier manufactured by Analog Devices, [122].

The maximal single-channel conversion frequency was 4800 Hz. However, the sampling rate was reduced by oversampling to 960 Hz to increase the accuracy. The ADC has an internal SINC4 filter, [122], which requires four conversions for a fully settled conversion after switching the channel. Hence, switching the channels between two conversions was impossible, and the channels were recorded sequentially. A high spatial resolution was required to measure the pressure pulse. The effect of the crack advancement, on the other hand, happened on longer time scales. The channel was switched every two seconds as the crack advancement during this timespan was negligible. A measurement cycle consisted of measuring the first channel for two seconds, switching to the second channel, and measuring this channel for the same duration before switching back to the first channel for the next cycle.

5.2.1.3 Noise Performance

The measurement drift and the peak-to-peak noise characterized the noise performance of the total setup. Figure 5.14 depicts the measured voltage and the moving standard deviation of an unloaded specimen.

Standard Deviation. The measurement circuit had a moving standard deviation within a one-second window of about $\sigma_{SD} \approx 0.02\ \mu V$. Infrequent measurement outliers with deviations of up to several microvolts led to peaks in the standard deviation. As the outlier significantly deviated from the other measurements and the expected value, an outlier detection was performed in the post-processing, and the outliers were discarded. The characteristic standard deviation indicated that the system met the targeted microvolt accuracy concerning the short-term sensor noise.

Measurement Drift. In addition to the short-term measurement noise, a long-term drift of the measurements has been observed. The measurements drifted due to the thermal expansion of the test specimens. Given the thermal expansion coefficient of S235 of $\alpha_T = 11.1\ ppm/K$, without compensation, even slight temperature fluctuations of $\Delta T = 1\ K$ would provoke a measurement drift of $\Delta\epsilon \approx 5.2\ \mu V$ (cf. Section 5.2.2). The self-compensation of the strain gauges internally compensates the majority of the thermal drift. In addition, a thermal expansion model was implemented for the post-processing to reduce the remaining thermal drift.

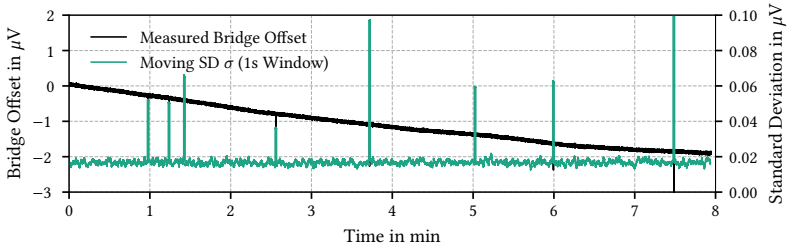

Figure 5.14: Measured voltage (primary y-axis), and the moving standard deviation (SD) with a window of 1 s (secondary y-axis).

Peak to Peak Noise. The peak-to-peak noise of the measurement setup was measured continuously throughout the experiments. Figure 5.15 visualizes the maximal peak-to-peak noise per cycle for a total of 10,000 cycles. The average peak-to-peak noise was $\omega_{p2p} = 0.94\ \mu V$. The histogram shows that the distribution corresponded approximatively to a normal distribution with a standard deviation of $\sigma_{SD,p2p} = 0.38\ \mu V$.

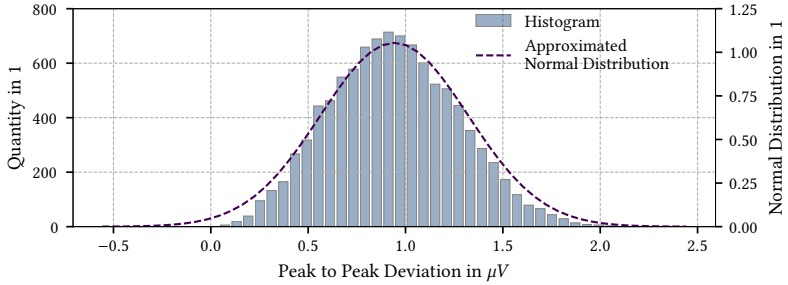

Figure 5.15: Maximal peak-to-peak noise per cycle measured over 10,000 cycles and approximated peak-to-peak noise normal distribution.

5.2.2 Post Processing

In this subsection, the post-processing steps are described. At first, the output of the analog-digital converter is converted into strain values. Afterwards,

two filters are applied to the strain measurements. The cyclic average filter calculated the moving average over consecutive pulsation to reduce the 50 Hz ripples. Subsequently, the thermal expansion model compensated temperature variations. At last, the test rig's idle times were removed from the final measurement sequence.

5.2.2.1 Data Conversion

The quantitative relation between the resistance R_{sg} and the strain ϵ is

$$\Delta R_{sg} = R_{sg} - R_{sg,0} = R_{sg,0} \cdot \epsilon \cdot k_{SG} \tag{5.6}$$

defined by the measurement sensitivity k_{SG} and the nominal resistance $R_{sg,0}$ of the strain gauges.

The AD converters output a 24-bit integer code $Code$ where the first bit is encoded as a sign and 23 bits for the value of the unsigned measurement. The measured voltage value U_m depends on the $Gain$ of the PGA and the reference voltage U_{ref}, [122], as

$$U_m = \left(\frac{Code}{2^{23}} - 1 \right) \cdot \frac{U_{ref}}{Gain}. \tag{5.7}$$

Strain Measurement. Kirchhoff's circuit laws correlate the measured voltage to the bridge's resistors' and the strain gauge's resistances as

$$U_m = \left(\frac{R_2}{R_1 + R_2} - \frac{R_4}{R_3 + R_4} \right) \cdot U_{ex}. \tag{5.8}$$

The resistances of the two fixed resistors $R_{bridge} = R1 = R4$ and both strain gauges $R_{sg} = R2 = R3$ are identical. Hence, equation (5.8) can be simplified, and the sensor's resistance R_{sg} is given as

$$R_{sg} = \frac{U_{ex} - U_m}{U_{ex} + U_m} \cdot R_{bridge}. \tag{5.9}$$

The resistance of the strain gauges depends on the strain and the nominal resistance $R_{sg,0}$ as

$$\epsilon = \frac{1}{k_{SG}} \cdot \left(1 - \frac{R_{sg}}{R_{sg,0}} \right) \tag{5.10}$$

which is for $R_{sg,0} = R_{bridge}$ equivalent to

$$\epsilon = \frac{1}{k_{SG}} \left(1 - \frac{U_{ex} - U_m}{U_{ex} + U_m} \right). \tag{5.11}$$

As the excitation voltage U_{ex} is identical to the reference voltage U_{ref}, the substitution of equation (5.7) into equation (5.11) shows that the strain measurements are independent of the excitation voltage. The strain depends on the measured conversion results as

$$\epsilon = \frac{2}{k_{SG}} \left(\frac{\left(\frac{Code}{2^{23}} - 1 \right)}{Gain + \left(\frac{Code}{2^{23}} - 1 \right)} \right). \tag{5.12}$$

Temperature Measurements. The temperature measurements with PT100 resistances were encoded identically to the strain measurements, but the conversion into a temperature value differed.

The sensor's resistance R_{PT100} is given in accordance with equation (5.9) as

$$R_{PT100} = \frac{U_{ex} - U_m}{U_{ex} + U_m} \cdot R_{bridge}. \tag{5.13}$$

In the next step, the corresponding temperature is calculated using the Callender-Van Dusen equation. The Callender-Van Dusen equation calculates the corresponding temperature for a given resistance of a PT100 sensor, [111]. In the following, the equation for the temperature range of $T \in [0\,°C, 661\,°C]$, is used

$$R_{PT100}(t_k) = R_{PT100,0} \left(1 + A_{PT100} T_{spec}(t_k) + B_{PT100} T_{spec}^2(t_k) \right). \tag{5.14}$$

Solving the quadratic equation and assuming only positive temperatures leads to

$$T_{spec}(t_k) = \frac{-A_{PT100} + \sqrt{A_{PT100}^2 - 4B_{PT100} \left(1 - \frac{R_{PT100}(t_k)}{R_{PT100,0}} \right)}}{2B_{PT100}}. \tag{5.15}$$

The PT100 sensor has a nominal resistance of $R_{PT100,0} = 100\ \Omega$, the parameters of the Callendar-Van Dusen equation are given in the DIN EN IEC 60751, [112], as

$$\begin{aligned} A_{PT100} &= 3.9083 \cdot 10^{-3}, \\ B_{PT100} &= 5.775 \cdot 10^{-7}. \end{aligned} \tag{5.16}$$

5.2.2.2 Cyclic Average Filter

The deformation of the strain gauges was measured through the voltage offset of the Wheatstone bridge. However, the measuring grids of the strain gauges worked to a certain extent as an induction loop. Hence, changing electromagnetic fields induced a parasitic voltage in the Wheatstone bridge, causing a systematic measurement error. Among others, the electric motors driving the test rig's hydraulic pumps provoked strong electromagnetic fields. The dominant frequency corresponds to the rotation rate of the electric pumps. The electric pumps turn at the frequency of the national grid (in Germany: 50 Hz). In addition to the internal 50 Hz suppression of the analog-digital converter, the cyclic average filter has been implemented to decrease the error due to the induced voltage.

The crack advancement occurred in time scales considerably longer than one pulse and even one measurement cycle of two seconds. Therefore, the deformation of specimens for all pressure pulses of one measurement cycle (2 s) was identical, except for measurement errors. As mentioned previously, the crack advancement over one measurement cycle of two seconds (six to twelve pulses) is negligible.

The cyclic average filter detected each pulse i and calculated the arithmetic mean $\tilde{\epsilon}_j(t_k)$ over the $\hat{i}_j$ pulses of the j-th measurement cycle as

$$\tilde{\epsilon}_j(t_k) = \sum_{i=1}^{\hat{i}_j} \epsilon(t_0(j,i) + t_k), \quad \forall\ k \in [0, M] \tag{5.17}$$

with timesteps t_k.

Each pulse i of the cycle j starting at the timestep $t_0(j,i)$ had a total number of M timesteps. The number of pulses per cycle $\hat{i}_j$ depended on the duration of one measurement cycle Δt_c and the pulse frequency f_p as

$$\hat{i}_j = \lfloor \Delta t_c \cdot f_p \rfloor - 1. \tag{5.18}$$

The number of averaged pulses was reduced by one as the measurement cycle was not synchronized with the test rigs, and incomplete pulses at the start and end of the cycle were excluded. The start times $t_0(j, i)$ were defined by the rising edges of the strain as

$$t_0 = \{t_k | k \in \mathbb{N}, \epsilon(t_k) > \epsilon_{th}, \epsilon(t_{k+1}) - \epsilon(t_k) > 0\}. \tag{5.19}$$

For clarity, the indices j and i were omitted in equation (5.19). The strain must surpass the threshold ϵ_{th} for a rising edge to be detected. Figure 5.16 depicts the measured voltage and rising edges corresponding to the start times $t_0(j, i)$. The average pulse is visualized in the enlarged subplot. In contrast to the raw measurements, the cyclic average filter suppressed frequencies that are not a multiple of the pulse frequency.

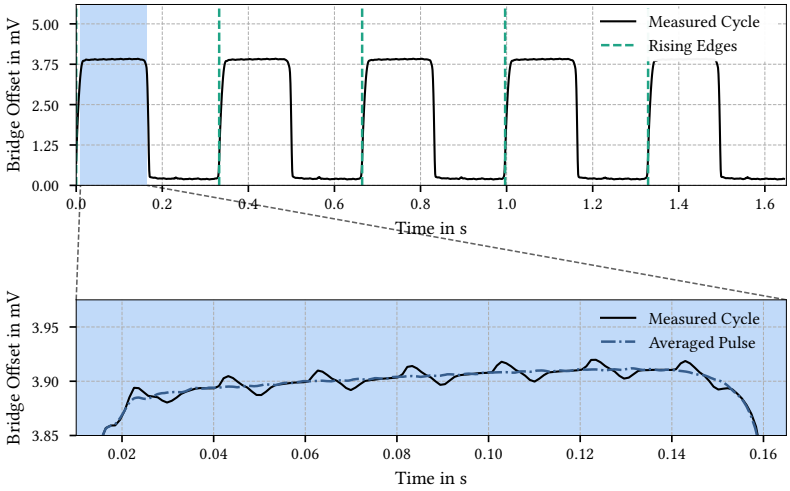

Figure 5.16: Cyclic average filter with rising edges separating the individual pulses and magnification of the averaged pulse of this cycle.

5.2.2.3 Thermal Expansion Compensation

Throughout the experiments, the heat transfer between the oil and the test specimens led to a rise in the test specimens' temperature. In consequence,

the thermal expansion caused an offset in the strain measurements. A thermal expansion compensation that approximates the test specimens' temperature and the thermal offset has been developed. The ambient temperature throughout the experiments has been around $T_{ambient} = 15\ °C$, and any variation due to the weather and day/night changes has been neglected. The test rig started with preheated oil at a temperature of $T_{oil}(t = 0) = 38.5\ °C$. While the pulsation test rig ran, the oil temperature increased over time with a time constant of $\tau_{oil} = 2.5 \cdot 10^{-5}\ K/s$. While the test rig was idle, the oil temperature decreased by the same time constant. The oil temperature was limited to $T_{oil}^{max} = 40.5\ °C$ by an active cooling system. As the total thermal capacity of the oil was significantly higher than the thermal capacity of the test specimens, the oil temperature was assumed to be independent of the heat transfer to the test specimen.

$$T_{oil}(t_k) = \min\left(T_{oil}(t_{k-1}) + \tau_{oil}\Delta t,\ T_{oil}^{max}\right) \tag{5.20}$$

The test specimens were modeled as thermic capacities, and a constant thermal resistance limited the heat transfer. Initially, the test specimens had the ambient temperature $T_{spec}(t = 0) = T_{ambient}$. The temperature approximation differs for the running test rig and the idle state, as only the dominant process was modeled directly. However, a heat transfer between the specimens and the surroundings occurred even while heating up. This heat transfer is only indirectly accounted for by the empiric constants. When running, the specimens' temperature increased until reaching the oil temperature. During the idle state, the specimens' temperature decreased until reaching the ambient temperature again. The temperature of the specimens for both cases is defined as

$$T_{spec}(t_k) = \begin{cases} (1 - e^{-\tau_{on}\cdot\Delta t}) \cdot (T_{oil}(t_k) - T_{spec}(t_{k-1})) + T_{spec}(t_{k-1}) & \text{pulser on,} \\ (1 - e^{-\tau_{off}\cdot\Delta t}) \cdot (T_{ambient} - T_{spec}(t_{k-1})) + T_{spec}(t_{k-1}) & \text{pulser off} \end{cases}. \tag{5.21}$$

The empiric constants were $\tau_{on} = 1.340 \cdot 10^{-4}\ K/s$ and $\tau_{off} = 0.737 \cdot 10^{-5}\ K/s$. The temperature approximation did not model all heat flows and only approximated the temperature with the empiric constants in the case of these particular boundary conditions. Temperature measurements of two specimens determined the constants throughout the test runs. Figure 5.17 shows the measured temperature and the temperature approximation of a specimen with a temperature sensor. A Figure visualizing a second specimen equipped with a temperature sensor is in the Appendix (Figure A.2). The plastic deformation and oil flow through the narrow crack increased as the test specimens

failed. In combination, this provoked significant thermal heat dissipation, and the temperature of the part increased rapidly. As a result, the temperature approximation was no longer valid.

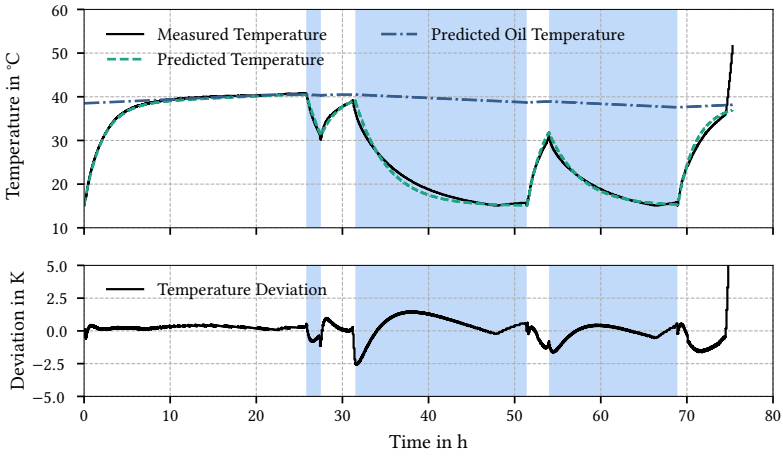

Figure 5.17: Measured specimen temperature, approximated specimen temperature, and approximated oil temperature for part 243. The idle times of the test rig (in blue) started at $t = \{25.8, 31.2, 54.0\}\ h$.

In the relevant temperature range of $T = [15, 45]\ °C$, the thermal expansion coefficient of S235 steel is typical in the range of $\alpha_T = 11.4 - 14\ ppm/K$, [113]. The strain gauges had an internal temperature compensation of $10.8\ ppm/K$, [123]. The measured non-compensated thermal expansion $\Delta\alpha_T \approx 0.157\ ppm/K$ was lower than the expected theoretical value. The strain offset caused by the thermal expansion was calculated by multiplying the thermal expansion coefficient for the non-compensated expansion with the approximated temperature offset

$$\Delta\epsilon_{thermal}(t_k) = \Delta\alpha_T \cdot \left(T_{spec}(t_k) - T_{spec}(t = 0)\right). \tag{5.22}$$

5.2.2.4 Idle Time Detection

In the last step of the post-processing, the idle times of the test rig were removed from the data sequence. The test rig stopped when leakage was

detected and remained idle until the test specimen was removed and the test rig restarted. The test rig was restarted until all four specimens failed.

The idle time detection evaluated the rising edges of the strain measurements (see equation (5.19)). If no rising edges were detected during one measurement cycle, the cycle was removed from the final data sequence.

5.3 Flow Measurements

The simulation of the FSI requires a fluid model, and in the previous section, a reduced laminar flow model was derived. The flow model included flow factors to account for the surface roughness of the crack. The flow factors must be parameterized to the flow regime, which can be determined by simulation or volume flow measurements. In the following, the volume flow through the cracks was measured after the fatigue experiments, and the flow factors were determined accordingly.

5.3.1 Flow Measurement Setup

The setup of the flow measurement test rig was similar to the previous configuration. The setup consisted of a hydraulic circuit supplying the fluid pressure, a sensor measuring the mass flow, and an electric circuit for analog-digital conversion. The challenge of the flow measurement setup was the required accuracy. The following setup was designed to measure volume flows as low as 2.5 ml/h ($4.2 \cdot 10^{-5}$ l/min). Instead of measuring the fluid flow supplied by the hydraulic circuit, the test rig measured the leakage by measuring the mass of the leaked oil. The mass flow through the crack was the ratio of the leaked oil's mass and the duration. This approach had the advantage that no compensation for the internal leakage of the hydraulic components was required, and the accuracy was independent of the hydraulic circuit.

5.3.1.1 Test Rig

Figure 5.18 depicts the schematics of the test rig. The test rig consisted of a hydraulic circuit with a constant pressure source, a pressure relief valve to regulate the pressure, and a directional valve to connect the specimen

to the pressure source or the tank. In contrast to the pulsation test rig, the hydraulic pressure source in this setup was limited to a maximal pressure of 300 bar. The electric circuit consisted of a load cell for the leaked oil, a programmable gain amplifier to amplify the voltage signal of the load cell, and an analog-digital converter to convert the analog into a digital signal, which was then transferred via an SPI. The load cell used strain gauges in a Wheatstone-Bridge configuration to measure the weight of the oil. The analog-digital converter measuring the bridge offset of the load cell had a conversion frequency of 10 Hz. The voltage measurements were oversampled to a frequency of 1 Hz.

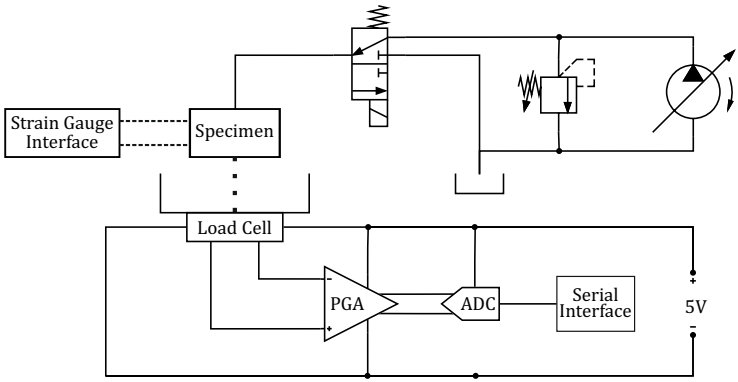

Figure 5.18: Hydraulic schematics of the test rig for the flow measurements. The hydraulic circuit provided the load pressure. The load cell connected to the electric circuit measured the leakage.

5.3.1.2 Noise Performance

Figure 5.19 shows the sensor drift and the moving standard deviation of the unloaded load cell over eight minutes. The drift and the sensor noise of the test setup were measured in the unloaded state without mass flow. Due to the slow dynamic behavior of the mass measurements, the moving standard deviation was calculated with a window of 60 s. The moving standard deviation of the mass measurement remained below $\sigma_{SD} < 0.1\ g$, and the long-term sensor drift remained below the targeted $|\Delta m| < 1\ g$. The peak-to-peak accuracy of the test setup was 0.5 g.

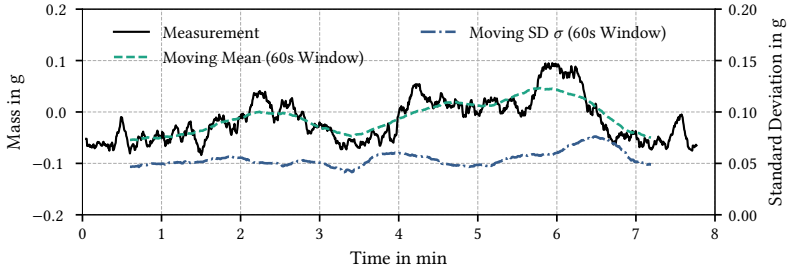

Figure 5.19: Load cell measurement of an unloaded load cell, moving average (main axis), and the moving standard deviation (secondary axis) with a window of 60 *s*.

The measurement of the oil flow through the crack onto the load cell is discontinuous, as the smallest quantity of oil getting onto the load cell was one droplet. As no fractional droplets can be measured, this adds a discretization error to the measurements of the magnitude of one droplet. However, the weight of one droplet was below the measurement accuracy of 1 *g*. The relative influence of the discretization error can be minimized by increasing the measurement period.

5.3.1.3 Experimental Procedure

The specimen was put under the defined pressure for a specific amount of time, and the test rig measured the total mass of the oil leaking through the fatigue crack of the damaged specimens. Dividing the oil mass by the duration gives the oil flow through the crack. The measurement time for the specific pressure levels is given in Table 5.3. As the oil flow was lower, the measurement periods were longer at the lower pressure levels to achieve the same relative accuracy. Longer measurement periods increased the total amount of oil and decreased the discretization error due to the lack of fractional droplets. Nevertheless, due to the drift of the evaluation circuit, the measurement duration remained a trade-off between the total amount of leaked oil and the error due to the circuit's drift.

The oil temperature has been kept constant during the flow experiments. In theory, the oil flow through the crack produced heat as the oil was relaxed to ambient pressure, and the specimen's temperature was prone to increase

Table 5.3: Pressure levels and measurement duration of the flow measurements.

Pressure in *bar*	115	140	170	200	230	270
Duration in *min*	30	25	20	15	10	5

during the measurements. An increasing temperature would decrease the oil's viscosity and increase the total mass flow through the crack. However, the thermal capacity and conduction of the test specimens and the hydraulic system were sufficient to keep the specimen's temperature constant during the static flow measurements at a pressure of up to 300 *bar*. The measurements of the leaked oil mass m_i, $\forall i \in [0, M]$ were evaluated by a linear (first-order) least-square regression with coefficients $[a_0, a_1]$, [114]:

$$\begin{bmatrix} a_0 \\ a_1 \end{bmatrix} = \left(\begin{bmatrix} 1 & 1 & \cdots & 1 \\ t_1 & t_2 & \cdots & t_M \end{bmatrix} \begin{bmatrix} 1 & t_1 \\ 1 & t_2 \\ \vdots & \vdots \\ 1 & t_M \end{bmatrix} \right)^{-1} \begin{bmatrix} 1 & 1 & \cdots & 1 \\ t_1 & t_2 & \cdots & t_M \end{bmatrix} \begin{bmatrix} m_1 \\ m_2 \\ \vdots \\ m_M \end{bmatrix} \tag{5.23}$$

The gradient of the first-order polynomial a_1 is the mass flow per time unit. Figure 5.20 depicts the raw mass values measured for one specimen and the corresponding regressions. No significant deviation between the linear regressions and the measurements was observed. This supports the assumption that the measurement noise was negligible and that the heat dissipation due to the oil flow had no influence. The measured mass flows at a pressure of 115 *bar* remained within the range of the measurement noise and were excluded from the evaluation.

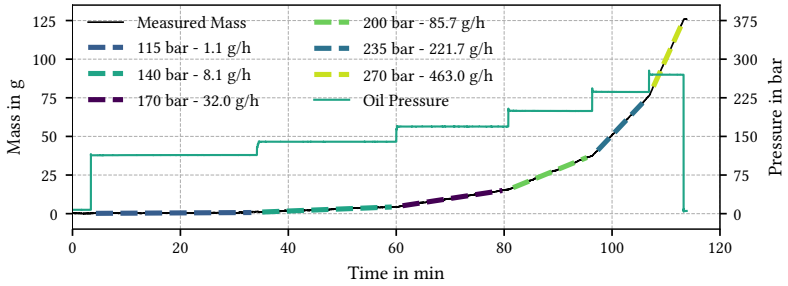

Figure 5.20: Raw values of the leaked oil mass for part 231 and corresponding linear regressions.

5.3.2 Measured Volume Flow

Table 5.4 gives the measured volume flow in ml/h of the tested specimens. The measured volume flow of each measured specimen differed due to different crack sizes and surface profiles. In the following, the expected volume flow for each specimen based on the assumption of a smooth surface has been calculated, and the flow factors have been determined.

Table 5.4: Measured volume flow in ml/h for a load pressure from 140 to 270 bar.

No.\P.	140 bar	170 bar	200 bar	230 bar	270 bar
210	11.6	35.8	94.0	204.9	510.4
212	2.8	20.5	63.4	159.1	445.6
220	7.0	11.6	31.3	99.9	336.0
222	10.2	28.3	76.6	192.6	535.9
231	9.8	39.0	103.0	227.1	549.9
233	1.2	11.4	57.5	191.4	594.3
242	6.2	34.5	100.4	259.7	703.8
243	1.9	24.8	108.8	282.1	778.3

5.3.3 Flow Factors

The laminar flow model gave the expected volume flow under the assumption of smooth surfaces (flow factor $\theta = 1$). The volume flow per unit length was multiplied by the crack width at the outer surface. The expected volume flow varied for each specimen as the crack extent was not identical, and the flow factors were approximated individually.

The averaged flow factor is defined as the ratio

$$\bar{\theta} = \frac{\bar{q}_m}{\bar{q}_p}. \tag{5.24}$$

between the measured flow $\bar{q}_m$ and the theoretical flow $\bar{q}_p$ under the assumption of a smooth surface.

If the assumption of a smooth surface holds, the average flow factor is equal to one. Figure 5.21 depicts the averaged flow factors for the measured pressure levels of the specimens of the second batch. The average flow factor was below one, indicating that the surface profile significantly influenced the fluid flow. An increase in the flow factors was observed with increasing load pressure. In general, flow factors depend on the cross-section height as the influence of the surface profile is more significant when the ratio between the surface roughness and the flow's cross-section is large, [70]. In the case of the investigated specimens, the cross-section height is proportional to the pressure level, explaining the correlation between the flow factors and the load pressure.
The variation of the average flow factors can not be explained by the measurement error of the flow measurements. Each crack path has an individual crack path, see Section 5.1.3, and, hence, individual flow characteristics. In the following, the individual flow factors are assumed to be normally distributed, and the σ confidence interval, including approximately 68 % of all similar cracks, was determined, [115].

In contrast to the average flow factor, the flow factors are unknown and can not be directly deduced from the measurements as the cross-section height varies along the crack of the measured specimens. Instead, the flow factors $\theta(h)$ were approximated with a chosen shape function.
The flow factors $\theta(h)$ are defined as the ratio of the measured real flow $q_m(h)$

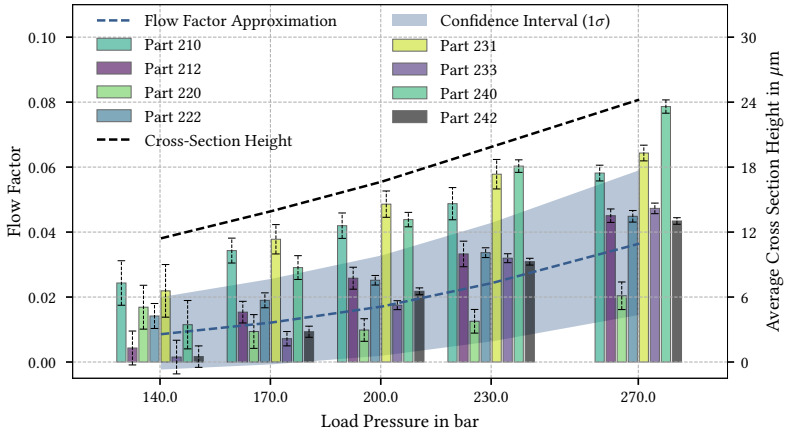

Figure 5.21: Measured average flow factors with error interval (bar chart). The average flow factors resulting from the flow factors approximation in blue with the σ_{SD} confidence area and the corresponding average cross-section height in black (line chart).

and the theoretical flow $q_p(h)$ inside a control volume with constant height h under the assumption of a smooth surface

$$\theta(h) = \frac{q_m(h)}{q_p(h)}. \tag{5.25}$$

The hydraulic resistance R_h is the inverse coefficient of the pressure loss and the steady-state volume flow, [116]. Hence, the theoretical steady-state volume flow along a flow line with constant height h can be expressed as

$$q_p(h) = \frac{1}{R_h(h)}\Delta p. \tag{5.26}$$

The hydraulic resistance is the integral along the streamline s of the hydraulic resistances multiplied by the flow factors. If the streamline is divided into N discrete sections i, the approximation of the hydraulic resistance is given as

$$\hat{R}_h = \int_0^{l_0} \frac{1}{\theta(h)} R_h(h) ds \approx \sum_{i=0}^{N} \frac{1}{\theta(h_i)} R_h(h_i). \tag{5.27}$$

The cross-section height h_i was known from the compliance simulations (Section 2.2). The hydraulic resistance follows accordingly from equation ((4.17)). Two different shape functions were compared for the approximation of the unknown function $\theta(h)$, a linear or a quadratic one:

1. Linear Shape Function:

$$\theta(h) = \begin{cases} C_0 & h < h_{th} \\ \min\left(C_1(h - h_{th}) + C_0, 1\right) & otherwise \end{cases} \tag{5.28}$$

2. Quadratic Shape Function:

$$\theta(h) = \begin{cases} C_0 & h < h_{th} \\ \min\left(C_2(h - h_{th})^2 + C_1(h - h_{th}) + C_0, 1\right) & otherwise \end{cases} \tag{5.29}$$

In general, previous studies indicated that the flow factor becomes one when the ratio of the cross-section height h and the arithmetic average profile height R_a is five or higher, [68], [70], [72].

$$\frac{h}{R_a} \gtrsim 5 \tag{5.30}$$

In this case, the arithmetic average profile height was in the range of $R_a \in [15, 25]\ \mu m$. In consequence, this results in an expected flow factor of one for a cross-section height of $h > 120\ \mu m$ and $\theta(h > 120\ \mu m) = 1$ was defined as an additional boundary condition for the approximations.

Table 5.5: Coefficients of the flow factor approximations.

	$C_2\ [\frac{1}{\mu m^2}]$	$C_1\ [\frac{1}{\mu m}]$	$C_0\ [-]$	$h_{th}\ [\mu m]$	$RMSE[-]$
Linear	0	$2.33 \cdot 10^{-3}$	$6.23 \cdot 10^{-3}$	11.97	0.25
σ (lin)	0	$5.44 \cdot 10^{-4}$	$5.48 \cdot 10^{-3}$	3.58	–
Quadratic	$7.26 \cdot 10^{-5}$	$1.92 \cdot 10^{-4}$	$3.34 \cdot 10^{-3}$	4.16	0.26
σ (quad)	$6.31 \cdot 10^{-6}$	$6.43 \cdot 10^{-4}$	$5.70 \cdot 10^{-3}$	0.36	–

The coefficients of the approximations in Table 5.5 were determined by a least-square optimization. Figure 5.22 displays the approximated flow factors. Both approximations are similar in the range of the measured specimens

with cross-section heights below $h \leq 30\ \mu m$. The linear approximation had a smaller average root mean square error (RMSE) but did not satisfy the additional boundary condition and differed significantly from the theoretical expectations at larger cross sections. The flow factors approximated with the quadratic function and the σ confidence interval of the quadratic approximation are displayed in Figure 5.21.

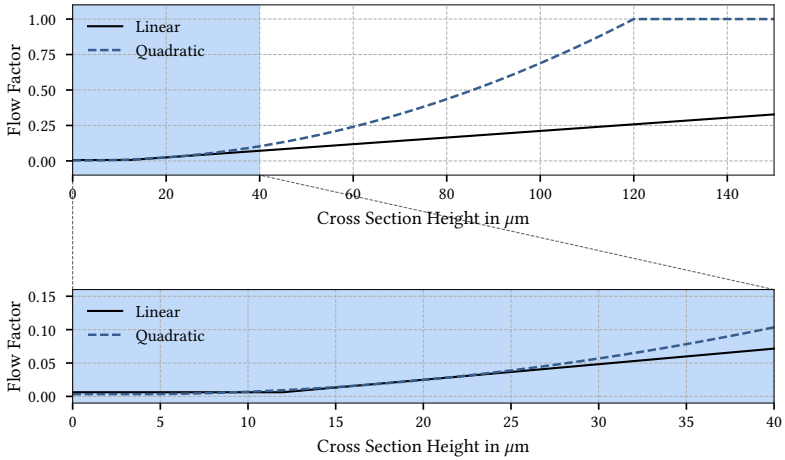

Figure 5.22: Approximated flow factors with the linear and quadratic shape function.

The σ confidence interval includes base flow factors C_0 of zero or less, leading to low flow factors for cross-section heights below 10 μm. At a certain point, the numerical resolution becomes insufficient to represent these flow factors correctly, and a floating point underflow occurs. Numerically, the flow is zero even though the pressure difference should technically lead to a small but existing flow through the cross-section. To prevent an underflow, the base flow factor C_0 has to be at least $C_0 \geq 1 \cdot 10^{-3}$.

5.4 Model Validation

The validation had to overcome the previously mentioned limitation that direct measurements of the fluid flow inside propagating cracks were infeasible. Figure 5.23 visualizes the applied approach. Instead of comparing the fluid-structure interaction, the structural deformation is measured and analyzed. The validation is structured in the following three parts:

1. Validation of the static structural deformation for intact and failed specimens.
2. Evaluation of the structural deformation with advancing cracks and estimation of the current crack length.
3. Validation of the system dynamics in the case of highly transient pressure pulsations.

The first two parts validate the structural model. In contrast to the structural model, the flow model has already been parameterized by measuring the volume flow through cracks. Therefore, the static fluid flow is already validated, and the third part of the validation addresses whether the flow model correctly simulates the dynamic fluid flow inside the crack.

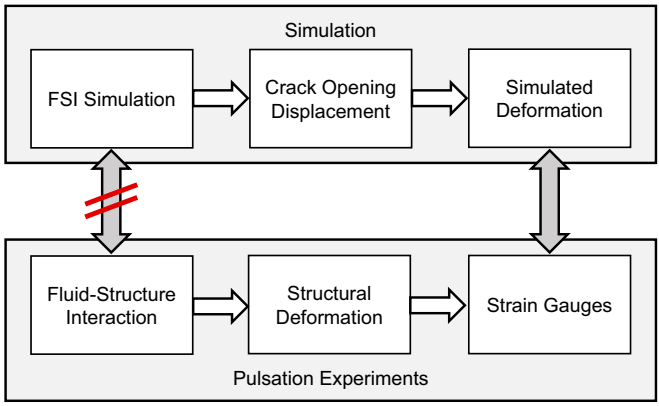

Figure 5.23: Overview of the validation approach as direct validation of the FSI is infeasible.

The validation focuses on the structural deformation instead of the crack propagation rate. Besides the stress amplitude, many macroscopic and mi-

croscopic parameters influence the effective crack propagation rate, e.g., material properties, specimen geometry, temperature, microscopic material, and manufacturing defects. Hence, the crack propagation laws presented in Subsection 2.1.1.5 can only partially represent the crack growth rate, and neglected correlations interfere with the validation.

5.4.1 Static Deformation

The FAE was validated by comparing the simulated strain to static strain measurements of the test specimen. The strain measurements have been performed twice, once before (intact part) and once after the pulsation tests (cracked part). As the extent of the crack has been measured by the optical analysis, a crack of the same extent was integrated into the simulations.

In Figure 5.24, the strain gauge measurements for the intact part and two cracked parts are displayed beside the simulation results. The strain measurements were repeated at different pressure levels, reflecting the increasing strain with increasing load pressure. The strain measurements of the intact part correspond to the simulated deformation of the intact part. The strain measurements of the intact parts were identical for all specimens. After the pulsation tests, the strain measurements differed between parts as the cracks had advanced further in some specimens before the tests were stopped due to leakage.

The measurements of the cracked parts (222 & 233) had an offset compared to the simulation. The offset between the measured and simulated strain did not change with increasing pressure. The incompatibility of the crack faces explained the deviation for the cracked part faces, [41]. In addition to the dynamic oil trapping, the incompatibility of the crack faces prevented the crack from closing completely, and a residual deformation remains inside the part even after a long time and complete discharge of the crack pressure. The microscopic analysis showed that after cutting the parts, the crack faces were not rejoint, and the crack opening remained visible (Figure 5.7).

Before the static strain measurements of each part, the measurement circuit was calibrated. As part of the calibration, the offset of the unloaded part's bridge circuit was set to zero. Due to the crack face incompatibility, the part was deformed even in the unloaded state (residual deformation), and the zero reference had a constant offset compared to the true zero reference used in

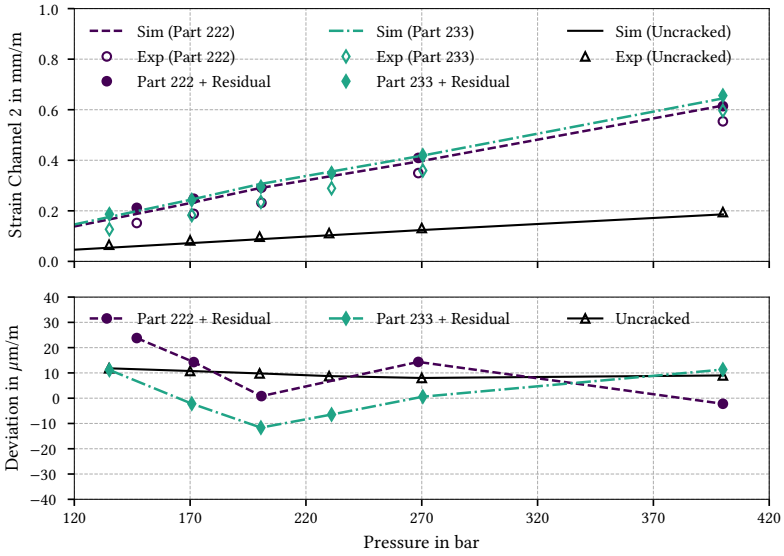

Figure 5.24: Simulation (line plot) and experimental (markers) results of the static strain measurements at channel two for the intact part (black) and of two parts (222 and 233) after the pulsation tests (purple/green), once without and once with compensation of the residual bias (+residual).

the simulation. The size of the offset was equal to the residual deformation of the measured part. The residual deformation, however, did not change the maximal deformation under pressure. In consequence, the measured amplitude is reduced by the calibration offset. As this offset is due to the calibration of the bridge circuit, it is independent of the pressure.

The measured strain corresponded to the simulation when adding the offset due to the residual deformation (legend: *Part # + Residual*). The residual offset was measured over the course of the pulsation tests as the crack face incompatibility increased with the crack advancement. The residual strain corresponded to the strain measurements once the pulsation had stopped and the oil had sufficient time to flow out of the crack. The residual offset was about $\epsilon_{res} \approx 0.06\ mm/m$ for all test specimens.

5.4.2 Crack Advancement

The maximal strain of each pulse is depicted in Figure 5.25a as floating maximum. The increasing maximal strain indicates the crack growth. The structural resistance of the specimen weakened as the crack advanced and the deformation increased. During the first one hundred thousand ($100k$) load cycles, the maximal strain remained constant, and no crack advancement was observed. The crack initiation occurred between $100k$ and $200k$ load cycles forming a macroscopic crack. After $200k$ cycles, stable crack growth took place. At $600k$ pulses, the crack advancement accelerated before the experiment was stopped due to the leakage of the specimen after $644k$ cycles.

Temperature Compensation and Crack Closure In Figure 5.25b, the minimal strain is enlarged. Without temperature compensation (non-compensated), the minimal strain increased due to thermal expansion. The thermal compensation model, however, decreased the measurement drift due to the thermal expansion, and low drift and low noise were observed. The minimal strain increased as the macroscopic crack advanced, indicating fluid-induced and crack face incompatibility-induced crack closure.

Crack Length Estimation In the previous section, the crack extent was measured optically after the pulsation tests, and the static strain measurements were compared to the simulation. On the other hand, no measurement of the current crack length was possible throughout the pulsation tests. However, as the advancing crack weakened the specimens, the maximal strain increased as a function of the crack lengths.
Figure 5.26 depicts the strain as a function of the crack length. The expected strain measurements for different crack lengths were simulated by the FAE and interpolated between the simulated lengths. During the pulsation tests, the pulse count distinguishes the strain measurements. The strain measurements at channel two are strictly increasing, and the simulated strain shown in Figure 5.26 provides a reference between the measured strain and the current crack length. Based on the simulated strain, the current crack length and the crack advancement of each specimen during the pulsation tests were estimated. Knowledge of the current crack length during the experiments is required to prove that the simulation correctly predicts the system dynamics at different crack lengths.

Figure 5.27 displays the estimated crack lengths for the first run with a confidence area of $\Delta\epsilon = \pm 10\ \mu m/m$. The estimated crack lengths' accuracy

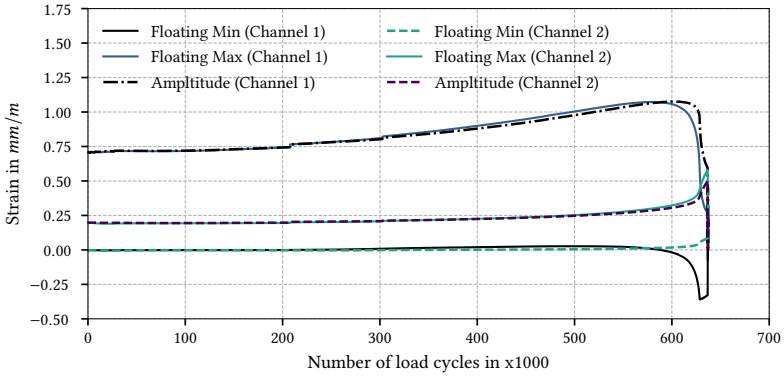

(a) Floating minimum, floating maximum, and amplitude of the measured strain with temperature compensation.

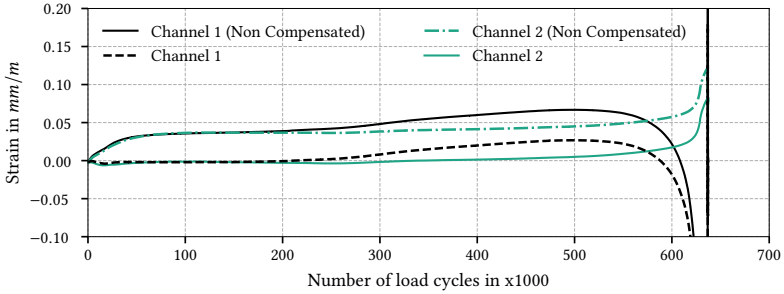

(b) Floating strain minimum with and without temperature compensation.

Figure 5.25: Floating strain minimum and maximum throughout the pulsation tests of specimen 210.

depended on the strain measurement's accuracy, the simulation's accuracy, and the current crack length. The sensor deviation and the post-processing (cyclic average filter, thermal expansion compensation) defined the accuracy of the measurement strain. For a crack length below 0.5 *mm*, the crack advancement provokes only minor changes in the measured strain (low strain gradient), and, therefore, the same measurement accuracy led to higher errors than for longer cracks. At crack lengths above 2.5 *mm*, the strain gradient is considerably higher, and more accurate estimations of the crack lengths are possible. The crack length is only estimated based on the measurements

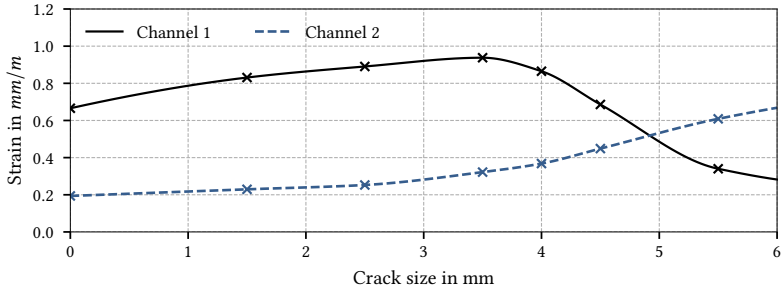

Figure 5.26: Simulation of the maximal strain measured by the strain gauges as a function of the crack lengths at 400 bar.

of channel two. The correlation based on channel one is ambiguous as the measured strain is not strictly increasing. In addition, channel one's accuracy decreased due to the high plastic deformations once the crack ruptured the surface to which the strain gauges were attached.

Comparing the crack advancement of the three specimens of the same run shows that the crack initiation took about 200, 000 load cycles and that the crack initiation time is comparable for all test specimens. While the crack growth rates vary between the tested specimens, all three show the same characteristic behavior. Especially noticeable are two considerable crack advancements shortly after crack initiation at nearly identical crack lengths. A single rupture to establish the macroscopic crack and the characteristic shape of the crack front is a likely explanation. As the pulsation stopped and the damaged specimen was removed (red dashed lines), the remaining specimen(s) showed a decreased crack growth speed for several load changes and even a decrease in the maximal strain. On the one hand, this error is likely partially caused by the thermal compensation, only estimating the current thermal expansion with a certain error. On the other hand, the influence of the specimen's temperature and the cooling down / reheating cycle on the crack propagation rate is unknown.
The analysis demonstrates that even similar specimens from identical material batches experience different crack growth due to variations in their metallurgic structure. Besides the effective stress amplitude, many other parameters and environmental settings influence crack growth, e.g., the cool-down phase due to the removal of the damaged specimen. The analysis shows

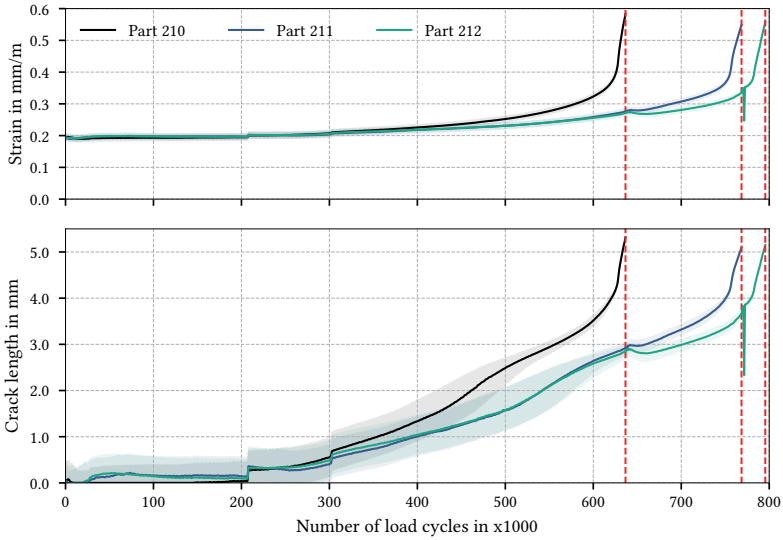

Figure 5.27: Maximal floating strain measured at channel two and corresponding estimated characteristic crack lengths of specimens 210-212 with the semi-transparent confidence area for a strain error of $\Delta\epsilon = \pm 10\ \mu m/m$.

that the crack growth speed varies highly due to parameters not represented in the simulation. Therefore, the fluid-structure interaction simulation inside hydraulic fatigue cracks cannot be validated by its influence on crack advancement. Hence, the mechanical strain provoked by the fluid-structure interaction was evaluated throughout this study to validate the simulation models.

5.4.3 Dynamic System Response

The previous evaluations of the experiments cannot prove that oil penetrated the crack during the pressure pulsations. The strong correlation between the measured maximal strain and the simulation indicates that the crack faces were under pressure. Nevertheless, the correlation alone is not yet sufficient evidence. However, if the dynamic system response is altered due to the oil penetration into the crack, it can support the hypothesis and validate the

simulation. The linear elastic relaxation of S235 steel is quasi-instantaneous, while the fluid flow is time-dependent due to the fluid's viscosity. The previously mentioned crack face incompatibility also provokes premature crack closure but does not provoke a time delay in contrast to the fluid-induced crack closure.

Figure 5.28 depicts the strain measured during a single pressure pulse at different times of the component's life. The legend indicates the estimated crack length and the number of load cycles before the measurement. As observed beforehand, the measured maximal strain and strain amplitude were higher for the pulses at longer crack lengths. At the beginning of the experiment, when no crack had yet formed, the measured strain was zero during the low-pressure phase. With increasing crack lengths, the minimal strain during one pulse increased due to fluid-induced crack closure and crack face incompatibility.

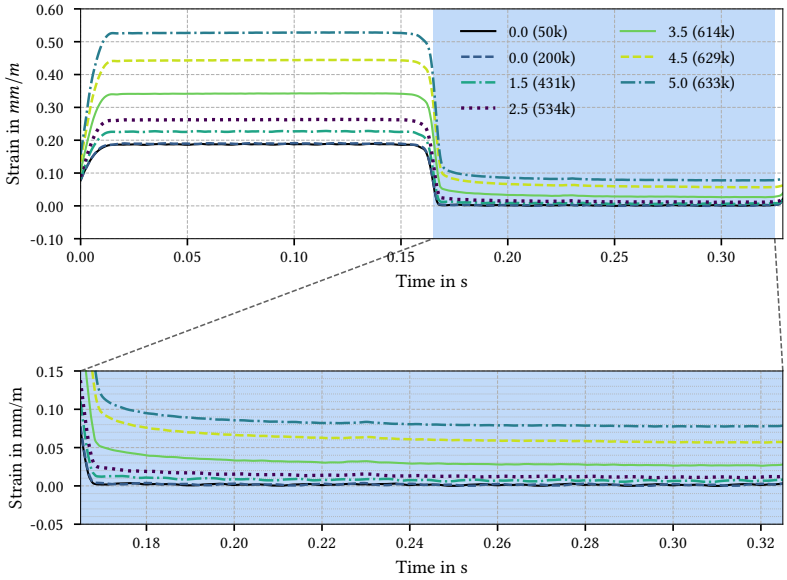

Figure 5.28: Measured strain at channel 2 for one pulse and magnification of the low-pressure phase (specimen no. 210, legend: estimated crack length in mm (pulse count))

Besides the increasing maximal and minimal strain levels, the dynamic strain response of the specimen changed with increasing load cycles. Figure 5.29 shows the relative strain during the low-pressure phase for all three specimens of the first run. The curves were adjusted by a constant offset so that the minimal strain of each cycle was equal to zero to highlight the time delay and the decrease of the strain over time. Without a crack, the strain remains approximately constant during the low-pressure phase. With a developed crack, instead of being constant, the strain decreased during the low-pressure phase even after the complete discharge of the load pressure. The decrease of the strain during the low-pressure phase indicated an out-flow of the oil during the low-pressure phase, as no other known mechanism could provoke the same macroscopic effect.

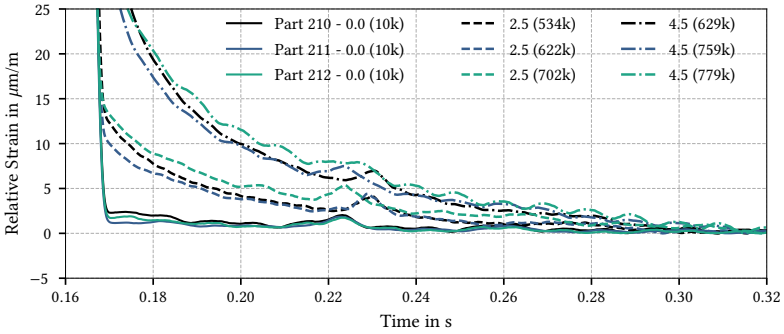

Figure 5.29: Measured relative strain at channel two during the low-pressure phase for specimens 210 (black), 211 (blue), and 212 (green) of run 2-1 (legend: estimated crack length in mm (pulse count)). The offset of the strain was removed so that the minimal relative strain of each pulse was equal to zero.

Besides the oil penetration, a plastic relaxation (creep) at the crack tip could have led theoretically to a time dependency of the structural deformation, [117], [118]. However, the size of the plastic zone and the plastic deformation did not significantly increase as long as the distance to the surface remained sufficient (cf. Subsection 4.2.2.2). Hence, the plastic relaxation would be independent of the crack length and can, therefore, be ruled out.

The low variance compared to the crack growth displayed in Figure 5.27 showed the independence of the dynamic system response from the microscopic metallurgic parameters influencing the crack propagation rate. Its

independence of microscopic material properties makes the dynamic system response well-suited for validating the simulation models. The different orientation of the measurement grid to the electric motors of the test rig explains the differences in the 50 Hz noise.

At last, the question remains whether the simulation with the reduced-order models correctly reproduces the dynamics of the coupled system during crack closure. The fluid flow inside the crack could not be measured directly, and the validation is limited to the macroscopic influence of the fluid. Figure 5.30 depicts the simulated and the measured strain over time for one pulse of part 233 loaded with a pressure pulsation of 6 Hz and a drop rate of 80 $kbar/s$. The simulation correctly reproduces the strain measurements over time for small cracks. For crack lengths above 3.5 mm, however, the measurement and the simulations deviate. The analytic estimation of the plastic deformation explains the higher absolute error at high crack lengths. The estimation does not consider the surface's local influence and underestimates the plastic deformation once the remaining wall thickness is small, as described in Subsection 4.2.2.2.

Figure 5.30b focuses on the low-pressure phase of the pulse. The simulation correctly reproduces the delayed out-flow of the oil. The relative deviation of the simulation remains below 10 % with an even lower deviation most of the time. Relatively high deviations occurred during the instant of the pressure drop. The immediate pressure drop was influenced by the connected valves, fittings, and pipes, which were not included in the simulation. For crack lengths above 3.5 mm, the measured strain is lower than the simulated, showing a faster out-flow of the oil. The faster out-flow is due to a larger cross-section, again explained by the higher plastic deformation due to the small remaining wall thickness. However, the relative deviation remained similar. Figure A.3 and Figure A.4 in the *Appendix* display the low-pressure phase for a pulsation of 3 Hz and drop rates of 80 $kbar/s$ and 10 $kbar/s$.

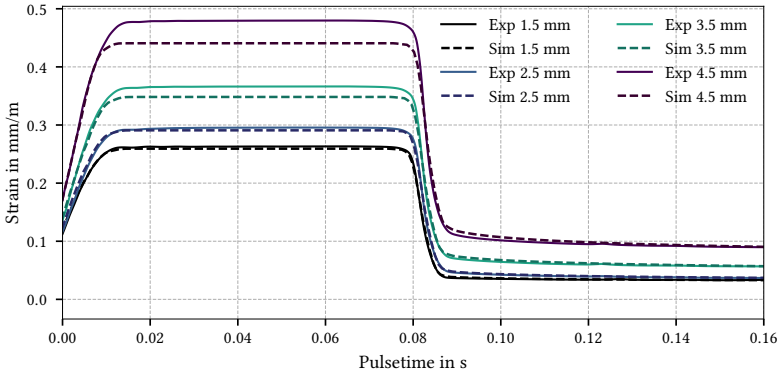

(a) Strain over time for one pressure pulse.

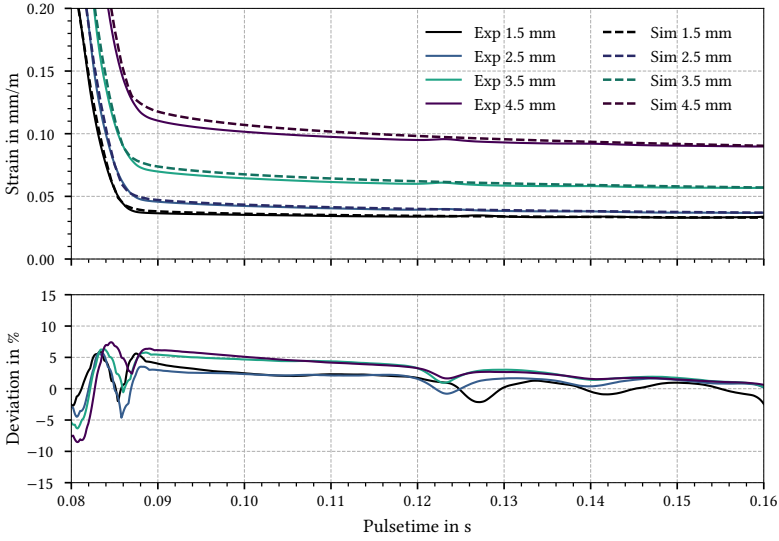

(b) Focussed low-pressure phase.

Figure 5.30: Measured and simulated strain over time of part 233 at crack lengths of $l_0 \in \{1.5, 2.5, 3.5, 4.5\}$ mm.

6 Results

In this chapter, the behavior of the oil in the crack is simulated using the model developed and validated in the previous chapters. The first two sections analyze the primary pressure distribution and the resulting stress amplitude over time. The simulations use the reference parameter set given in Table 6.1. The last subsection examines the influence of the parameters and their reciprocal interaction.
Previous studies indicated that the fluid-structure interaction influences the fatigue stress amplitude by two opposing mechanisms. As the oil penetrates the crack, the hydrostatic pressure acts on the crack faces, increasing the stress amplitude. In contrast to this mechanism, fluid-induced crack closure prevents the crack faces from returning to their initial state, reducing the stress amplitude.

6.1 Pressure Distribution

Figure 6.1 depicts the pressure distribution of one load cycle. At the start of the simulation, the crack was initialized in an unloaded state. The pressure and the crack opening displacement were zero, and no residual plastic deformation existed. As the load pressure built up, the crack opened, and the oil entered, charging the crack faces with the hydrostatic pressure. Plastic deformation was observed in the direct vicinity of the crack tip. Subsequently, the load pressure was released, and the crack opening displacement decreased. However, the oil prevented the crack from closing, and the pressure increased. Especially near the crack tip, high pressures of up to $1,500\ bar$ and only a slight decrease in the crack opening displacement were observed.

A 3D representation of the crack provides a rough overview of the pressure distribution and crack opening over time. For the detailed analysis, however, it is helpful to display the pressure and the crack size at defined locations

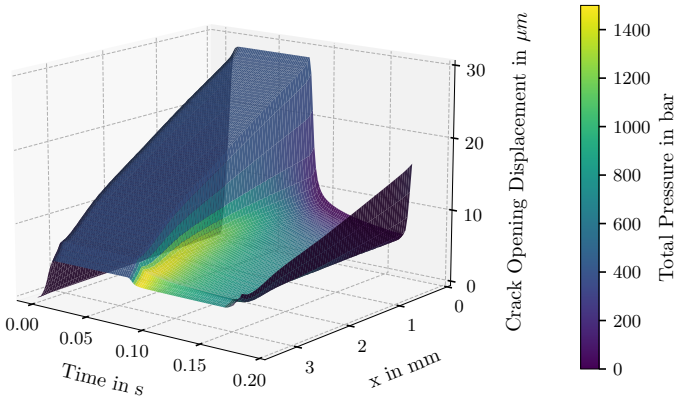

Figure 6.1: Fluid pressure distribution and crack opening displacement inside the crack over time during one pressure pulse.

along the crack in a line diagram. Figure 6.2 depicts the pressure and the crack opening displacement at the locations $x = \{0, 1.5, 3.0, 3.5\}$ *mm*. Initially, a cavitation phase occurred where the crack opened more rapidly than the oil flowed into the crack. Subsequently, as the load pressure remained constant, the crack filled completely. In this state, the pressure inside the crack equals the load pressure. The crack opening displacement decreased as the load pressure was released and the oil flowed out. The oil remaining in the crack led to a substantial increase in the pressure. The pressure inside the crack had to increase to counteract the structural resistance.

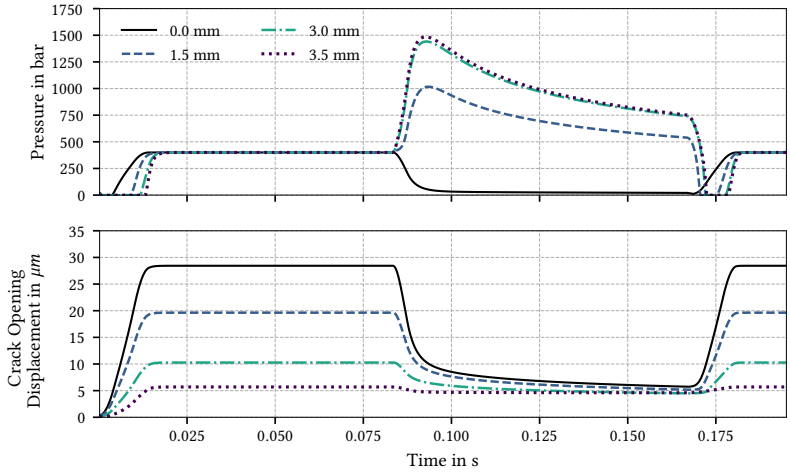

Figure 6.2: Fluid pressure and crack opening displacement at specific positions (x) of the crack.

6.2 Influence on the Stress Amplitude

The previous section demonstrated that both presumed mechanisms are present in the case of fatigue cracks. An additional load on the crack due to the hydrostatic pressure on the crack flanks and fluid-induced crack closure was observed. The extent of the influence of the respective mechanisms based on the stress intensity factors (SIF) is investigated in the following.

Figure 6.3 depicts the SIF for Mode I crack growth (K_I) over two pressure pulses. The figure displays the estimated cumulated cycles without (noFSI) and with fluid-structure interaction (FSI). With FSI, the pressure on the crack faces increases the maximal SIF, and the fluid-induced crack closure increases the minimal SIF in the uncharged state. Hence, the SIF ratio increases, and depending on which effect is more severe, the SIF amplitude increases or decreases.

Three cases were evaluated to quantify the influence of FSI on the crack propagation rate. In the first case, the SIF amplitude includes the hydrostatic pressure on the rack faces and fluid-induced crack closure (Label: FSI). This

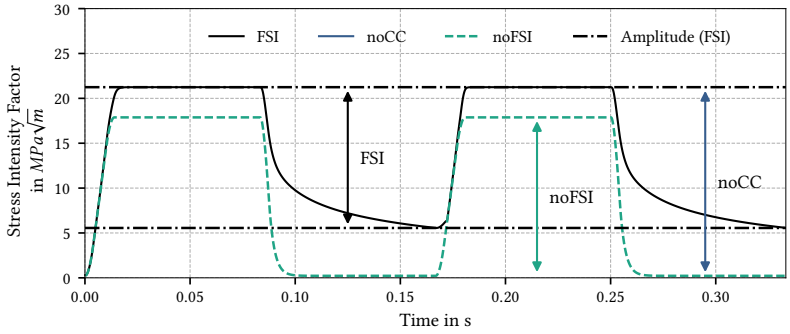

Figure 6.3: Stress Intensity Factor (Mode I) over time with fluid-structure interaction (FSI) and without FSI (noFSI), the corresponding amplitudes, and the amplitude without crack closure (noCC).

case represents typical cyclic loads above a minimal frequency ($\gtrsim 1\ Hz$), e.g., on a pulsation test bench. In the second case, the influence of the hydrostatic pressure on the crack faces is taken into account, but the fluid-induced crack closure is not (Label: noCC). This theoretical case occurs in pulsations with extended low-pressure phases. The amplitude consists of the maximum of the pulse with FSI and the minimum without FSI. The last case is without FSI (Label: noFSI).

The crack propagation rate can be estimated using a suitable fatigue crack growth equation based on the SIF amplitude and the SIF ratio. Figure 6.4 illustrates this for the examined test specimens. The crack propagation rates were calculated with the NASGRO equation described in Subsection 2.1.1.5. The NASGRO equation permits the calculation of crack propagation rates for different SIF ratios with the same material constants.

The hydrostatic pressure increases the crack propagation rate significantly. In the investigated example, the estimated lifetime of the specimens was around 277,000 lifecycles, which was 38.7% lower than the expected 452,000 lifecycles without FSI. The fluid-induced crack closure reduces the crack propagation rate (with FSI), and the lifetime reduction with fluid-induced crack closure was 19.2%. In this example, the influence of the hydrostatic pressure predominates at small crack lengths, whereas the influences of both mechanisms counterbalance each other at medium crack lengths. At the

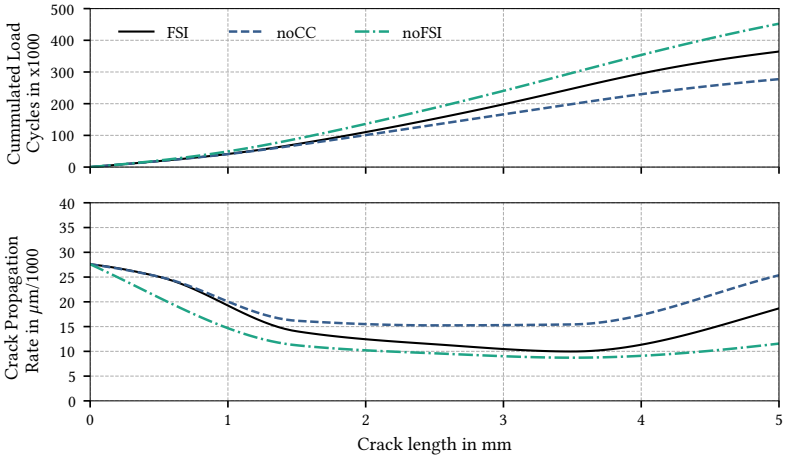

Figure 6.4: Crack propagation rates calculated based on NASGRO in dependence of the FSI mechanisms(legend: FSI - with hydrostatic pressure and fluid-induced crack closure, noCC - with hydrostatic pressure and without fluid-induced crack closure, noFSI - without hydrostatic pressure and fluid-induced crack closure).

end of the crack propagation, the hydrostatic pressure is predominant again before the crack ruptures the surface at a length of $l = 5\ mm$.

Depending on the parameter combination, the influence of the fluid-induced crack closure varies, and, as a consequence, so does the SIF amplitude and the expected lifetime. This example shows the importance of considering the temporal gradient of the load pressure when predicting lifetimes. The fluid-induced crack closure can be negligible in the case of low-frequencies with extended low-pressure phases, leading to an about 39% higher expected crack propagation rate for the test specimens. High-frequency loads with significant fluid-induced crack closure could decrease the crack propagation rate even more. In conclusion, the temporal pressure gradient can influence the estimated lifetime by even more than 39%.

6.3 Parameter Influence

The equations of the reduced-order models describe the Fluid-Structure Interaction and define the input parameters (see Section 4.2). These include the following parameters:

- **Load Pressure:**
  - Low-Pressure (LP) Level
  - High-Pressure (HP) Level
  - Build-Up Rate
  - Drop Rate
  - Duration of the High-Pressure Phase
  - Duration of the Low-Pressure Phase
- **Geometric Parameters:**
  - Crack Length
  - Cross Section (Structural Resistance)
  - Flow Factors
- **Fluid Parameters:**
  - Fluid Viscosity
  - Fluid Compressibility (Bulk Modulus)

The parameters can be divided into three groups. The first group refers to the load pressure being defined following the EN ISO 6803:2017 by the low-pressure level, the high-pressure level, the raise rate, the drop rate, the duration of the high-pressure phase, and the duration of the low-pressure phase. The pressure build-up rate and the duration of the high-pressure phase do not influence the stress amplitude, except in the case of a partially filled crack. However, this particular case is considered separately.
The second group consists of the geometric parameters, including the crack length, the cross-section, and, technically, the flow factors. The cross-section is equivalent to the crack opening displacement, which depends on the structural resistance, as a duplication of the deformation also leads to a duplication of the crack opening displacement. The flow factors result from the

microstructure of the crack. According to the current state of knowledge, whether these are material and component-dependent is unknown. From this group, the crack length and the structural resistance are varied as design parameters in the following investigation.
The last group is made up of the fluid parameters, which in this case are the fluid viscosity and the fluid compressibility (bulk modulus). The amount of dissolved gas primarily influences the fluid compressibility, while the viscosity depends on the oil type and the temperature. Table 6.1 defines the interval of the design parameters. The structural resistance of the component depends on the Young's Modulus (E) of its material, which is varied to modify the structural resistance.

Table 6.1: List of varied design parameters.

Parameter	Unit	Minimum	Reference Value	Maximum
Low-Pressure Level	bar	0	5	50
High-Pressure Level	bar	200	400	600
Drop Rate	$kbar/s$	12	80	450
Low-Pressure Duration	ms	21	83	333
Crack Length	mm	1.5	3.5	4.5
Structural Resistance (E)	GPa	105	210	420
Viscosity	$Pa \cdot s$	0.0097	0.038	0.1552
Bulk Modulus	MPa	666	1000	1500

Despite the restriction to seven parameters, not every parameter combination can be visualized. For this reason, the medians of the absolute gradient were analyzed to quantify the influence of the parameters and their reciprocal impact.

Figure 6.5 illustrates the estimated crack propagation rate of the specimen and the second gradient varying the duration of the low-pressure phase and the crack length. As expected, a shorter duration of the low-pressure phase reduced the crack propagation rate (Figure 6.5a). The crack length also influences the crack growth in a characteristic pattern. Whether the two parameters influence each other is reflected in the second gradient (Figure 6.5b). The mutual influence was generally low for the two parameters. Nevertheless, the parameters influenced each other when the low-pressure phase was short. During a long low-pressure phase, the oil flowed out entirely, whether the cracks were short or long. However, in the case of short low-pressure phases,

the crack lengths had a higher influence on how much oil remained inside the crack.

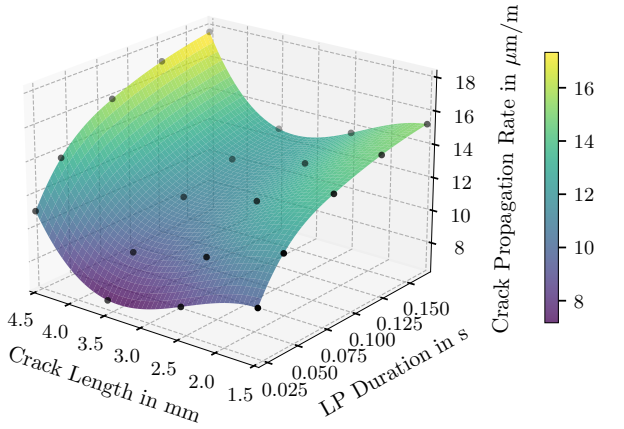

(a) Stress Intensity Factor (Mode I).

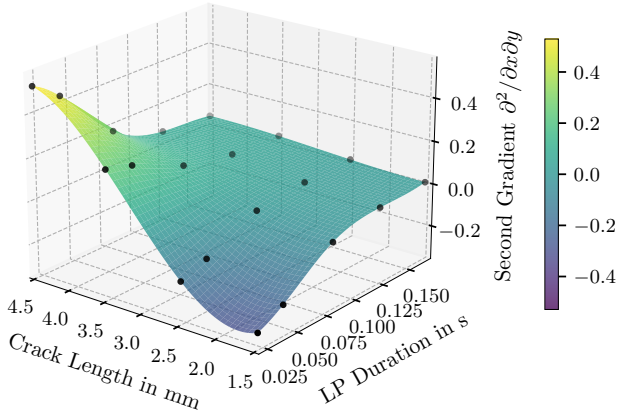

(b) Second gradient $\partial^2/\partial x \partial y$.

Figure 6.5: Influence of duration of the low-pressure (LP) phase and crack length on the SIF amplitude.

Figure 6.6 depicts the median of the absolute gradient of the estimated crack propagation rate da/dN for all parameters in the respective intervals. The gradients are normalized to 100%, corresponding to the duplication of the

crack propagation rate when duplicating this parameter's reference value. A value of 10% signifies that the crack propagation rates increased by ten percent when the reference value of this parameter was multiplied by two. The estimated crack propagation rates are calculated with the NASGRO equation, ignoring the stress intensity threshold and critical stress intensity. The main diagonal corresponds to the gradient along the parameter axis. The lower triangular matrix corresponds to the second gradient of the parameter combination. The lower triangular matrix is equivalent to the Hessian matrix of a seven-dimensional parameter space. A negative value indicates a reduced, and a positive value indicates an increased crack propagation rate.

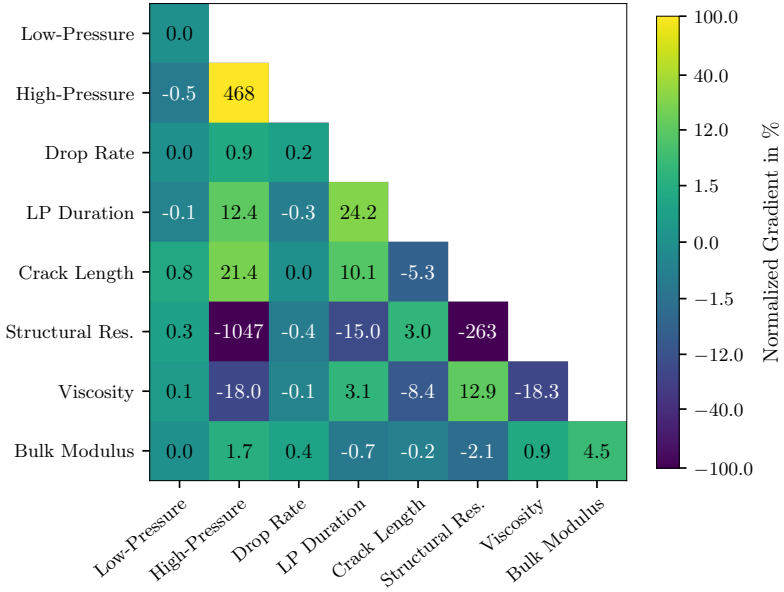

Figure 6.6: Heatmap of the median of the absolute gradients of the estimated crack propagation rate da/dN, normalized to 100% (main diagonal: gradient along primary parameter, lower triangular matrix: second gradient along primary and secondary parameter).

The gradients show that the structural resistance and the high-pressure level had the highest impact on the crack propagation. Due to the non-linearity

of the crack propagation law, the crack propagation rate increased up to 468%. The low-pressure level and the drop rate did not influence the crack propagation. The influence of the bulk modulus remained small, whereas the duration of the low-pressure phase, the viscosity, and the crack length had a more significant impact. While the pressure drop rate had no influence, the crack propagation rate increased with a longer lower-pressure phase as more oil flowed out. The viscosity had the opposite effect. A higher viscosity increased the flow resistance, and less oil flowed out of the crack. If the compressibility was decreased (higher bulk modulus), the pressure increased. Thus, the oil volume flow was higher.

Especially notable is that the low-pressure level had no significant influence. The increased low-pressure level did not alter the amount of fluid remaining inside the crack, and the crack opening displacement remained unaltered as long as the low-pressure level did not exceed a certain level. However, the pressure distribution visualized in Figure 6.7 inside the crack shows that the fluid pressure decreased contrary to the minimal stress. When the low-pressure level was higher, the oil did not need to exert the same force to maintain the crack opening displacement.

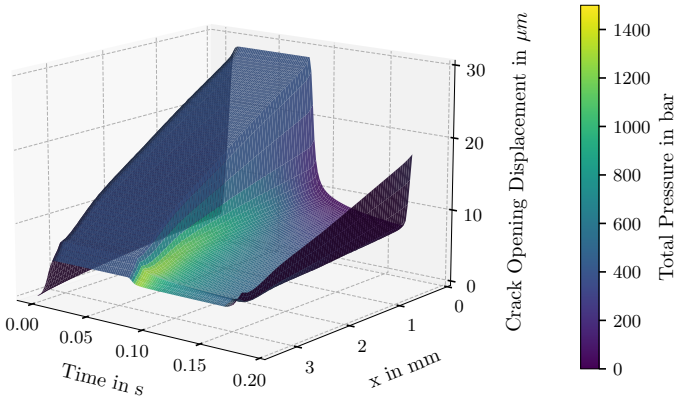

Figure 6.7: Fluid pressure distribution and crack opening displacement inside the crack over time during one pressure pulse with a low-pressure level of $p_{min} = 50\ bar$.

Particular parameter combinations lead to partially filled cracks. Partial-filled cracks occur when the load pressure drops before the oil fills the crack. This partial fill of the crack occurs, for example, with small crack openings or low-pressure build-up rates. In this case, evaporated gas is still inside the crack due to the cavitation during pressure build-up. Once the crack opening decreases, the pressure increases, and the phase transitions occur. The developed models can not simulate cavitation damage due to the implosion of cavitation bubbles. However, there are two arguments against pronounced cavitation damage: firstly, the low gap heights do not allow the formation of large cavitation bubbles. Secondly, the visual examinations of the crack faces did not reveal cavitation damage. In the case of partially filled cracks, however, further oil flowing into the crack tip during the pressure drop is possible, or at least no oil will flow out of the area of the crack tip. Hence, the crack opening in this area remained constant during the low-pressure phase. Figure 6.8 depicts the pressure curve of the simulated component for a pressure reduction rate of 5 $kbar/s$ and dynamic viscosity of $\eta = 0.1552\ Pa \cdot s$. The high viscosity provoked a partial-filled crack and a higher crack tip pressure.

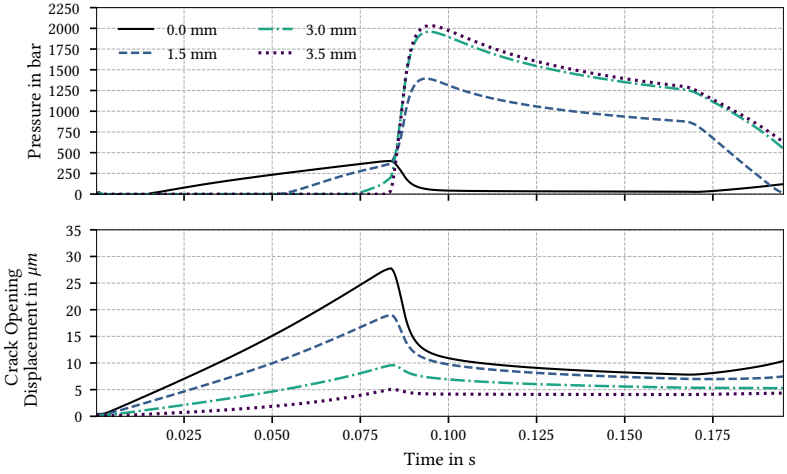

Figure 6.8: Fluid pressure and crack opening displacement at specific positions (x) of the crack in the case of a partially filled crack ($dp_{bu} = 5\ kbar/s$, $\eta = 0.1552\ Pa \cdot s$).

7 Summary

In this work, a simulation approach for the fluid-structure interaction in fatigue cracks of hydraulic components was developed. The approach simulates the influence of the fluid-structure interaction on the stress amplitude and the expected service life. It was demonstrated on a test specimen, and physical models were validated in experiments with this specimen.

A literature analysis of the influence of high-viscous fluids on crack growth has shown that two competing mechanisms are to be expected. On one side, the hydraulic pressure of the oil acts on the crack faces and increases the stress amplitude and the crack growth. On the other side, fluid-induced crack closure upholds the crack faces' displacement as the high-viscous fluid does not flow entirely. The uphold displacement reduces the stress amplitude and the crack propagation rate. So far, the impact of hydraulic pressure on crack propagation has been investigated with a focus on hydraulically forced fractures and external forces in the pitting of gear- and rail contacts. Fluid-structure interaction in fatigue cracks has not yet been investigated in the context of hydraulic components. In particular, high temporal pressure gradients are suspected to influence the fatigue crack propagation rate.

The simulation approach used reduced-order models for the fluid flow and the displacement of the crack faces. Reduced models improved the performance and numerical stability compared to a coupled finite-element and finite-volume simulation. The fluid flow inside the crack was represented by an adapted thin-film flow model, including flow factors to account for the surface roughness of the crack. The displacement of the crack faces was simulated by a yield strip model. The yield strip model divides the displacement into a linear-elastic and an ideal-plastic part. The linear-elastic displacement of the crack faces was approximated using weight functions. The component-specific deformation was simulated with a finite element analysis, from which the weight functions were derived. Based on the predicted elastic displacement, the ideal-plastic displacement was estimated using Irwin's model. The

models were discretized using the finite difference method and coupled to simulate the fluid-structure interaction. The model equations were formulated using a forward Euler formulation and numerically stabilized by an under-relaxation.

Pulsation tests were carried out with the developed test specimens to validate the simulation models. During the experiments, the test specimens' deformation was measured in the vicinity of the crack tip. The experiments showed that the fluid flow within the crack alters the dynamic system response of the part and that the dynamic system response is suitable for validating the physical models. After the crack growth inside the specimens reached the outer surface, the fluid flow through the crack was measured, and the flow factors were determined. First, the mechanical and fluid dynamical models were validated separately. In the second step, compliance simulations were used to determine the crack length of the components during the fatigue tests. As a consequence, the simulation results with a specific crack length could be compared to the dynamic system response of the part during the experiments.

The strain measurements during the fatigue tests validated that the simulation could reproduce the component's dynamics and that the reduced-order models correctly simulated the fluid-structure interaction in the crack. The influence of the fluid-structure interaction on the estimated fatigue damage was investigated using the test specimens as an example. Due to the fluid pressure on the crack faces, the expected service life of the components is reduced by approximately 39%. The fluid-induced crack closure has the opposite effect, which lowers the lifetime reduction in the investigated example to 19%. Six parameters that directly influence the damage amplitude were identified. The six parameters can be divided into the load pressure parameters (high-pressure level, duration of the low-pressure phase), the geometric parameters (crack length, structural resistance), and the fluid parameters (fluid viscosity, bulk modulus). Depending on the temporal gradient of the load pressure, the component service life can vary by more than 40%.

7.1 Scientific Contribution

In order to evaluate the scientific contribution, the research questions formulated in Section 2.4 are answered.

How does oil penetrate fatigue cracks in hydraulic components?

In Section 5.3, flow measurements on damaged components showed that oil flows through fatigue cracks, and the flow rate was quantified. Strain measurements during the fatigue tests in Section 5.2 indicated an oil flow into and out of cracks during the high- and low-pressure phase of pressure pulsations. Identically loaded specimens without a crack did not show the characteristic deformation due to the oil flow. The measured component strain was consistent with the expected component strain based on the simulated oil flow, and other known effects could be ruled out in Section 5.4.

How can the model complexity for FSI Simulations inside fatigue cracks be reduced?

In Chapter 4, a simulation approach with reduced-order model complexity was developed. The model complexity of the fluid model was reduced to a one-dimensional thin-film flow. The non-linear plastic deformation of the crack flanks was divided into two linear problems using a yield strip model. The linear models were combined into a forward Euler formulation by discretization with the finite difference method. The analysis of the dynamic system response during pressure pulses in Subsection 5.4.3 proved that the reduced-order models correctly simulated the oil flow inside the cracks and the displacement of the crack faces. The dynamic system response of the simulated specimen corresponded to the strain measured in the experiments.

How does the interaction of the oil with the mechanic structure influence the stress amplitude of fatigue cracks?

The fluid-structure interaction influences the stress amplitude and the crack propagation by two competing mechanisms. The fluid pressure provokes a force on the crack faces, increasing the crack opening displacement and the stress intensity at the crack tip. The increased stress intensity leads to a higher amplitude. Fluid-induced crack closure has the opposite effect. In the case of high-frequency pressure pulses, the oil remains in the crack, keeping the crack faces apart. Hence, the minimal stress intensity increases, and the amplitude is reduced.

Which load and design parameters influence the effective stress amplitude of fatigue cracks under cyclic loads?

In Section 6.3, three groups of parameters that could influence the effective stress amplitude in the crack were outlined. Of these, seven potential parameters were investigated in detail. The simulation results proved that five parameters significantly influence the stress amplitude and the expected crack propagation rate. In terms of load pressure, only the maximal pressure and the duration of the low-pressure phase influence the crack growth. In addition, the geometric parameters (crack length and structural resistance) and the fluid parameters (viscosity and compressibility) impact the crack propagation rate.
The frequency of the pulsation has no direct influence on the crack propagation rate. However, the frequency may influence the duration of the low-pressure phase. A shorter low-pressure phase reduces the amount of oil that leaves the crack and, therefore, the stress amplitude. The build-up and drop rates did not influence the fatigue stress as long as the high-pressure phase was sufficiently long to fill the crack entirely.
The crack advancement increases the influence of the fluid-structure interaction. For longer cracks, both the impact of hydrostatic pressure on the crack faces and fluid-induced crack closure become more significant.

Does the fluid-structure interaction inside fatigue cracks provoke a time delay between the pressure load and the mechanical deformation?

The oil flow in the crack leads to a characteristic delay in the deformation of the component. As analyzed in Subsection 5.4.3, at high drop rates, the delay is measurable and solely depends on the crack length. In particular, it is independent of the crack propagation rate. Therefore, this delay can be used to detect fatigue cracks and determine their length.

Due to the positive answers to the research questions, the research hypothesis

«*The interaction between a pressurized fluid and crack face influences the effective stress amplitude of fatigue cracks in hydraulic components.*»

can be confirmed.

Accounting for the fluid-structure interaction improves the estimation of the service life of hydraulic components. At the same time, testing a large number of configurations with little effort is possible with reduced-order

models. As a result, simulations of the component's lifetime can improve the development, leading to lighter and more efficient hydraulic components. As such, the presented approach contributes to scientific progress and makes an economic contribution.

7.2 Continuing Approaches

The simulation approach demonstrated that the fluid-structure interaction significantly impacts the effective stress amplitude and, thus, the expected crack growth. However, the experimental crack growth is subject to high fluctuations, and the current crack growth laws are not sufficient to predict the crack growth precisely. Metallurgical investigations are required to improve the prediction of the crack propagation rate, e.g., by incorporating the temperature. In this context, the simulation models can be extended by an improved estimation of the plastic zone and by incorporating effects such as cyclic plasticity.

The work has adopted the averaged Reynolds equation from tribology for fatigue cracks. It was demonstrated that the flow factors are able to correct the volume flow to account for the surface roughness inside the crack. However, only one geometry and one material were investigated. The influence of the material and the geometry on the flow factors has yet to be investigated. It remains unknown whether a universal law for flow factors in fatigue cracks can be formulated or to what extent these have to be determined anew for each material and geometry. Several approaches to simulate flow factors have been developed in tribological investigations, but further studies still need to investigate if they can be transferred to fatigue cracks. Investigations with hydraulic pressure amplifiers would permit the flow factors to be measured at higher pressures and to validate whether the assumption of a quadratic progression holds true for large cracks.

The use of reduced-order models brings performance advantages but limits the flexibility of the simulation. For the investigation of the FSI, a simple geometry was chosen, which allowed a clear separation of the individual influences. However, for a commercial application, especially in view of the increasing computational performance of simulation servers, integration of the fluid model into a three-dimensional structural simulation, such as the extended finite element method, is recommended. A coupled extended FEM would permit the simulation of complex and unknown geometries without additional modeling effort.

A Appendix

A.1 Figures

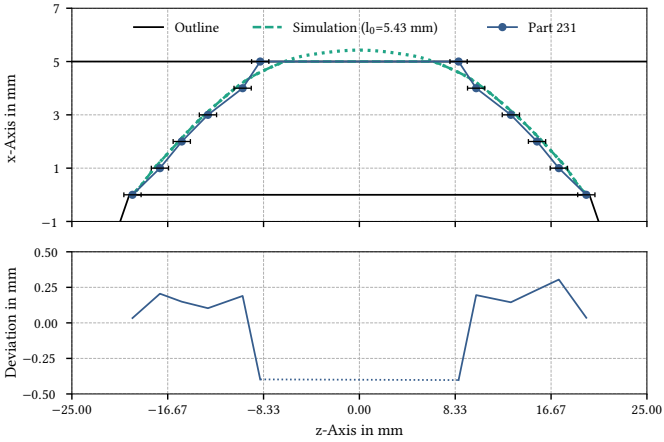

Figure A.1: Crack front measurement and deviation of the crack front approximation for part 231.

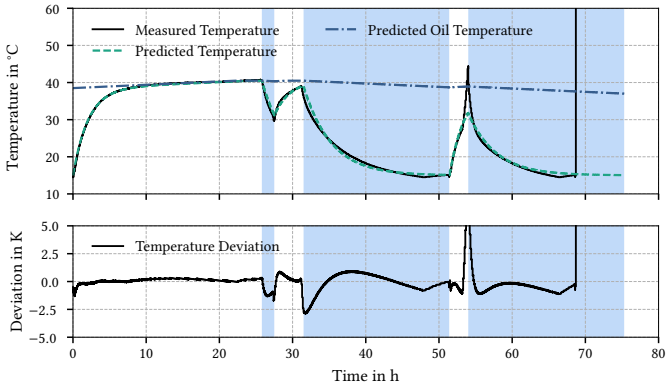

Figure A.2: Measured specimen temperature, approximated specimen temperature, and approximated oil temperature for part 242. Idle times at $t = [25.8, 31.5]\ h$.

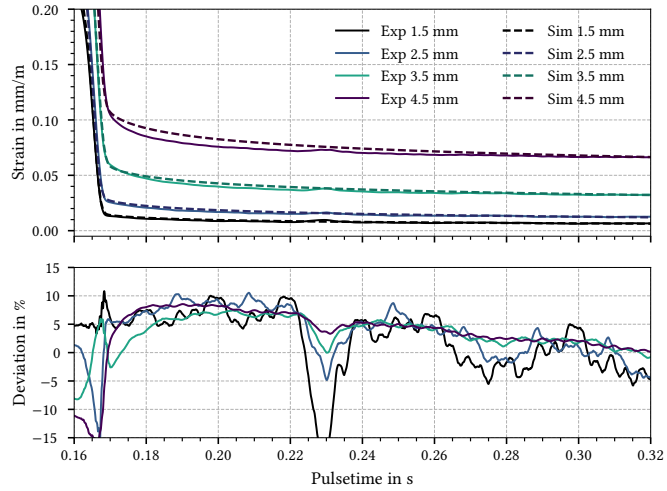

Figure A.3: Measured strain of part 210 (3 Hz, 80 $kbar/s$) compared to the FSI simulation results for crack lengths of $l_0 \in [1.5, 2.5, 3.5, 4.5]\ mm$.

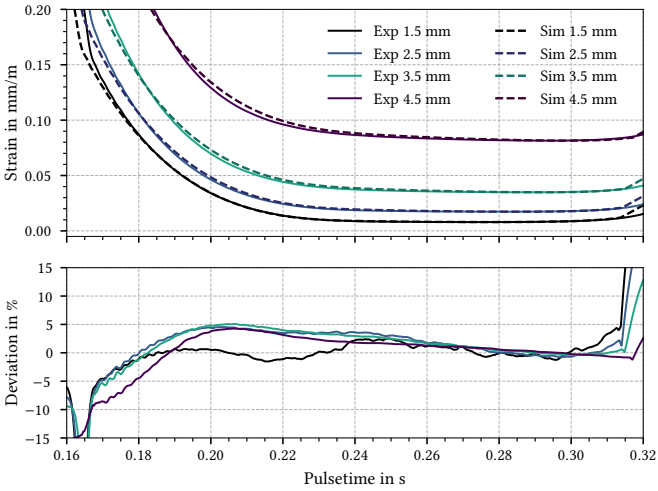

Figure A.4: Measured strain of part 220 (3 Hz, 10 $kbar/s$) compared to the FSI simulation results for crack lengths of $l_0 \in [1.5, 2.5, 3.5, 4.5]$ mm.

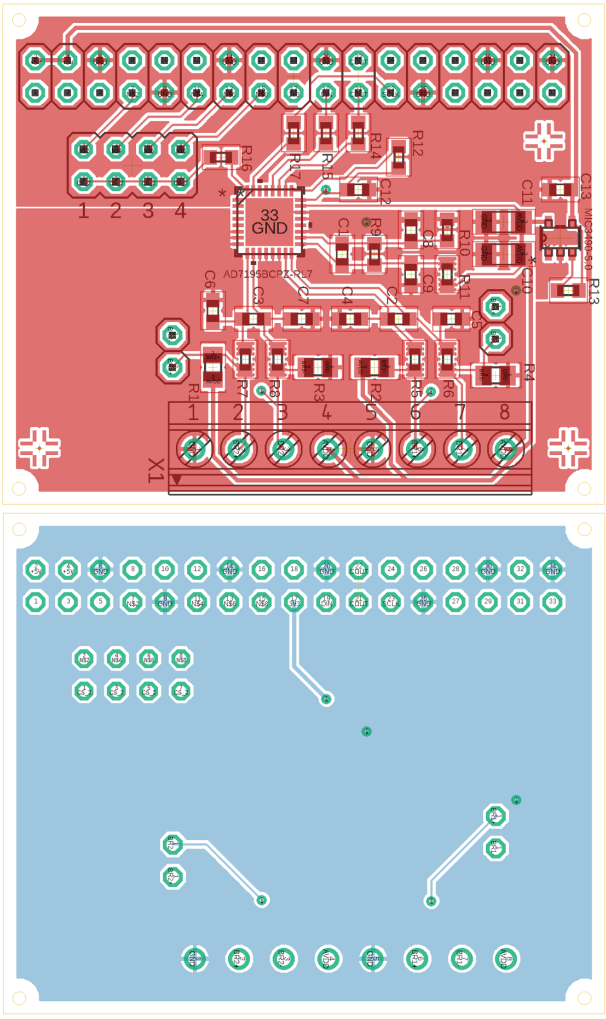

Figure A.5: PCB Layout of the AD Converter Circuit integrating the AD7195.

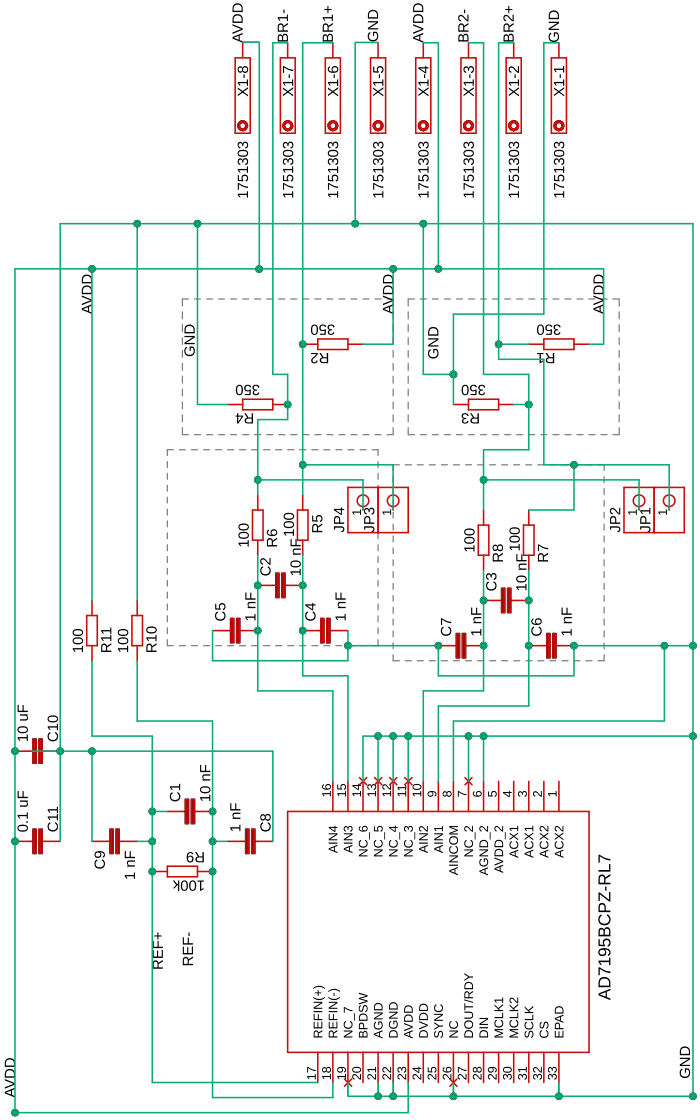

Figure A.6: Circuit Diagram of the AD Converter Circuit integrating the AD7195, the voltage supply is omitted.

A.2 Tables

Table A.1: Material properties

Parameter	Unit	Value
High-Pressure Level	bar	400
Low-Pressure Level	bar	5
Build-Up Rate	$kbar/s$	40
Drop Rate	$kbar/s$	80
Dynamic Viscosity	Pas	0.0388
Base Oil Density	kg/m^3	800
Bulk Modulus	GPa	1
Young's Modulus	210	GPa
Poisson's Ratio	0.3	-
Yield Strength	235	MPa

Table A.2: Simulation parameters

Parameter	Unit	Value
Element Size	μm	50
Step Size	ns	20
Under Relaxation Factor	–	0.01
Numeric COD Threshold	μm	0.1
Flow Factor Approximation	–	quadratic

Table A.3: NASGRO material constants

Parameter	Unit	Value
C_{FM}	$mm/(MPa\sqrt{(mm)})^n$	0.605e-12
n	–	2.8
p	–	0.5
q	–	0.5
$\Delta K_{I,th}$	$MPa\sqrt{(mm)}$	243
ΔK_{IC}	$MPa\sqrt{(mm)}$	2432
α	–	2
SR	–	0.3

Table A.4: Crack widths measured by dye penetration at $x = 5\ mm$ and estimated characteristic crack lengths.

Part	Optical Resolution in px/mm	Path Length in mm	Projected Width in mm	Characteristic Crack Length in mm
210	58	19.3	16.3	5.47
212	68	17.4	17.4	5.55
220	38	16.9	15.9	5.56
220	107	16.9	16.1	5.46
231	36	17.2	16.6	5.43
233	116	19.3	18.4	5.70
240	82	18.6	16.5	5.49
242	70	20.1	20.1	5.97

List of Figures

List of Tables

Bibliography

[1] E. Santecchia *et al.*, "A Review on Fatigue Life Prediction Methods for Metals", *Advances in Materials Science and Engineering*, vol. 2016, e9573524, Sep. 27, 2016, ISSN: 1687-8434. DOI: 10.1155/2016/9573524.

[2] M. Ciavarella, P. D'antuono, and A. Papangelo, "On the connection between Palmgren-Miner rule and crack propagation laws", *Fatigue & Fracture of Engineering Materials & Structures*, vol. 41, no. 7, pp. 1469–1475, Jul. 2018, ISSN: 8756-758X, 1460-2695. DOI: 10.1111/ffe.12789.

[3] F. H. Davis, E. G. Ellison, and W. J. Plumbridge, "Effects of Hydrostatic Pressure on the Rate of Fatigue Crack Growth", *Fatigue & Fracture of Engineering Materials & Structures*, vol. 12, no. 6, pp. 511–525, 1989, ISSN: 1460-2695. DOI: 10.1111/j.1460-2695.1989.tb00560.x.

[4] F. H. Davis and E. G. Ellison, "Hydrodynamic Pressure Effects of Viscous Fluid Flow in a Fatigue Crack", *Fatigue & Fracture of Engineering Materials & Structures*, vol. 12, no. 6, pp. 527–542, 1989, ISSN: 1460-2695. DOI: 10.1111/j.1460-2695.1989.tb00561.x.

[5] S. Jian, L. Xin, and W. Shaoping, "Dynamic Pressure Gradient Model of Axial Piston Pump and Parameters Optimization", *Mathematical Problems in Engineering*, vol. 2014, pp. 1–10, 2014, ISSN: 1024-123X, 1563-5147. DOI: 10.1155/2014/352981.

[6] L. Brinkschulte, "Assistenzsysteme zur Reduktion des Schädigungsverhaltens von Komponenten einer mobilen Arbeitsmaschine", Dissertation, Karlsruhe Institute of Technology (Karlsruher Schriftenreihe Fahrzeugsystemtechnik). Karlsruhe, 2021, vol. 90, 219 pp., ISBN: 978-3-7315-1089-5. DOI: 10.5445/KSP/1000130176.

[7] B. Pyttel, D. Schwerdt, and C. Berger, "Very high cycle fatigue – Is there a fatigue limit?", *International Journal of Fatigue*, Advances in Very High Cycle Fatigue, vol. 33, no. 1, pp. 49–58, Jan. 1, 2011, ISSN: 0142-1123. DOI: 10.1016/j.ijfatigue.2010.05.009.

[8] Q. Wang, M. K. Khan, and C. Bathias, "Current understanding of ultra-high cycle fatigue", *Theoretical and Applied Mechanics Letters*, vol. 2, no. 3, p. 031 002, Jan. 1, 2012, ISSN: 2095-0349. DOI: 10.1063/2.1203102.

[9] H. Mughrabi, "Damage Mechanisms and Fatigue Lives: From the Low to the Very High Cycle Regime", *6th International Conference on Creep, Fatigue and Creep-Fatigue Interaction*, vol. 55, pp. 636–644, Jan. 1, 2013, ISSN: 1877-7058. DOI: 10.1016/j.proeng.2013.03.307.

[10] D. Broek, *Elementary Engineering Fracture Mechanics*. Dordrecht: Springer Netherlands, 1982, ISBN: 978-94-010-8425-3. DOI: 10.1007/978-94-009-4333-9.

[11] H. A. Richard, *Fracture Predictions for Cracks Exposed to Superimposed Normal and Shear Stresses* (VDI-Forschungsheft 631). Duesseldorf (Germany): VDI-Verl, 1985, 60 pp., ISBN: 3-18-85 0631-7.

[12] H. A. Richard and M. Sander, *Fatigue Crack Growth* (Solid Mechanics and Its Applications). Cham: Springer International Publishing, 2016, vol. 227, ISBN: 978-3-319-32532-3. DOI: 10.1007/978-3-319-32534-7.

[13] H. A. Richard and M. Sander, *Fatigue Crack Growth* (Solid Mechanics and Its Applications). Cham: Springer International Publishing, 2016, vol. 227, Reproduced with permission from Springer Nature, ISBN: 978-3-319-32532-3. DOI: 10.1007/978-3-319-32534-7.

[14] J. W. Ringsberg and A. Bergkvist, "On propagation of short rolling contact fatigue cracks", *Fatigue & Fracture of Engineering Materials & Structures*, vol. 26, no. 10, pp. 969–983, 2003, ISSN: 1460-2695. DOI: 10.1046/j.1460-2695.2003.00657.x.

[15] K. Farhangdoost and M. Kavoosi, "Effect of Lubricant on Surface Rolling Contact Fatigue Cracks", *Advanced Materials Research*, vol. 97–101, pp. 793–796, 2010, ISSN: 1662-8985. DOI: 10.4028/www.scientific.net/AMR.97-101.793.

[16] T. Fett, *Stress Intensity Factors - T-Stresses - Weight Functions* (Schriftenreihe Des Instituts Für Keramik Im Maschinenbau - IKM). Karlsruhe: Universitätsverlag Karlsruhe (KIT), 2008, vol. 50, 362 pp., ISBN: 9783866442351. DOI: 10.5445/KSP/1000007996.

[17] Y. Murakami, *Stress Intensity Factors Handbook*. University of Michigan: Pergamon, 1987, ISBN: 978-0-08-034809-4.

[18] T. Fett and G. Rizzi, "Weight Functions for Stress Intensity Factors and T-Stress for Oblique Cracks in A Half-Space", *International journal of fracture*, vol. 132, no. 1, pp. L9–L16, 2005, ISSN: 0376-9429. DOI: 10.1007/s10704-005-0024-9.

[19] H. P. Rossmanith, *Finite Elemente in Der Bruchmechanik*. Vienna: Springer Vienna, 2013, ISBN: 978-3-7091-2297-6.

[20] S. R. McNeill, W. H. Peters, and M. A. Sutton, "Estimation of stress intensity factor by digital image correlation", *Engineering Fracture Mechanics*, vol. 28, no. 1, pp. 101–112, Jan. 1, 1987, ISSN: 0013-7944. DOI: 10.1016/0013-7944(87)90124-X.

[21] D. P. Rooke, F. I. Baratta, and D. J. Cartwright, "Simple methods of determining stress intensity factors", *Engineering Fracture Mechanics*, vol. 14, no. 2, pp. 397–426, Jan. 1, 1981, ISSN: 0013-7944. DOI: 10.1016/0013-7944(81)90010-2.

[22] H.-J. Schindler, W. Cheng, and I. Finnie, "Experimental determination of stress intensity factors due to residual stresses", *Experimental Mechanics*, vol. 37, no. 3, pp. 272–277, Sep. 1, 1997, ISSN: 1741-2765. DOI: 10.1007/BF02317418.

[23] Q. Han *et al.*, "Determination of stress intensity factor for mode I fatigue crack based on finite element analysis", *Engineering Fracture Mechanics*, vol. 138, pp. 118–126, Apr. 1, 2015, ISSN: 0013-7944. DOI: 10.1016/j.engfracmech.2015.02.019.

[24] M. Besel and E. Breitbarth, "Advanced analysis of crack tip plastic zone under cyclic loading", *International Journal of Fatigue*, vol. 93, pp. 92–108, Dec. 1, 2016, ISSN: 0142-1123. DOI: 10.1016/j.ijfatigue.2016.08.013.

[25] M. W. Brown, E. R. de los Rios, and K. J. Miller, "A Critical Comparison of Proposed Parameters for High-Strain Fatigue Crack Growth", in *Basic Questions in Fatigue: Volume I*, ASTM International, Jan. 1, 1988, pp. 233–259. DOI: 10.1520/STP23219S.

[26] Y. Du, A. Patki, and E. Patterson, "Monitoring Crack Tip Plastic Zone Size During Fatigue Loading", in *Experimental and Applied Mechanics, Volume 6*, T. Proulx, Ed., ser. Conference Proceedings of the Society for Experimental Mechanics Series, New York, NY: Springer, 2011, pp. 569–573, ISBN: 978-1-4419-9792-0. DOI: 10.1007/978-1-4419-9792-0_83.

[27] Y. J. Jia *et al.*, "A Better Estimation of Plastic Zone Size at the Crack Tip Beyond Irwin's Model", *Journal of Applied Mechanics*, vol. 80, no. 5, Jul. 18, 2013, ISSN: 0021-8936. DOI: 10.1115/1.4023642.

[28] G. R. Irwin, "Plastic zone near a crack and fracture toughness", in *Proceedings of the 7th Sagamore Ordnance Materials Research Conference*, Racquette Lake, NY, Aug. 16–19, 1960, pp. 63–78.

[29] S. K. Paul and S. Tarafder, "Cyclic plastic deformation response at fatigue crack tips", *International Journal of Pressure Vessels and Piping*, vol. 101, pp. 81–90, Jan. 1, 2013, ISSN: 0308-0161. DOI: 10.1016/j.ijpvp.2012.10.007.

[30] P. Paris and F. Erdogan, "A Critical Analysis of Crack Propagation Laws", *Journal of Basic Engineering*, vol. 85, no. 4, pp. 528–533, Dec. 1, 1963, ISSN: 0021-9223. DOI: 10.1115/1.3656900.

[31] R. G. Forman and S. R. Mettu, "Behavior of surface and corner cracks subjected to tensile and bending loads in Ti-6Al-4V alloy", NASA Technical Reports, Technical Memorandum (TM) S-611, Sep. 1, 1990.

[32] Y. Li, H. Wang, and D. Gong, "The interrelation of the parameters in the Paris equation of fatigue crack growth", *Engineering Fracture Mechanics*, vol. 96, pp. 500–509, Dec. 1, 2012, ISSN: 0013-7944. DOI: 10.1016/j.engfracmech.2012.08.016.

[33] N. Pugno *et al.*, "A generalized Paris' law for fatigue crack growth", *Journal of the Mechanics and Physics of Solids*, vol. 54, no. 7, pp. 1333–1349, Jul. 1, 2006, ISSN: 0022-5096. DOI: 10.1016/j.jmps.2006.01.007.

[34] J. Maierhofer, R. Pippan, and H.-P. Gänser, "Modified NASGRO equation for physically short cracks", *International Journal of Fatigue*, vol. 59, pp. 200–207, Feb. 1, 2014, ISSN: 0142-1123. DOI: 10.1016/j.ijfatigue.2013.08.019.

[35] K. S. Chan, "Roles of microstructure in fatigue crack initiation", *International Journal of Fatigue*, Emerging Frontiers in Fatigue, vol. 32, no. 9, pp. 1428–1447, Sep. 1, 2010, ISSN: 0142-1123. DOI: 10.1016/j.ijfatigue.2009.10.005.

[36] M. D. Sangid, "The physics of fatigue crack initiation", *International Journal of Fatigue*, Fatigue and Microstructure: A Special Issue on Recent Advances, vol. 57, pp. 58–72, Dec. 1, 2013, ISSN: 0142-1123. DOI: 10.1016/j.ijfatigue.2012.10.009.

[37] J. Payne *et al.*, "Observations of fatigue crack initiation in 7075-T651", *International Journal of Fatigue*, vol. 32, no. 2, pp. 247–255, Feb. 1, 2010, ISSN: 0142-1123. DOI: 10.1016/j.ijfatigue.2009.06.003.

[38] W. Elber, "Fatigue crack closure under cyclic tension", *Engineering Fracture Mechanics*, vol. 2, no. 1, pp. 37–45, Jul. 1, 1970, ISSN: 0013-7944. DOI: 10.1016/0013-7944(70)90028-7.

[39] W. Elber, "The Significance of Fatigue Crack Closure", in *Damage Tolerance in Aircraft Structures*, ASTM International, 1971, pp. 230–242. DOI: 10.1520/STP26680S.

[40] L. P. Borrego, J. M. Ferreira, and J. M. Costa, "Fatigue crack growth and crack closure in an AlMgSi alloy", *Fatigue & Fracture of Engineering Materials & Structures*, vol. 24, no. 4, pp. 255–265, 2001, ISSN: 1460-2695. DOI: 10.1046/j.1460-2695.2001.00383.x.

[41] R. Pippan and A. Hohenwarter, "Fatigue crack closure: A review of the physical phenomena", *Fatigue & Fracture of Engineering Materials & Structures*, vol. 40, no. 4, pp. 471–495, 2017, ISSN: 1460-2695. DOI: 10.1111/ffe.12578.

[42] A. K. Vasudeven, K. Sadananda, and N. Louat, "A review of crack closure, fatigue crack threshold and related phenomena", *Materials Science and Engineering: A*, vol. 188, no. 1, pp. 1–22, Nov. 30, 1994, ISSN: 0921-5093. DOI: 10.1016/0921-5093(94)90351-4.

[43] B. C. Sheu, P. S. Song, and C. S. Shin, "The effect of infiltration induced crack closure on crack growth retardation", *Scripta Metallurgica et Materialia; (United States)*, vol. 31:10, Nov. 15, 1994, ISSN: 0956-716X. DOI: 10.1016/0956-716X(94)90107-4.

[44] K. Solanki, S. R. Daniewicz, and J. C. Newman, "Finite element analysis of plasticity-induced fatigue crack closure: An overview", *Engineering Fracture Mechanics*, vol. 71, no. 2, pp. 149–171, Jan. 1, 2004, ISSN: 0013-7944. DOI: 10.1016/S0013-7944(03)00099-7.

[45] S. K. Ray and A. F. Grandt, "Comparison of Methods for Measuring Fatigue Crack Closure in a Thick Specimen", in *Mechanics of Fatigue Crack Closure*, ASTM International, Jan. 1, 1988, pp. 197–213. DOI: 10.1520/STP27209S.

[46] Y. Xu, P. J. Gregson, and I. Sinclair, "Systematic assessment and validation of compliance-based crack closure measurements in fatigue", *Materials Science and Engineering: A*, vol. 284, no. 1, pp. 114–125, May 31, 2000, ISSN: 0921-5093. DOI: 10.1016/S0921-5093(00)00758-9.

[47] L. Patriarca, S. Foletti, and S. Beretta, "A comparison of DIC-based techniques to measure crack closure in LCF", *Theoretical and Applied Fracture Mechanics*, vol. 98, pp. 230–243, Dec. 1, 2018, ISSN: 0167-8442. DOI: 10.1016/j.tafmec.2018.09.020.

[48] K.-J. Bathe, "Finite Element Method", in *Wiley Encyclopedia of Computer Science and Engineering*, John Wiley & Sons, Ltd, 2008, pp. 1–12, ISBN: 978-0-470-05011-8. DOI: 10.1002/9780470050118.ecse159.

[49] A. E. Tekkaya and P. A. F. Martins, "Accuracy, reliability and validity of finite element analysis in metal forming: A user's perspective", *Engineering Computations*, vol. 26, no. 8, pp. 1026–1055, Jan. 1, 2009, ISSN: 0264-4401. DOI: 10.1108/02644400910996880.

[50] G. Warren and W. Scott, "Numerical dispersion of higher order nodal elements in the finite-element method", *IEEE Transactions on Antennas and Propagation*, vol. 44, no. 3, pp. 317–320, Mar. 1996, ISSN: 1558-2221. DOI: 10.1109/8.486299.

[51] D. Weida *et al.*, "Benefits of higher order elements for electrostatic simulations of large-scale 3D insulator structures", in *2009 IEEE Electrical Insulation Conference*, May 2009, pp. 558–561. DOI: 10.1109/EIC.2009.5166408.

[52] D. S. Dugdale, "Yielding of steel sheets containing slits", *Journal of the Mechanics and Physics of Solids*, vol. 8, no. 2, pp. 100–104, May 1, 1960, ISSN: 0022-5096. DOI: 10.1016/0022-5096(60)90013-2.

[53] G. S. Wang and A. F. Blom, "A strip model for fatigue crack growth predictions under general load conditions", *Engineering Fracture Mechanics*, vol. 40, no. 3, pp. 507–533, Jan. 1, 1991, ISSN: 0013-7944. DOI: 10.1016/0013-7944(91)90148-T.

[54] S. Östlund, "Large scale yielding for dynamic crack growth in a strip geometry", *International Journal of Fracture*, vol. 49, no. 3, pp. 219–237, Jun. 1, 1991, ISSN: 1573-2673. DOI: 10.1007/BF00035043.

[55] S. Beretta and M. Carboni, "A Strip-Yield algorithm for the analysis of closure evaluation near the crack tip", *Engineering Fracture Mechanics*, vol. 72, no. 8, pp. 1222–1237, May 1, 2005, ISSN: 0013-7944. DOI: 10.1016/j.engfracmech.2004.10.003.

[56] C. Fischer, C. Schweizer, and T. Seifert, "Assessment of fatigue crack closure under in-phase and out-of-phase thermomechanical fatigue loading using a temperature dependent strip yield model", *International Journal of Fatigue*, vol. 78, pp. 22–30, Sep. 1, 2015, ISSN: 0142-1123. DOI: 10.1016/j.ijfatigue.2015.03.022.

[57] S. R. Daniewicz and C. R. Aveline, "Strip-yield and finite element analysis of part-through surface flaws", *Engineering Fracture Mechanics*, vol. 67, no. 1, pp. 21–39, Sep. 1, 2000, ISSN: 0013-7944. DOI: 10.1016/S0013-7944(00)00032-1.

[58] S. Beretta, M. Carboni, and M. Madia, "Modelling of fatigue thresholds for small cracks in a mild steel by "Strip-Yield" model", *Engineering Fracture Mechanics*, MatModels 2007, vol. 76, no. 10, pp. 1548–1561, Jul. 1, 2009, ISSN: 0013-7944. DOI: 10.1016/j.engfracmech.2009.04.015.

[59] J. H. Ferziger, M. Perić, and R. L. Street, *Computational Methods for Fluid Dynamics*. Cham: Springer International Publishing, 2020, ISBN: 978-3-319-99691-2 978-3-319-99693-6. DOI: 10.1007/978-3-319-99693-6.

[60] H. Oertel, M. Böhle, and U. Dohrmann, *Stroemungsmechanik*. Wiesbaden: Vieweg+Teubner, 2009, ISBN: 978-3-8348-0483-9 978-3-8348-9248-5. DOI: 10.1007/978-3-8348-9248-5.

[61] C. Pozrikidis, *Fluid Dynamics : Theory, Computation, and Numerical Simulation* (Springer eBook Collection), 3rd ed. New York, NY: Springer Link, 2017, ISBN: 978-1-4899-7991-9.

[62] O. Reynolds, "IV. On the theory of lubrication and its application to Mr. Beauchamp tower's experiments, including an experimental determination of the viscosity of olive oil", *Philosophical Transactions of the Royal Society of London*, vol. 177, pp. 157–234, 1886. DOI: 10.1098/rstl.1886.0005.

[63] A. Z. Szeri, *Fluid Film Lubrication*, 2nd ed. Cambridge: Cambridge University Press, 2010, ISBN: 978-0-511-98883-7.

[64] C. Kleinstreuer, *Engineering Fluid Dynamics: An Interdisciplinary Systems Approach*. Cambridge: Cambridge University Press, 1997. DOI: 10.1017/CBO9781139174510.

[65] P. W. Gold *et al.*, "Viscosity–pressure–temperature behaviour of mineral and synthetic oils", *Journal of Synthetic Lubrication*, vol. 18, no. 1, pp. 51–79, Apr. 2001, ISSN: 0265-6582, 1557-6841. DOI: 10.1002/jsl.3000180105.

[66] X. Paredes *et al.*, "High pressure viscosity characterization of four vegetable and mineral hydraulic oils", *Industrial Crops and Products*, vol. 54, pp. 281–290, Mar. 1, 2014, ISSN: 0926-6690. DOI: 10.1016/j.indcrop.2014.01.030.

[67] N. Patir and H. S. Cheng, "An Average Flow Model for Determining Effects of Three-Dimensional Roughness on Partial Hydrodynamic Lubrication", *Journal of Lubrication Technology*, vol. 100, no. 1, pp. 12–17, Jan. 1, 1978, ISSN: 0022-2305. DOI: 10.1115/1.3453103.

[68] N. Patir and H. S. Cheng, "Application of Average Flow Model to Lubrication Between Rough Sliding Surfaces", *Journal of Lubrication Technology*, vol. 101, no. 2, pp. 220–229, Apr. 1, 1979, ISSN: 0022-2305. DOI: 10.1115/1.3453329.

[69] D. Bartel, *Simulation von Tribosystemen*. Wiesbaden: Vieweg+Teubner, 2010, ISBN: 978-3-8348-1241-4 978-3-8348-9656-8. DOI: 10.1007/978-3-8348-9656-8.

[70] J. L. Teale and A. O. Lebeck, "An Evaluation of the Average Flow Model for Surface Roughness Effects in Lubrication", *Journal of Lubrication Technology*, vol. 102, no. 3, pp. 360–366, Jul. 1, 1980, ISSN: 0022-2305. DOI: 10.1115/1.3251544.

[71] S. R. Harp and R. F. Salant, "An Average Flow Model of Rough Surface Lubrication With Inter-Asperity Cavitation", *Journal of Tribology*, vol. 123, no. 1, pp. 134–143, Oct. 17, 2000, ISSN: 0742-4787. DOI: 10.1115/1.1332397.

[72] N. Bauer *et al.*, "Elastohydrodynamic Simulation of Pneumatic Sealing Friction Considering 3D Surface Topography", *Chemical Engineering & Technology*, vol. 46, no. 1, pp. 167–174, Jan. 2023, ISSN: 0930-7516, 1521-4125. DOI: 10.1002/ceat.202200471.

[73] C. R. Maliska, *Fundamentals of Computational Fluid Dynamics: The Finite Volume Method* (Fluid Mechanics and Its Applications). Cham: Springer International Publishing, 2023, vol. 135, ISBN: 978-3-031-18234-1 978-3-031-18235-8. DOI: 10.1007/978-3-031-18235-8.

[74] R. Kamakoti and W. Shyy, "Fluid–structure interaction for aeroelastic applications", *Progress in Aerospace Sciences*, vol. 40, no. 8, pp. 535–558, Nov. 1, 2004, ISSN: 0376-0421. DOI: 10.1016/j.paerosci.2005.01.001.

[75] G. Hou, J. Wang, and A. Layton, "Numerical Methods for Fluid-Structure Interaction — A Review", *Communications in Computational Physics*, vol. 12, no. 2, pp. 337–377, Aug. 2012, ISSN: 1815-2406, 1991-7120. DOI: 10.4208/cicp.291210.290411s.

[76] F. Duarte, R. Gormaz, and S. Natesan, "Arbitrary Lagrangian–Eulerian method for Navier–Stokes equations with moving boundaries", *Computer Methods in Applied Mechanics and Engineering*, vol. 193, no. 45, pp. 4819–4836, Nov. 12, 2004, ISSN: 0045-7825. DOI: 10.1016/j.cma.2004.05.003.

[77] A. Gerstenberger and W. A. Wall, "Enhancement of fixed-grid methods towards complex fluid–structure interaction applications", *International Journal for Numerical Methods in Fluids*, vol. 57, no. 9, pp. 1227–1248, 2008, ISSN: 1097-0363. DOI: 10.1002/fld.1782.

[78] C. S. Peskin, "The immersed boundary method", *Acta Numerica*, vol. 11, pp. 479–517, Jan. 2002, ISSN: 1474-0508, 0962-4929. DOI: 10.1017/S0962492902000077.

[79] X. Wang and W. K. Liu, "Extended immersed boundary method using FEM and RKPM", *Computer Methods in Applied Mechanics and Engineering*, Meshfree Methods: Recent Advances and New Applications, vol. 193, no. 12, pp. 1305–1321, Mar. 26, 2004, ISSN: 0045-7825. DOI: 10.1016/j.cma.2003.12.024.

[80] A. Legay, J. Chessa, and T. Belytschko, "An Eulerian–Lagrangian method for fluid–structure interaction based on level sets", *Computer Methods in Applied Mechanics and Engineering*, Fluid-Structure Interaction, vol. 195, no. 17, pp. 2070–2087, Mar. 15, 2006, ISSN: 0045-7825. DOI: 10.1016/j.cma.2005.02.025.

[81] T.-P. Fries and T. Belytschko, "The extended/generalized finite element method: An overview of the method and its applications", *International Journal for Numerical Methods in Engineering*, vol. 84, no. 3, pp. 253–304, 2010, ISSN: 1097-0207. DOI: 10.1002/nme.2914.

[82] K. Rege and H. G. Lemu, "A review of fatigue crack propagation modelling techniques using FEM and XFEM", *IOP Conference Series: Materials Science and Engineering*, vol. 276, no. 1, p. 012 027, Dec. 2017, ISSN: 1757-899X. DOI: 10.1088/1757-899X/276/1/012027.

[83] E. Gordeliy and A. Peirce, "Coupling schemes for modeling hydraulic fracture propagation using the XFEM", *Computer Methods in Applied Mechanics and Engineering*, vol. 253, pp. 305–322, Jan. 1, 2013, ISSN: 0045-7825. DOI: 10.1016/j.cma.2012.08.017.

[84] H. Y. Wang, "Numerical modeling of non-planar hydraulic fracture propagation in brittle and ductile rocks using XFEM with cohesive zone method", *Journal of Petroleum Science and Engineering*, vol. 135, pp. 127–140, Nov. 1, 2015, ISSN: 0920-4105. DOI: 10.1016/j.petrol.2015.08.010.

[85] C. J. Polk, W. R. Murphy, and C. N. Rowe, "Determining Fatigue Crack Propagation Rates in Lubricating Environments through the Application of a Fracture Mechanics Technique", *A S L E Transactions*, vol. 18, no. 4, pp. 290–298, Jan. 1, 1975, ISSN: 0569-8197. DOI: 10.1080/05698197508982771.

[86] J.-L. Tzou, S. Suresh, and R. Ritchie, "Fatigue crack propagation in viscous environments", in *Mechanical Behaviour of Materials*, J. CARLSSON and N. OHLSON, Eds., Pergamon, Jan. 1, 1984, pp. 711–717, ISBN: 978-1-4832-8372-2. DOI: 10.1016/B978-1-4832-8372-2.50090-7.

[87] J.-L. Tzou *et al.*, "Fatigue crack propagation in oil environments— II. A model for crack closure induced by viscous fluids", *Acta Metallurgica*, vol. 33, no. 1, pp. 117–127, Jan. 1, 1985, ISSN: 0001-6160. DOI: 10.1016/0001-6160(85)90225-1.

[88] W. J. Plumbridge, P. J. Ross, and J. S. C. Parry, "Fatigue crack growth in liquids under pressure", *Materials Science and Engineering*, vol. 68, no. 2, pp. 219–232, Jan. 1, 1985, ISSN: 0025-5416. DOI: 10.1016/0025-5416(85)90411-2.

[89] O. P. Datsyshyn and V. V. Panasyuk, "Pitting of the rolling bodies contact surface", *Wear*, 13th International Conference on Wear of Materials, vol. 251, no. 1, pp. 1347–1355, Oct. 1, 2001, ISSN: 0043-1648. DOI: 10.1016/S0043-1648(01)00771-2.

[90] D. I. Fletcher, P. Hyde, and A. Kapoor, "Investigating fluid penetration of rolling contact fatigue cracks in rails using a newly developed full-scale test facility", *Proceedings of the Institution of Mechanical Engineers, Part F: Journal of Rail and Rapid Transit*, vol. 221, no. 1, pp. 35–44, Jan. 1, 2007, ISSN: 0954-4097. DOI: 10.1243/09544097JRRT63.

[91] M. Akama and T. Mori, "Boundary Element Analysis of Effects of Crack Face Friction and Trapped Fluid on Rolling Contact Fatigue Cracks", *Quarterly Report of RTRI*, vol. 46, no. 4, pp. 231–237, 2005, ISSN: 0033-9008, 1880-1765. DOI: 10.2219/rtriqr.46.231.

[92] P. E. Bold, M. W. Brown, and R. J. Allen, "Shear mode crack growth and rolling contact fatigue", *Wear*, vol. 144, no. 1, pp. 307–317, Apr. 20, 1991, ISSN: 0043-1648. DOI: 10.1016/0043-1648(91)90022-M.

[93] A. F. Bower, "The Influence of Crack Face Friction and Trapped Fluid on Surface Initiated Rolling Contact Fatigue Cracks", *Journal of Tribology*, vol. 110, no. 4, pp. 704–711, Oct. 1, 1988, ISSN: 0742-4787. DOI: 10.1115/1.3261717.

[94] G. Fajdiga and M. Sraml, "Fatigue crack initiation and propagation under cyclic contact loading", *Engineering Fracture Mechanics*, vol. 76, no. 9, pp. 1320–1335, Jun. 1, 2009, ISSN: 0013-7944. DOI: 10.1016/j.engfracmech.2009.02.005.

[95] D. I. Fletcher, P. Hyde, and A. Kapoor, "Modelling and full-scale trials to investigate fluid pressurisation of rolling contact fatigue cracks", *Wear*, Contact Mechanics and Wear of Rail/Wheel Systems - CM2006, vol. 265, no. 9, pp. 1317–1324, Oct. 30, 2008, ISSN: 0043-1648. DOI: 10.1016/j.wear.2008.02.025.

[96] P. E. Bold, M. W. Brown, and R. J. Allen, "A Review of Fatigue Crack Growth in Steels Under Mixed Mode I and II Loading", *Fatigue & Fracture of Engineering Materials & Structures*, vol. 15, no. 10, pp. 965–977, 1992, ISSN: 1460-2695. DOI: 10.1111/j.1460-2695.1992.tb00025.x.

[97] T. Narabayashi *et al.*, "Experimental study on leak flow model through fatigue crack in pipe", *Nuclear Engineering and Design*, vol. 128, no. 1, pp. 17–27, Jul. 1, 1991, ISSN: 0029-5493. DOI: 10.1016/0029-5493(91)90245-D.

[98] L. V. Clarke *et al.*, "Measurement of fluid flow rates through cracks", *International Journal of Pressure Vessels and Piping*, vol. 71, no. 1, pp. 71–75, Apr. 1, 1997, ISSN: 0308-0161. DOI: 10.1016/S0308-0161(96)00056-7.

[99] N. M. Bagshaw, S. B. M. Beck, and J. R. Yates, "Identification of fluid flow regimes in narrow cracks", *Proceedings of the Institution of Mechanical Engineers, Part C: Journal of Mechanical Engineering Science*, vol. 214, no. 8, pp. 1099–1106, Aug. 1, 2000, ISSN: 0954-4062. DOI: 10.1243/0954406001523542.

[100] T. C. Chivers, "The influence of surface roughness on fluid flow through cracks", *Fatigue & Fracture of Engineering Materials & Structures*, vol. 25, no. 11, pp. 1095–1102, 2002, ISSN: 1460-2695. DOI: 10.1046/j.1460-2695.2002.00595.x.

[101] C. Hong, Y. Asako, and J.-H. Lee, "Estimation of Leak Flow Rates Through Narrow Cracks", *Journal of Pressure Vessel Technology*, vol. 131, no. 5, Sep. 2, 2009, ISSN: 0094-9930. DOI: 10.1115/1.3147984.

[102] V. Molotnikov and A. Molotnikova, *Theory of Elasticity and Plasticity: A Textbook of Solid Body Mechanics / by Valentin Molotnikov, Antonina Molotnikova*. 2021, ISBN: 978-3-030-66622-4.

[103] ASME, *Boiler and Pressure Vessel Code, Section VIII: Division 2*. American Society of Mechanical Engineers, 1998.

[104] V. N. Constantinescu, "On the Influence of Inertia Forces in Turbulent and Laminar Self-Acting Films", *Journal of Lubrication Technology*, vol. 92, no. 3, pp. 473–480, Jul. 1, 1970, ISSN: 0022-2305. DOI: 10.1115/1.3451444.

[105] S. T. Tzeng and E. Saibel, "Surface Roughness Effect on Slider Bearing Lubrication", *A S L E Transactions*, vol. 10, no. 3, pp. 334–348, Jan. 1, 1967, ISSN: 0569-8197. DOI: 10.1080/05698196708972191.

[106] H. J. Petroski and J. D. Achenbach, "Computation of the weight function from a stress intensity factor", *Engineering Fracture Mechanics*, vol. 10, no. 2, pp. 257–266, Jan. 1, 1978, ISSN: 0013-7944. DOI: 10.1016/0013-7944(78)90009-7.

[107] M. Skorupa *et al.*, "Application of the strip-yield model from the NASGRO software to predict fatigue crack growth in aluminium alloys under constant and variable amplitude loading", *Engineering Fracture Mechanics*, vol. 74, no. 3, pp. 291–313, Feb. 1, 2007, ISSN: 0013-7944. DOI: 10.1016/j.engfracmech.2006.06.014.

[108] A. U. de Koning and G. Liefting, "Analysis of Crack Opening Behavior by Application of a Discretized Strip Yield Model", in *Mechanics of Fatigue Crack Closure*, ASTM International, pp. 437–458. DOI: 10.1520/STP27224S.

[109] J. H. Kim and S. B. Lee, "Fatigue crack opening stress based on the strip-yield model", *Theoretical and Applied Fracture Mechanics*, vol. 34, no. 1, pp. 73–84, Aug. 1, 2000, ISSN: 0167-8442. DOI: 10.1016/S0167-8442(00)00025-2.

[110] T. Fett, C. Mattheck, and D. Munz, "On the calculation of crack opening displacement from the stress intensity factor", *Engineering Fracture Mechanics*, vol. 27, no. 6, pp. 697–715, Jan. 1987, ISSN: 00137944. DOI: 10.1016/0013-7944(87)90159-7.

[111] M. V. Dusen, "Platinum-resistance thermometry at low temperatures", *Journal of the American Chemical Society*, vol. 47, no. 2, pp. 326–332, 1925.

[112] DKE, *DIN EN IEC 60751:2023-06, Industrial platinum resistance thermometers and platinum temperature sensors*, Jun. 2023. DOI: 10.31030/3405985.

[113] M. De Strycker *et al.*, "Measuring the thermal expansion coefficient of tubular steel specimens with digital image correlation techniques", *Optics and Lasers in Engineering*, vol. 48, no. 10, pp. 978–986, Oct. 1, 2010, ISSN: 0143-8166. DOI: 10.1016/j.optlaseng.2010.05.008.

[114] D. J. Olive, *Linear Regression*. Cham: Springer International Publishing, 2017, ISBN: 978-3-319-55250-7 978-3-319-55252-1. DOI: 10.1007/978-3-319-55252-1.

[115] F. Dekking, *A Modern Introduction to Probability and Statistics: Understanding Why and How* (Springer Texts in Statistics). Springer, 2005, ISBN: 978-1-85233-896-1.

[116] F. A. Smith and J. D. Wilson, "Electrical Circuits and Water Analogies", *The Physics Teacher*, vol. 12, no. 7, pp. 396–399, Oct. 1, 1974, ISSN: 0031-921X. DOI: 10.1119/1.2350471.

[117] M. F. Sayre, "Elastic After-Effect in Metals", *Journal of Rheology*, vol. 3, no. 2, pp. 206–211, Apr. 1, 1932, ISSN: 0097-0360. DOI: 10.1122/1.2116452.

[118] W. Chen, T. Kitamura, and M. Feng, "Creep and fatigue behavior of 316L stainless steel at room temperature: Experiments and a revisit of a unified viscoplasticity model", *International Journal of Fatigue*, vol. 112, pp. 70–77, Jul. 1, 2018, ISSN: 0142-1123. DOI: 10.1016/j.ijfatigue.2018.03.010.

Unpublished Sources

[119] J. Happel, "Druckabbauraten-induzierte Erhöhung der Risswachstumsgeschwindigkeit", Master's thesis, Karlsruhe Institute of Technology. Karlsruhe, 2018.

[120] B. Welschof, "Pulsationen und Rissausbreitung", presented at the KIT - Institute of Mobile Machines (Mobima) (Karlsruhe), Aug. 12, 2017.

Internet Sources

[121] Inc. Ansys. "Ansys Mechanical | Structural FEA Analysis Software", Ansys Mechanical | Structural FEA Analysis Software. (2023), [Online]. Available: https://www.ansys.com/products/structures/ansys-mechanical (visited on 07/05/2023).

[122] A. Devices. "AD7195 - Datasheet Rev. A". (2017), [Online]. Available: https://www.analog.com/en/products/ad7195.html (visited on 07/08/2023).

[123] Hottinger Brüel & Kjær. "Temperature Compensation of Strain Gauges", HBK World. (2023), [Online]. Available: https://www.hbkworld.com/en/knowledge/resource-center/articles/strain-measurement-basics/strain-gauge-fundamentals/article-temperature-compensation-of-strain-gauges (visited on 01/17/2024).

Own Publications

[124] L. Michiels and M. Geimer, "Influence of high pressure drop rates on fatigue crack growth", in *Proceedings of 13th International Fluid Power Conference, Aachen, 13th - 15th June 2022*, 2022, p. 328.

[125] L. Michiels and M. Geimer, “Influence of High Pressure Drop Rates on Fatigue Crack Growth”, *Chemical Engineering & Technology*, vol. 46, no. 1, pp. 45–52, 2022, ISSN: 0930-7516, 1521-4125. DOI: 10.1002/ceat.202200385.

[126] L. Michiels and M. Geimer, “Dynamic fluid simulation of hydraulic oil flow inside fatigue cracks during transient loads”, in *Proceedings of 7th Global Fluid Power Society PhD Symposium (GFPS 2022)*, Naples, 2022.

[127] L. Michiels and M. Geimer, “On the frequency dependency of fatigue damage caused by viscous fluid-structure interaction in hydraulic components”, in *Proceedings of 18th Scandinavian International Conference on Fluid Power (SICFP 2023)*, Tampere, 2023.

[128] L. Michiels and M. Geimer, “Non-destructive pressure impulse examination for fatigue crack detection in hydraulic components”, in *Proceedings of the ASME/BATH 2023 Symposium on Fluid Power and Motion Control*, Sarasota, FL, USA, 2023.

[129] S. Beiser, L. Michiels, and M. Geimer, “State Estimation for a portal advancing mechanism by measuring the pressure in hydraulic actuators”, in *Proceedings of 18th Scandinavian International Conference on Fluid Power (SICFP 2023)*, Tampere, 2023, ISBN: 978-952-03-2911-2.

[130] B. Kazenwadel *et al.*, “Data-driven algorithms for predicting energy-efficient operating points in agricultural soil tillage”, in *Land.Technik AgEng 2023*, 2023, p. 519, ISBN: 978-3-18-092427-4. DOI: 10.51202/9783181024270.

[131] L. Michiels *et al.*, “Real-time localization of mobile machines by fusing barometric altitude measurements with surface profiles”, in *2022 IEEE 25rd International Conference on Information Fusion (FUSION)*, Linköping, Jul. 2022.